DISS. ETH NO. 26166

Structure and function of synapses in the first stages of processing in mouse neocortex

A thesis submitted to attain the degree of

DOCTOR OF SCIENCES of ETH ZURICH

(Dr. sc. ETH Zurich)

presented by

GREGOR FRANZ PAUL SCHUHKNECHT

MSc. ETH in Biology

born on 27.02.1989

citizen of Germany

accepted on the recommendation of

Prof. Dr. Mehmet Fatih Yanik

Prof. Dr. Kevan A. C. Martin

Dr. Graham Knott

Prof. Dr. Csaba Földy

2019

Table of Contents

Summary

A grand challenge of systems neuroscience is to explain how the canonical microcircuit of neocortex enables such a wealth of diverse functions, including our remarkable cognitive abilities. The superficial layers of the neocortex are particularly interesting for the cortical computation because they receive the majority of the driving input from the thalamus and implement the first stages of its processing. Their anatomy and physiology are currently studied in great detail using a myriad of different methods – yet many of the secrets of their function remain unresolved.

This thesis is comprised of two parts. First, we set out to investigate the long-standing conundrum that the motor areas of the neocortex violate the canonical circuit motif because they seem to lack the granular layer 4 (L4), which is the main recipient layer for thalamic input in sensory areas. We identified synapses of thalamic origin in the middle layer of mouse primary motor cortex (M1) and primary somatosensory cortex (S1) by their immunoreactivity for the vesicular glutamate transporter 2 (VGluT2). Using electron microscopy (EM), we found that M1 possesses the canonical circuit motif of core thalamic input to the middle cortical layer: thalamic synapses formed a minority of synapses in the neuropil of M1 (12%) and S1 (17%). However, thalamic synapses in M1 were larger compared to S1 (median postsynaptic density area of 0.064 μm^2 and 0.042 μm^2, respectively). A further intriguing difference between the areas was that thalamic synapses avoided inhibitory neurons in M1, which indicates that inhibitory gain control is implemented via different mechanisms compared to sensory areas. In conclusion, our results suggest that the thalamocortical projection to L4 of M1 probably has a similar driving effect on single neurons in L4 as it has in sensory areas.

In the course of this project, the fact emerged that we do not understand how the ultrastructural features of even a single cortical synapse relate to its physiological transmission strength. Thus, it remains experimentally unvalidated that quantitative EM studies at synaptic resolution can provide insights about the physiology of the underlying circuit. To bridge this gap, we recorded pairs of synaptically connected layer 2/3 pyramidal neurons in mouse S1 *in vitro* and then recovered all synapses between the neurons using correlated light microscopy (LM) and EM. The synapses in this study (n = 10 pairs) had mean excitatory postsynaptic potential (EPSP) amplitudes between 0.15 and 2.3 mV, which correlated with the cumulative area of their postsynaptic densities (r = 0.73). This correlation held when differential dendritic attenuation was corrected for. We then developed and validated a novel form of quantal analysis and found that the number of release sites of a connection exceeded the number of anatomical synapses. Thus, single cortical synapses are capable of multivesicular release and release of single vesicles does not saturate all postsynaptic receptors. Most previous correlative studies relied on LM and likely overestimated the number of synapses, and so concluded that each synapse contains only a single release site, which has become a central dogma in the field.

In conclusion, relating structure and function of the same synapses allowed us to bridge the gap between the anatomical and electrophysiological characterization of synaptic transmission in cortex. The relationship we discovered between synapse size and EPSP amplitude provides experimental confirmation that EM studies can inform about the physiology of the underlying neuronal circuitry and our data could be a key step towards giving functional attributes to high-power EM reconstructions of neocortical circuits.

Zusammenfassung

Es ist eine der grossen Herausforderungen der Neurowissenschaften zu erklären wir der kanonische Schaltkreis in der Grosshirnrinde (Neokortex) dazu in der Lage ist, eine solch reichhaltige Vielfalt an verschiedenen Funktionen zu ermöglichen, wie beispielsweise unsere aussergewöhnlichen kognitiven Fähigkeiten. Die Schaltkreise in den oberen kortikalen Schichten sind besonders interessant für das Verständnis der Rechenprozesse in der Grosshirnrinde, denn sie erhalten den Grossteil der anregenden Nervenfasern aus dem Thalamus und beinhalten die ersten Stufen der Verarbeitung dieser Signale. Die Anatomie und Physiologie dieser oberen Schichten werden momentan mit einer Vielzahl an verschiedenen Methoden sehr intensiv untersucht – trotzdem bleiben viele der Geheimnisse über ihre Funktionsweise im Verborgenen.

Diese Arbeit besteht aus zwei Teilen. Im ersten Teil untersuchten wir das lange unbeantwortete Rätsel, ob die Motorareale der Grosshirnrinde nicht den kanonischen Schaltkreis beinhalten, da ihnen allem Anschein nach die granulare Schicht 4 fehlt, in der, in den sensorischen Arealen, der Hauptteil der Synapsen aus dem Thalamus ankommt. Wir identifizierten Synapsen aus dem Thalamus in den mittleren Schichten des primären Motorkortex (M1) und des primären sensorischen Kortex (S1) anhand ihrer Immunreaktivität für den vesikulären Glutamattransporter 2 (VGLuT2). Über Elektronenmikroskopie (EM) fanden wir heraus, dass M1 das kanonische Element eines «Core» Eingangssignals vom Thalamus besitzt: Synapsen aus dem Thalamus bildeten die Minderheit aller Synapsen im Neuropil von M1 (12%) und S1 (17%). Allerdings waren Synapsen aus dem Thalamus in M1 grösser als in S1 (Median der Fläche der postsynaptischen dichten Membranregion (PSD) von 0.064 μm^2 und 0.042 μm^2). Ein weiterer interessanter Unterschied zwischen den Gehirnarealen bestand darin, dass Synapsen aus dem Thalamus inhibitorische Neurone in M1 mieden, was dafürspricht, dass die Kontrolle der inhibitorischen Signalverstärkung über andere Mechanismen geregelt sein muss im Vergleich zu sensorischen Hirnregionen. Zusammenfassend deuten unsere Resultate darauf hin, dass die thalamokortikalen Bahnen in die Schicht 4 im M1 wahrscheinlich einen ähnlich anregenden Effekt auf einzelne Neurone besitzen wir in den sensorischen Arealen.

Im Verlauf dieses Projektes kristallisierte sich die Tatsache heraus, dass wir nicht einmal verstehen wie die strukturellen Eigenschaften von einer einzigen Synapse, wie wir sie im EM sehen können, mit der physiologischen Stärke ihrer Signalübertragung zusammenhängen. Es bleibt somit experimentell unbestätigt, dass quantitative Studien, in denen Synapsen im EM untersucht werden, überhaupt Einblicke in die Physiologie des zugrundeliegenden Schaltkreises gewähren können. Um diese Diskrepanz zu überrücken haben wir die synaptische Reizübertragung zwischen Paaren von verbundenen Pyramidenzellen in der Schicht 2/3 im S1 der Maus *in vitro* gemessen und fanden anschliessend alle Synapsen zwischen den Neuronen mithilfe von korrelierter Lichtmikroskopie (LM) mit EM wieder. Die synaptischen Verbindungen in dieser Studie (n = 10 Paare) hatten mittlere Amplituden der exzitatorischen postsynaptischen Potentiale (EPSPs) zwischen 0.15 und 2.3 mV, die mit der Gesamtfläche der PSD korreliert waren (r = 0.73). Diese Korrelation blieb bestehen als wir die unterschiedliche dendritische Attenuierung herausrechneten. Anschliessend entwickelten wir eine neue Technik zur Analyse der gequantelten Neurotransmitterfreisetzung und fanden heraus, dass die Anzahl der Vesikelfreisetzungsstellen zwischen synaptisch verbundenen Zellen die Anzahl der anatomischen Synapsen überstieg. Somit müssen einzelne

kortikale Synapsen dazu in der Lage sein mehrere synaptische Vesikel freizusetzen und die Freisetzung eines einzelnen Vesikels kann nicht dazu führen, dass alle postsynaptischen Rezeptoren saturieren. Die meisten vorangegangenen Studien verliessen sich auf LM und überschätzten aus diesem Grund wahrscheinlich die Anzahl der Synapsen, wodurch sie schlussfolgerten, dass jede Synapse nur eine einzige Vesikelfreisetzungsstelle besitzt, was zu einem zentralen Dogma in den Neurowissenschaften wurde.

Zusammenfassend erlaubte uns unsere Zuordnung von Struktur und Funktion an den gleichen Synapsen die Diskrepanz zwischen anatomischer und elektrophysiologischer Charakterisierung von Synapsen in der Grosshirnrinde zu überbrücken. Der Zusammenhang, den wir zwischen Synapsengrösse und EPSP Amplitude entdeckten, bietet die experimentelle Bestätigung, dass EM Studien über die Physiologie der zugrundeliegenden Schaltkreise Auskunft geben können. Unsere Daten könnten ein wichtiger Schritt dazu sein um hochauflösenden EM Rekonstruktionen von Schaltkreisen der Grosshirnrinde funktionelle Attribute zuordnen zu können.

Acknowledgements

It is with the greatest pleasure and gratitude that I would like to first thank my mentor Kevan Martin, who has guided me with incredible skill and patience through my first 5000 hours of being a neuroscientist. Words cannot express how thankful I am for your generosity and kindness, for the excellent scientific education, and for giving me every opportunity to grow – through meditation, Alexander technique, and voice training – and for making me worry less. Thank you for allowing me to fail, for providing a safety net whenever one was needed, and for being my biggest critic, and of course for the cake.

The institute you and Rodney have built and the people you have assembled here have allowed me to prosper and develop personally and intellectually in ways I could never have imagined. It is therefore that my second "thank you" goes to the INI and all of its inhabitants and in particular the breakfast meeting group. This is a unique place in time and I consider myself truly fortunate to be a part of it.

I am tremendously grateful to Ora Ohana, who gifted me the art of *in vitro* whole-cell recordings for an entire month in her laboratory in Hamburg and who provided her constant and unconditional support, in particular during the early and vulnerable phase, when Saray and I assembled the setup and started our experiments.

Likewise, I am tremendously grateful to Ken Stratford for enthusiastically sharing his vast expertise in the art of quantal analysis and especially for enduring my initial ignorance of the secrets of synaptic transmission so patiently and with such a refreshing sense of humor.

Both Ora and Ken have been fantastic teachers and mentors to me, without whom the successful completion of the second project would have been hardly possible.

I would like to thank my sister-in-crime Saray Soldado Magraner for her aqueous assistance and for introducing a much-need Spanish composure into my work attitude. Thanks for putting up with me – I could not have done it without you.

I would like to thank Graham Knott and Csaba Földy for co-supervising my thesis, for their kind support, for sharing their great expertise in anatomy and physiology, and for their critical comments and suggestions on how to make the project better. The committee meetings have always been great fun and tremendously motivating. A very special "thanks" goes to Fatih Yanik, for so kindly "adopting" me.

Particular gratitude goes to John Anderson for his anatomical expertise and the whiskey, to Rita Bopp and German Köstinger for their mastery of the electron microscope and to Simone Holler-Rickauer for her heroic contributions to histology. Not only have they invested much of their time to being critically involved in the data acquisition and analysis for both projects, they have also patiently and joyfully taught me many of the things I know about neuroanatomy and guided me through the ultrastructural world, in particular when I joined the group as a novice in such matters.

Introduction

The human brain is often referred to as the crowning achievement of evolution. While this seems a rather egotistical statement in the light of all the other amazing achievements of evolution, and while it remains difficult to explain what makes us human based on our brain's anatomy (Herculano-Houzel, 2009), it is hard to argue against the fact that our brains have been crucially involved in the invention of the wheel, the creation of art, our space expeditions, and our ability to study brains. One structure within the human brain has likely been of particular importance for these and related endeavors: the neocortex. The neocortex is an evolutionary relatively young brain area that is unique to mammals and emerged with their appearance 200 million years ago (Glenn Northcutt and Kaas, 1995; Kaas, 2006). It is involved in sensory perception, motor execution, and higher-order brain functions, such as planning, language, and cognition (Douglas and Martin, 2012). Despite this rich myriad of diverse functions, the same principal canonical circuit architecture seems to be conserved across all of its areas (Douglas and Martin, 1991). This raises the intriguing question of what the blueprint of this circuitry is and whether we could advance our own technological developments by understanding more about the principles of its operation.

This thesis is comprised of two chapters: In the first chapter, we investigated a long-standing conundrum in the systems neuroscience field, which concerns the hypothesis that the areas of the neocortex that are responsible for voluntary movement could implement a different basic circuitry compared to the better-studied sensory areas. We tackled this question by conducting a detailed anatomical comparison of the synapses made by the thalamus in the main input layer of the motor and sensory cortex.

In the course of this project the realization emerged that we do not understand how the anatomical features of even a single cortical synapse seen in the electron microscope (EM) relate to its physiological strength. This problem has a deep significance for neuroscience for several reasons: (1) comparative electron microscopic studies at synaptic resolution, such as connectomics approaches and the study performed by us (Bopp et al., 2017), are often based on the assumption that big synapses are strong synapses and small synapses are weak synapses, but the experimental validation for this assumption is lacking. (2) Knowing the electrophysiological strength of synapses reconstructed from EM could allow us to construct more realistic computational models of neuronal circuits. (3) By relating structure and function of single synapses, we have the chance to gain a deeper understanding of synaptic transmission.

We subsequently tackled this question by combining *in vitro* whole-cell patch-clamp recordings of synaptically connected layer 2/3 (L2/3) pyramidal neurons in mouse sensory cortex with correlated light and electron microscopy to recover all recorded synapses anatomically.

Chapter 1

1.1 Introduction

1.1.1 Mapping the motor cortex

1.1.1.1 The excitable cortex – early electrophysiology

One of the seminal experiments in the discovery of the functions of the neocortex was the classical experiment of Fritsch and Hitzig (Fritsch and Hitzig, 1870), who stimulated the cortex of dogs with platinum wires and observed twitches of the contralateral musculature. In performing this fundamentally simple experiment, they provided the first evidence that the cerebral cortex was electrically excitable. More importantly, stimulation of different sites across the anterior cortex evoked twitches of different muscles, which assembled into a topographic map of different body parts on the surface of the brain. Despite their initial reluctance of using analgesia or anesthesia, which seems incomprehensible by modern ethical standards, their work is considered by some as one of the most important events in the history of neuroscience (Taylor and Gross, 2003).

Inspired by the work of Fritsch and Hitzig, David Ferrier immediately elaborated on their experiments and mapped the cortex of a monkey more systematically, which allowed him to produce a more complete and refined somatotopic motor map (Ferrier, 1874; Zola-Morgan, 1995; Taylor and Gross, 2003; Gross, 2007).

It was not realized until later that the experiments by Fritsch and Hitzig and by Ferrier had in fact produced somewhat antagonistic results. Two opposing schools of thought eventually emerged and engaged in a century-long controversy concerning which motor variables are encoded by the motor cortex. While Fritsch and Hitzig's experiments suggested that the motor cortex controls single muscles, the experiments by Ferrier produced rather complex movements that were more elaborate than the single muscle twitches that Fritsch and Hitzig had seen (Gross, 2007; Tanaka, 2016). These differences were likely facilitated by the different stimulation strategies used: Fritsch and Hitzig applied direct, galvanic current stimulation that allowed only for short periods of activation because it created a net charge transfer, which was harmful for the tissue. The alternating, faradic current used by Ferrier produced no net charge transfer and thus allowed extended stimulation periods, which in turn could result in activation of a larger region of cortex (Taylor and Gross, 2003; Gross, 2007; Tanaka, 2016).

This controversy has ultimately revealed that the topographic representation of individual body parts across the motor cortex (the *motor homunculus*) seems not to be the only intrinsic organizational principle. Extended electrical stimulation of cortical sites in monkeys evokes very complex, etiologically relevant actions, such as reach-and-grasp movements, hand-to-mouth movements, or defensive actions. These kinematically complex movement patterns form an action map that exists in addition to the motor homunculus. Thus, the motor cortex is now thought to contain both a map of the body and a map of etiologically relevant actions (Graziano et al., 2002a, 2002b; Taylor and Gross, 2003; Gross, 2007; Graziano, 2015; Tanaka, 2016).

With their findings, Ferrier, and Fritsch and Hitzig followed in the footsteps of Paul Broca to show the localization of function in the brain. From autopsies of patients with deficits in language production, Broca had concluded that a specific area in the left frontal lobes is responsible for producing articulated sounds. When this area, which became known as *Broca's Area*, was damaged, the ability to produce language ceased [(Broca, 1861) but see (Zola-Morgan, 1995; Taylor and Gross, 2003; Gross, 2007)].

1.1.1.2   The agranular motor areas - early anatomy

A contemporary advocate of the principal of functional localization in the brain was the anatomist Korbinian Brodmann, who parcellated the neocortex according to anatomical criteria in the early 1900s (Brodmann, 1909; Shipp, 2005). Using cytoarchitecture – the histological differences of cell types and their packing density across the cortical thickness and differences in the layer thicknesses – he separated the human neocortex into 52 distinct anatomical areas, a map that is still in use today. Despite a myriad of cytoarchitectonic variations across cortex, the motor cortex stood out in Brodmann's map because it violated the classical six-layered architecture of the cerebral cortex. Brodmann observed that during fetal development in primates, the six layers were present in the motor cortex, but in adult animals, the granular middle layer was absent. From his observations he termed these areas "agranular" in reference to their lacking of the *granular layer 4* (L4). "Granularity" referred to the appearance of L4 as a dense and grainy band under the microscope, which originates from the often smaller and more densely packed cell bodies that reside in L4 compared to layer 2/3 (L2/3) and layer 5 (L5) (Brodmann, 1909; Shipp, 2005).

Not all sensory areas contain spiny stellate cells in their L4 [e.g. the primary auditory cortex in cats (Smith and Populin, 2001)]. In cat primary visual cortex (V1), L4 contains star pyramids in addition to spiny stellate cells (Martin and Whitteridge, 1984) and in rodent barrel cortex, pyramidal neurons can be found in addition to star pyramids and spiny stellates (Staiger et al., 2004; Shepherd, 2009). Additionally, a small portion of L4 cells are inhibitory interneurons (Meyer et al., 2010; Keller et al., 2018). Thus, the granular appearance of L4 in sensory areas is a manifestation of a generally higher density of cell bodies, which could be a mechanism to amplify the thalamic input: the high density of cell bodies means that L4 also emits a large fraction of action potentials compared to other layers across the cortical thickness (Meyer et al., 2010).

Terminology is a powerful tool in science because it can facilitate or constrain the thinking of generations of scientists, especially when it is introduced by influential figures (Thorne, 1995). The names "granular" and "agranular" were potent because they suggested immediately to the anatomists and physiologists that the motor areas and the sensory areas were profoundly and inherently different from one another.

And indeed, before Brodmann's work should shape the zeitgeist of the field, Santiago Ramón y Cajal – together with Camillo Golgi the founding father of brain histology – had already characterized the layering of the human neocortex using the Nissl technique. His conclusion was that the precentral motor areas were in fact not agranular, but that a thin and rudimentary granular layer was present. Within this lamina, Cajal identified cells (using the Golgi Method), which had some morphological resemblance with neurons in the granular layer of sensory areas. His verdict was that the precentral motor areas in the human brain contain a reduced granular layer, which is interstratified with larger pyramidal neurons from the surrounding layers [(Ramón y Cajal, 1899), but see (García-Cabezas and Barbas, 2014; Barbas and García-Cabezas, 2015)].

The similarities Cajal described between L4 of motor and sensory cortex were largely forgotten and only revived recently (García-Cabezas and Barbas, 2014; Barbas and García-Cabezas, 2015). They could not withstand the power of Brodmann's terminology of "granular" and "agranular" that highlighted the differences.

A further important hallmark of motor areas is their control of the effectors of voluntary movement: corticospinal (pyramidal) neurons in L5 send their axons via the pyramidal tract to the spinal cord, where they form synapses with excitatory interneurons. Some of these interneurons in turn innervate the lower motor neurons (alpha motor neurons), which form synapses with the muscles. In this manner, the local spinal cord circuitry integrates the descending motor commands to instruct the muscles. This disynaptic motif exists in all mammals, including higher primates and humans (Kuypers, 1981; Rathelot and Strick, 2009; Shepherd, 2009). A subset of these corticospinal neurons in primates are the characteristically giant pyramidal neurons in upper L5, termed *Betz cells* (Betz, 1874).

An important exception to this scheme has been discovered in higher primates and humans. In these species, a particular type of corticospinal pyramidal cell forms monosynaptic connections with the lower motor neurons directly, without the detour via interneurons of the spinal cord circuitry. Intriguingly, this direct connection was found for L5 neurons in motor cortex, which innervate the finger muscles. It is thus hypothesized that the precision grip of humans and higher primates critically depends on ability of the motor cortex to control the muscles directly (Rathelot and Strick, 2006, 2009).

1.1.1.3   How does motor cortex operate?

Brodmann's notion that motor areas are agranular has prevailed in the field until very recently and most theories that were developed to explain how motor areas operate, in particular the primary motor cortex (M1), have embraced the absence of L4 as the central pillar of their reasoning (Shipp, 2005; Weiler et al., 2008; Shepherd, 2009; Shipp et al., 2013). The paramount importance of whether or not a granular middle layer exists in the motor areas will become evident in the next paragraphs.

1.1.2   The canonical microcircuit of the neocortex

In light of the impressive catalogue of qualitatively diverse functions, which the neocortex is capable of, it is striking that across cortical areas, the same *canonical microcircuit* motif is preserved (Douglas et al., 1989; Douglas and Martin, 1991). Interestingly, this unifying framework of how signals flow through neocortex was not discovered from anatomical observations. Instead, the canonical circuit motif was developed as a model that could explain electrophysiological responses of neurons across the layers of cat V1 following stimulation of the afferent fibers from the visual thalamus (the lateral geniculate nucleus, LGN).

Key hallmarks of the canonical microcircuit are (1) weak thalamic input, (2) strong recurrent excitation between superficial layer cells – most excitation in superficial layer cells is not due to monosynaptic input from the thalamus, but is generated intrinsically in the cortex. Thus, cortical circuits possess a great capacity to amplify weak thalamic input. (3) Recurrent inhibition balancing the recurrent excitation.

1.1.3   Feedforward thalamocortical computation in sensory areas

The most intuitive model for how thalamic input could shape the firing properties of cortical neurons is the famous model of a *simple cell* suggested by Hubel and Wiesel for cat V1 (Hubel and Wiesel, 1962). Neurons in the LGN have concentric receptive fields that consist of a circular central region and a doughnut-shaped surrounding region. These regions are antagonistic in their response to light. The neuron discharges when a light stimulus is presented to the "on" region and when a light stimulus is retracted from the "off" region (Kuffler, 1953).

A groundbreaking discovery, which has shaped the field of neuroscience for decades to come, was that neurons in V1 possess a strikingly different organization of receptive fields. As LGN cells, the receptive fields of simple cells consist of discrete "on" and "off" regions; however, these regions are organized not in a center-surround manner, but rather as elongated receptive fields. Neurons in V1 can be driven to discharge with elongated bar-shaped stimuli presented to the eyes (Hubel and Wiesel, 1959, 1962). In their model of a simple cell, Hubel and Wiesel described how the lateral arrangement of center-surround LGN cells could result in the transformation of center-surround receptive fields in the thalamus to the elongated, orientation- and direction-selective receptive fields of simple cells in V1. In this model of the simple cell, the processing of cortical neurons depends crucially on the feedforward flow of information from the thalamus to the neocortex.

1.1.4   The central role of layer 4 in models of cortical circuits

In the late 1950s, Hubel and Wiesel were able to tackle the question of what the visual cortex was doing with the information that it receives from the retina via the thalamus because some critical details of the physiology and anatomy of the subcortical visual pathway in the cat had already been worked out (Hubel and Wiesel, 1998). This included anatomical knowledge of the visual pathway from the LGN to the cortex, which had been traced out using the degeneration technique introduced by Minkowski in Zurich (Minkowski, 1913; Poljak, 1927; Waller and Barris, 1937) and knowledge about the center-surround receptive fields in the retina, which Steven Kuffler (the mentor of Hubel and Wiesel) had pioneered (Kuffler, 1953), as well as David Hubel's finding in preceding studies that the receptive fields in the LGN were also center-surround, like fields of retinal ganglion cells (Hubel and Wiesel, 1998).

In the years and decades after Hubel and Wiesel's groundbreaking discoveries, the anatomical and physiological properties of the thalamic input to cat V1 were studied in great detail and it was appreciated that the feedforward driving input from the X (parvocellular) and Y (magnocellular) neurons of the LGN terminated predominantly in separate sublaminae of the granular L4 (LeVay and Gilbert, 1976; Ferster and LeVay, 1978; Ferster and Lindström, 1983; Freund et al., 1985; Humphrey et al., 1985).

In their 1962 paper, Hubel and Wiesel were very intrigued by the fact that in L4 they had only found cells with simple receptive fields and had never seen a *complex cell*. Cells with complex fields were found in all other layers, except L4. From this observation, they suggested that simple cells could be constructed directly from the thalamic input that relayed the center-surround receptive fields from the LGN. The receptive fields of the complex cells outside of L4 could then in turn be constructed from combining the receptive fields of simple cells in L4 and the other layers (Hubel and Wiesel, 1962).

Therefore, from the early explorations of the neocortex (Hubel and Wiesel, 1998), L4 had a central role amongst the cortical lamina in models of cortical processing. Thalamic afferents terminate in all six layers of the

cortex, but the major termination zone is L4, and the thalamic synapses in L4 drive cortical activity (Hubel and Wiesel, 1962; Douglas et al., 1989; Douglas and Martin, 1991). This view was developed in the cat visual cortex, but it holds true across species and has been validated in the primary visual cortex of the monkey (Hubel and Wiesel, 1968, 1969; Winfield and Powell, 1983) and rodent primary somatosensory cortex [see for example (Meyer et al., 2010, 2010; Viaene et al., 2011; Schoonover et al., 2014)], amongst others.

It is not surprising that in light of the paramount importance of the thalamic input in driving cortical activity in sensory areas, the apparent absence of L4 in the agranular areas has sparked theories about how information could flow through the motor areas without the driving thalamic input. In the next paragraphs, we shall visit some of these theories in more detail.

1.1.5   Theories about the function of motor cortex

1.1.5.1   Theories that incorporate the thalamocortical projection

Most theories about the function of M1 have been founded on its agranular appearance and have thus largely neglected the thalamocortical input. A noteworthy exception is the work by Kuramoto and colleagues (2009, 2013), who mapped out in detail the thalamocortical axons that terminate in M1. In fact, in their concluding schematic diagram, L4 is indicated. Kuramoto et al. found that the thalamocortical afferents terminate in M1 in a similar core-matrix type projection pattern that is known from sensory areas (Jones, 2012).

Axons from the ventrolateral nucleus of the thalamus (VL) innervate predominantly the middle layers and the layer 5/6 (L5/6) border, whereas axons from the ventroanterior nucleus (VA) and the ventromedial nucleus (VM) terminate predominantly in layer 1 (L1). VL itself receives motor input from the cerebellum, which was hypothesized to carry a motor command, or "go" signal. VA and VM, on the other hand, are innervated strongly by GABAergic (gamma-aminobutyric-acid) axons from the basal ganglia, which are thought to select amongst competing motor programs and were hypothesized to relay preparatory motor information to the thalamus. Thus, information remains segregated at the subcortical level and the cerebellar and basal ganglia signals were hypothesized to merge in M1 corticospinal neurons to mediate motor control (Kuramoto et al., 2009, 2013).

In their unifying scheme, the group suggested that the VA/VM afferents could relay the gain-increase or "ready" signal to the apical dendrites of L5 corticospinal neurons in L1 and prepare them for activation. The VL afferents could then transmit the motor-command or "go"-signal from the cerebellum to the corticospinal neurons through the local circuitry in L4 and the superficial layers (Kuramoto et al., 2009, 2013).

A similar framework, which honors the diverse thalamic innervation in M1, but focuses strongly on the importance of top-down feedback projections in the motor system has been brought forward by Shipp (2005). In this account, the fact that motor areas are agranular means that they do not engage in serial feedforward processing of sensory information in the way the sensory cortices do. Instead, motor areas incorporate a strong feedback flow of information: motor plans are selected in higher motor and sensory areas and relayed via corticocortical feedback projections to M1, where the appropriate muscles are prepared for movement. Alternatively, competing motor plans could be selected through the basal ganglia circuitry and be relayed to M1 via thalamocortical projections.

In this framework, the thalamus could ultimately provide the decisive activation that finally drives the selected motor output by activating corticospinal neurons (Shipp, 2005).

1.1.5.2   Predictive Coding Theories

The *Predictive Coding Hypothesis* for motor control, on the other hand, is a theory, which explicitly demands the absence of the driving thalamic input to L4 in M1 (Shipp et al., 2013).

Predictive coding schemes describe how the brain could extract the causes about events in the sensory world by predicting what the sensory input should be. Sensory percepts are represented simultaneously in different areas across the sensory hierarchy in increasingly abstract ways. In this framework, higher areas generate predictions about what the sensory input should be based on an intrinsic, high-level representations of the world. These expectations are relayed to lower areas via descending, or feedback projections. The lower areas compare these expectations to the actual sensory input that they receive through ascending, bottom-up projections. Thereby, they generate a prediction error signal, which they in turn relay back to higher-order areas through ascending projections to modify the expectations in the higher areas. In an iterative manner, each area in the sensory hierarchy minimizes the prediction error until finally the system converges onto a plausible interpretation for the sensory input that satisfies all levels of the hierarchy and can be explained with the high-level representations of the events in the sensory world (Mumford, 1992; Rao and Ballard, 1999; Lee and Mumford, 2003; Bastos et al., 2012; Shipp et al., 2013).

In the theory brought forward of predictive coding in M1, the descending signals in the motor system serve as commands from higher motor areas to initiate a motor action in M1. Because the transmitted motor plan is deterministic, it does not require to be revised by ascending prediction error signals. The feedback pathway is driving and the feedforward pathway, which would signal a sensory prediction error to M1 in the form of the proprioceptive dynamics during the selected motor action, is redundant. The lack of the feedforward pathway to M1 is thought to be manifested in the absence of a granular L4 and with it the absence of feedforward thalamic input to M1. Further evidence for this view is seen in the developmental recession of L4 in M1 that was observed by Brodmann and that is hypothesized to coincide with the developmental acquisition of motor skills. Instead of reaching M1, sensory input following movement is thought to be relayed to sensory areas, where it updates the sensory view of the proprioceptive and kinematic state of the body and could be used to refine motor plans through intracortical connections with the motor areas (Shipp et al., 2013).

It is important to consider that not all intentional motor actions are necessarily controlled by the motor areas. Different cortical areas, such as cat V1 and rodent barrel cortex, have access to subcortical motor centers via projections from L5 pyramidal neurons and can evoke movement when stimulated [see for example (Douglas and Martin, 2004; Büttner and Büttner-Ennever, 2006; Matyas et al., 2010)]. One example is the control of eye movements: projections from V1, the frontal eye field, and other visual cortical areas terminate in the superior colliculus, where they generate downstream saccades of the eyes (Büttner and Büttner-Ennever, 2006).

1.1.5.3   Top-down information flow in motor cortex

Yet another theory was founded on the information flow through M1, as experimentally recorded through *in vitro* functional circuit mapping studies (Weiler et al., 2008; Shepherd, 2009).

In the absence of L4, the driving input for M1 was thought to arrive not predominantly through the thalamus, but instead through corticocortical connections from the sensory areas and higher motor areas to the superficial layers of M1. The intra-areal circuit organization of M1 revealed some interesting peculiarities, which seemed to fit well into this framework. In sensory areas, information is relayed from L4 upwards to L2/3 and then flows bidirectionally between the upper and the lower layers. In M1, on the other hand, the strongest functional intra-areal connection by far is the descending projection from L2/3 to L5, while the ascending L5/6 to L2/3 projection is weak compared to sensory areas (Weiler et al., 2008). From these observations, it was hypothesized that driving input reaches the upper layers of M1, where it is processed within recurrent intralaminar circuits and from whence it is then relayed to the lower layers to ultimately activate the L5 corticospinal neurons to drive movement (Weiler et al., 2008; Shepherd, 2009).

However, this model did recognize that, despite of its apparent lack of L4, M1 receives abundant input from the thalamus and that this thalamic input could be merged with the corticocortical input from motor and sensory areas in L2/3 of M1 (Weiler et al., 2008; Shepherd, 2009). In the absence of L4, the VL afferents were suggested to terminate in layer 3 (L3) at a similar cortical depth in comparison to the driving thalamic input to L4 in the sensory areas and it was therefore hypothesized that this projection could be the homolog of the driving projecting in sensory areas (Shepherd, 2009).

1.1.6   The long-lost layer 4 is re-discovered

A major revision to this latter theory was made when the same group recognized that they had found a "genuine layer 4 in motor cortex". In their 2015 study, Yamawaki et al. showed that – despite their persistent inability to detect L4 in the microscope – they had now measured that neurons at the L2/3 to L5 border in M1 received input from the primary thalamus, projected mostly unidirectionally to the superficial layers, and did not engage in long-range projections with other cortical areas. Thus the, same input-output circuits were reported to exist in the middle layer of M1 that are considered the hallmarks of the sensory L4 (Yamawaki et al., 2015).

Yamawaki et al. were not the first ones after Cajal to recognize that also M1 possesses a granular middle layer. During the review process of their 2015 paper, the group were pointed to two publications (Krieg, 1946; Skoglund et al., 1997), which had previously reported the existence of a L4 in rat M1, but which were usually not cited by the motor cortex community (see *Author Response* section of the online version of Yamawaki et al. 2015).

In conjunction with the established and detailed knowledge on the termination zones of thalamic input in M1, the ground had been paved for the group to conclude that M1 possesses a functional homolog of the sensory L4 (Yamawaki et al., 2015). Of course, this opened a novel explanatory path, because it could now be acknowledged that the thalamic input to M1 might play a decisive role in driving M1, as it does in sensory areas.

This card was quickly played by a group working on primate M1, who – around the same time – had described a cytological L4 in M1 of the adult animal using molecular markers (García-Cabezas and Barbas, 2014). They took sides with Cajal against Brodmann's observations. Subsequently, they used theirs and Yamawaki et al.'s

(2015) findings to hypothesize (maybe somewhat prematurely) that all primary areas (sensory and motor) are equivalent and that the thalamic input to L4 of the motor areas likely serves the same function as the thalamic input to L4 of sensory areas (Barbas and García-Cabezas, 2015).

1.1.7   The question

As highlighted in the paragraphs above, the motor cortex field is currently in the process of a paradigm-shift, whose roots can be traced back to the early days of modern neuroscience. It seems that the field is currently undecided how to digest the new knowledge and how to interpret the role of L4 in the context of cortical processing in M1.

The suggestion by Barbas and García-Cabezas (2015) is certainly intriguing and it would allow the motor cortex to be placed into the unifying framework of the canonical microcircuit, but many details about the thalamic input and about L4 remain missing and therefore, the degree of similarity between M1 and primary sensory areas remains unclear.

We reasoned that the functional importance of L4 for the cortical processing within M1 in comparison to sensory areas should be determined by the anatomical substrate of the thalamocortical projection. However, the number of thalamocortical synapses in L4 of M1, and their size distribution were entirely unknown for any species.

It is a hallmark of L4 in sensory areas that only a small fraction of all excitatory synapses originates from the thalamus (Ahmed et al., 1994; Latawiec et al., 2000; da Costa and Martin, 2009) and that each L4 neuron receives only a few hundred thalamic synapses (da Costa and Martin, 2011). In cat V1 and rodent barrel cortex *in vitro*, thalamocortical synapses evoke larger excitatory postsynaptic potentials (EPSPs) and depress more strongly during repeated activation than corticocortical synapses (Stratford et al., 1996; Gil et al., 1999; Bruno and Sakmann, 2006; Lee and Sherman, 2008). Because the high spontaneous activity of thalamic relay cells depresses thalamocortical EPSPs *in vivo*, they are equally large as corticocortical EPSPs (Bruno and Sakmann, 2006; Banitt et al., 2007).

A central question of research has therefore been how the numerically small thalamic input can be capable of driving activity in cortical areas? Several mechanisms are now known to enable the driving nature of the thalamic input: (1) local cortical circuit properties, such as amplification through recurrent circuits, can boost the thalamic signal (Douglas et al., 1989, 1995; Douglas and Martin, 1991; Stratford et al., 1996; Lübke et al., 2000) and (2) synchronous activation of thalamic synapses likely plays a critical role in exciting single neurons in L4 (Hubel and Wiesel, 1962; Bruno and Sakmann, 2006; Banitt et al., 2007).

In the light that thalamic synapses are capable of driving activity in sensory areas despite their small numbers and similar sizes as cortical synapses, it is very intriguing to compare the anatomical substrate of the thalamocortical projection to L4 of M1 to the thalamocortical projection to L4 of S1.

The first experimental part of this thesis is dedicated to a quantitative comparison of the thalamic input to layer 4 of primary motor cortex and primary somatosensory cortex in the mouse using primarily the electron microscope (EM). This work has been published in the Journal of Neuroscience (Bopp et al., 2017) and is reproduced on the following pages.

Systems/Circuits

An Ultrastructural Study of the Thalamic Input to Layer 4 of Primary Motor and Primary Somatosensory Cortex in the Mouse

Rita Bopp, Simone Holler-Rickauer, ⓘ**Kevan A.C. Martin, and** ⓘ**Gregor F.P. Schuhknecht**
Institute of Neuroinformatics, University of Zürich and ETH Zürich, 8057 Zürich, Switzerland

The traditional classification of primary motor cortex (M1) as an agranular area has been challenged recently when a functional layer 4 (L4) was reported in M1. L4 is the principal target for thalamic input in sensory areas, which raises the question of how thalamocortical synapses formed in M1 in the mouse compare with those in neighboring sensory cortex (S1). We identified thalamic boutons by their immunoreactivity for the vesicular glutamate transporter 2 (VGluT2) and performed unbiased disector counts from electron micrographs. We discovered that the thalamus contributed proportionately only half as many synapses to the local circuitry of L4 in M1 compared with S1. Furthermore, thalamic boutons in M1 targeted spiny dendrites exclusively, whereas ~9% of synapses were formed with dendrites of smooth neurons in S1. VGluT2$^+$ boutons in M1 were smaller and formed fewer synapses per bouton on average (1.3 vs 2.1) than those in S1, but VGluT2$^+$ synapses in M1 were larger than in S1 (median postsynaptic density areas of 0.064 μm^2 vs 0.042 μm^2). In M1 and S1, thalamic synapses formed only a small fraction (12.1% and 17.2%, respectively) of all of the asymmetric synapses in L4. The functional role of the thalamic input to L4 in M1 has largely been neglected, but our data suggest that, as in S1, the thalamic input is amplified by the recurrent excitatory connections of the L4 circuits. The lack of direct thalamic input to inhibitory neurons in M1 may indicate temporal differences in the inhibitory gating in L4 of M1 versus S1.

Key words: barrel cortex; electron microscopy; layer 4; motor cortex; thalamocortical; VGluT2

> **Significance Statement**
>
> Classical interpretations of the function of primary motor cortex (M1) emphasize its lack of the granular layer 4 (L4) typical of sensory cortices. However, we show here that, like sensory cortex (S1), mouse M1 also has the canonical circuit motif of a core thalamic input to the middle cortical layer and that thalamocortical synapses form a small fraction (M1: 12%; S1: 17%) of all asymmetric synapses in L4 of both areas. Amplification of thalamic input by recurrent local circuits is thus likely to be a significant mechanism in both areas. Unlike M1, where thalamocortical boutons typically form a single synapse, thalamocortical boutons in S1 usually formed multiple synapses, which means they can be identified with high probability in the electron microscope without specific labeling.

Introduction

The eponymous feature of agranular cortical areas, which include the primary motor cortex (M1), is their lack of the cytologically distinct layer 4 (L4) that is so prominent in granular cortical areas

(Brodmann, 1909). In sensory areas, the granular L4 is a primary site of thalamic input and thus is considered to be the first stage of processing in the laminar hierarchy (Hubel and Wiesel, 1962). Not surprisingly, in the absence of a granular L4, theories about the cortical computation in M1 have proposed a quite different mode of interlaminar processing (Shipp, 2005; Shepherd, 2009; Shipp et al., 2013) that completely exclude the thalamocortical input.

From time to time, reports have emerged of a L4 in M1, a layer composed of a thin band of pyramidal cells (Krieg, 1946; Skoglund et al., 1997; García-Cabezas and Barbas, 2014); and, as in granular cortex, thalamic afferents do innervate the middle layers of M1 (Strick and Sterling, 1974; Shinoda and Kakei, 1989; Yamamoto et al., 1990; Nakano et al., 1992; Kuramoto et al., 2009). Recordings from slices of mouse M1 by Yamawaki et al.

(2015) revealed a layer of pyramidal neurons located at the L3/5A border that could be monosynaptically activated from the thalamus and that projected to the upper layers, as do the L4 spiny neurons of sensory cortices. Barbas and García-Cabezas (2015) then speculated that L4 of M1 performs the same basic functions as in sensory cortices. Although this hypothesis is intriguing, many details about the thalamocortical projection to the middle layers of M1 are lacking, and thus its degree of similarity to L4 of sensory cortex remains unclear.

One key aspect of the thalamic input to sensory cortices is the small number of synapses it actually provides, despite its critical role in driving the cortex. In our quantitative studies of primary visual cortex (V1) in cat and monkey we found that only 5–10% of the asymmetric synapses in L4 are thalamic in origin (Ahmed et al., 1994; Latawiec et al., 2000; da Costa and Martin, 2009), which means that thalamic afferents form only a few hundred synapses with each neuron. In cat and monkey between 90% and 95% of the thalamic synapses were formed with pyramidal or spiny stellate cells, the remainder with smooth (putative GABAergic inhibitory) neurons (Ahmed et al., 1994; Latawiec et al., 2000; da Costa and Martin, 2009). To drive cortex with so few synapses, it was supposed that they must be strong. Physiological studies in cat V1 *in vitro* showed that, indeed, the thalamic synapses did have a larger amplitude EPSP with a very low coefficient of variance, but also that they depressed strongly with repeated activation (Stratford et al., 1996). Similar dynamics were reported for thalamocortical synapses in rodent somatosensory cortex (Gil et al., 1999; Bruno and Sakmann, 2006). *In vivo*, the spontaneous activity of the thalamus will depress the amplitude of the EPSPs, thus making the number of thalamic synapses simultaneously active a critical factor in driving the postsynaptic cell (Bruno and Sakmann, 2006; Banitt et al., 2007).

Comparable numbers of thalamocortical synapses, their size distribution, and their targets are unknown in M1 for any species. The present study was designed to answer this question by making a quantitative assessment of the thalamocortical projection to the forepaw area of M1 and comparing it with the barrel region of primary somatosensory cortex (S1). We exploited the fact that one of the vesicular glutamate transporters (VGluT2) is a selective marker for thalamocortical boutons (Nahmani and Erisir, 2005; Coleman et al., 2010). Our examination of synapses formed by VGluT2-positive (VGluT2$^+$) boutons in M1 and S1 indicates that the motor cortex possesses a canonical laminar pattern of thalamic innervation and that, in both M1 and S1, the thalamocortical synapses form a small fraction of the excitatory input to a L4 neuron.

Materials and Methods

Animals. Three adult male B6/C57 mice (Harlan Laboratories) under the license of K.A.C.M. (approved by Cantonal Veterinary Office, Zurich) were used in this study. The animals were anesthetized with pentobarbital and perfused transcardially with saline, followed by a solution of paraformaldehyde (4%), picric acid (15%), and glutaraldehyde (0.3%). The measured brain shrinkage with this solution was 11%.

Immunohistochemistry. All analyses of M1 were performed in the forelimb representation region (Tennant et al., 2011) and all analyses of S1 were performed within barrels. Areas were identified by conventional criteria (Paxinos and Franklin, 2004). The brain was removed from the skull and sectioned coronally at 80 μm. Sections were incubated in an ascending sucrose ladder for cryoprotection and then rapidly frozen individually in liquid nitrogen, followed by treatment in 0.5% sodium borohydrate, 3% hydrogen peroxide, and 10% methanol. After blocking in 1% BSA and 5% NGS in PBS for 30 min at room temperature (RT), we incubated the sections in primary antibody (anti-VGluT, made in

guinea pig; Millipore catalog #AB2251, RRID:AB_1587626, 1:10.000) in 1% BSA and 1% NGS in PBS overnight at 4°C. After this, sections were washed and incubated with a biotinylated secondary antibody (Vector Laboratories catalog #BA-7000, RRID:AB_2336132, 1:200) at RT for 3 h. After washing, we kept the sections in Vectastain ABC Kit (Vector Laboratories catalog #PK-6100, RRID:AB_2336819) overnight at 4°C and visualized the biotin using a protocol containing nickel-diaminobenzidine tetrahydrochloride and hydrogen peroxide treatment. Those sections that were selected for electron microscopy (EM) were then treated with 1% osmium tetroxide for 20 min, dehydrated using an ascending series of ethanol and propylene oxide (including treatment in 1% uranyl-acetate in 70% ethanol), and flat-mounted in Durcupan resin (Sigma-Aldrich). We have measured the shrinkage through all stages of processing in both cat (da Costa and Martin, 2009) and mouse (unpublished observations) cortex. The aldehyde fixation–perfusion produced a consistent 11% shrinkage. After washing out the sucrose used for cryoprotection, immunostaining the floating 80-μm-thick sections, osmicating, and then embedding the sections for light microscopy and EM, we measured no additional shrinkage of the tissue beyond that of the initial fixation–perfusion shrinkage of 11%. We have not corrected for this 11% shrinkage in any of the quantitative measurements or calculations reported in the Results.

To identify all the layers of termination of the thalamic afferents in M1 and S1, we additionally performed a VGluT2 and neuronal nuclei (NeuN) double labeling in one mouse, visualized with fluorescing secondary antibodies. NeuN was particularly helpful in identifying the cortical laminae in fluorescent images. In this protocol, we added 1% Triton X-100 and 10% donkey serum to the blocking solution and 0.4% Triton X-100 and 2% donkey serum to the primary antibody solution (VGluT2 as above and anti-NeuN, made in mouse, Millipore catalog #MAB377, RRID:AB_2298772, 1:500) and incubated the sections for 48 h at 4°C. Treatment in the secondary antibody solution (1% BSA, 2% donkey serum, 1% NGS, 0.4% Triton X-100 with Alexa Fluor 488, donkey-antimouse (Thermo Fisher Scientific catalog #A-21202, RRID:AB_2535788) and Alexa Fluor 555, goat-anti-guinea pig (Thermo Fisher Scientific catalog #A-21435, RRID:AB_2535856), both 1:500) was done at 4°C for 12 h. Sections were mounted in Vectashield mounting medium containing DAPI (Vector Laboratories catalog #H-1000, RRID:AB_2336789) and imaged using a Leica SP8 confocal laser-scanning microscope (10× dry objective, numerical aperture 0.3); subsequent image processing was done in ImageJ and Photoshop.

EM. Sections that contained L4 in barrel and motor cortex were cut into 50 nm ultrathin sections and collected on Pioloform-coated single-slot copper grids and treated with lead-citrate (after embedding). Unbiased disector counts of VGluT2-labeled and -unlabeled asymmetric synapses was performed as described by da Costa et al. (2009). Briefly, we randomly chose one section within the superficial 3 μm of the tissue block where penetration of antibody was satisfactory and randomly placed a grid of equally spaced sampling locations onto this section. Photographs of the sampling sites were taken at 13,500× and we counted the synapses that disappeared within a 5 × 5 μm square from reference to lookup section (separated by one intervening section, giving a disector volume of 2.5 μm^3). Reference and lookup section were then reversed and we counted in the opposite direction.

All synapses were examined in serial sections and were classified as either asymmetric (Gray's type 1) or symmetric (Gray's type 2) (Gray, 1959; Colonnier, 1968). Postsynaptic structures were also examined in multiple sections and identified as dendritic spines, dendritic shafts, or somata according to their morphological features (Gray, 1959; Colonnier, 1968; Peters et al., 1991; Peters and Palay, 1996).

3D bouton reconstructions. As with the unbiased disector method, we chose random locations on a starting section for the reconstruction of boutons forming labeled and unlabeled asymmetric synapses (VGluT2$^-$). Serial electron micrographs (13,500×) were generated for all VGluT2$^+$ and VGluT2$^-$ boutons contained in the initial section and fully reconstructed and digitized using the TrakEM2 plugin of ImageJ. VGluT2$^-$ boutons appeared more frequently and, to sample similar numbers of VGluT2$^+$ and VGluT2$^-$ boutons, in some sets of serial micrographs, we reconstructed only the VGluT2$^+$ boutons. We chose the
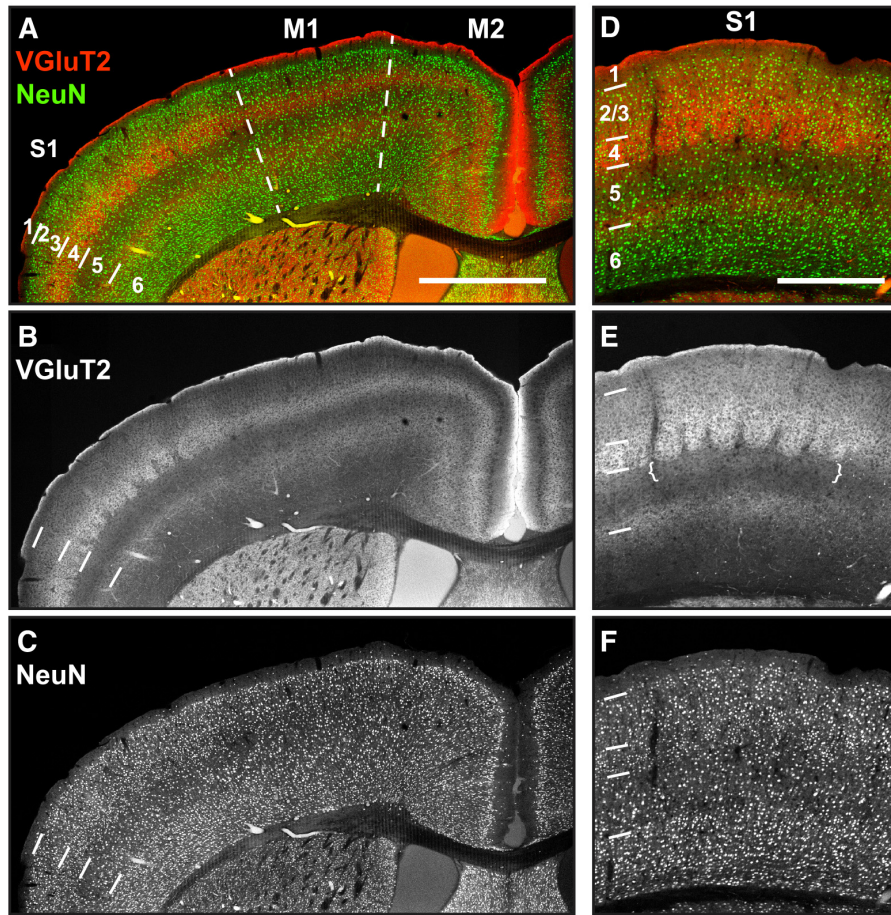
Figure 1. Thalamorecipient layers in sensory and motor areas revealed by dual labeling of VGluT2 and NeuN. ***A–C***, Coronal section (0.48 mm anterior of the bregma) containing M2, M1, and S1. Scale bar, 1 mm. ***A***, Merge of micrographs of VGluT2- and NeuN-stained sections with cortical layers 1– 6 indicated. ***B***, VGluT2 label occurs in three distinct bands. The L4 band is most salient in S1 and can be followed medially into M1 and M2, where it becomes fainter and thinner. ***C***, NeuN staining for neuronal somata revealing cytoarchitecture, L4 in S1 is composed of small and densely packed cells; in M1, it is present but less easily identified. ***D–F***, Coronal section containing vibrissal barrel cortex (0.48 mm posterior of bregma). Scale bar, 500 μm. ***D***, Merge of micrographs of VGluT2- and NeuN-stained sections with cortical layers 1– 6 indicated. ***E***, VGluT2 fluorescence is strongest in L4 barrels and less intense in the septa. VGluT2 label is also present in L1, L2/3, upper L5 (brackets), and at the L5/6 border. ***F***, NeuN staining revealing the cytoarchitecture of barrel cortex.

method of reconstructing either all or none of the VGluT2$^-$ boutons in a starting section to avoid size biases. Using a sampling grid to select a subset of VGluT2$^-$ boutons for reconstruction would have biased our selection toward larger VGluT2$^-$ boutons because objects with large cross-sectional areas have a higher probability of falling on a sampling spot. For both samples, only boutons that could be reconstructed entirely throughout the set of serial sections were included in the analysis. Bouton, spine head, and mitochondria volume and synapse area were then measured in the same software by multiplying the manually traced areas with the section thickness (50 nm). 3D reconstructions of representative structures were exported into the Blender software, fitted with a skin, and rendered to offer a 3D impression. Subsequent data analysis and visualization were performed with MATLAB R2015a (The MathWorks) and GraphPad Prism 6.

Estimation of synaptic vesicle density. We estimated the vesicle density of VGluT2$^-$ and VGluT2$^+$ boutons from single electron micrographs. Vesicles were counted only in sections in which the postsynaptic density (PSD) was also present and in which the lumen of the vesicles were clearly visible; that is, not obscured by reaction end-product. Vesicles were annotated in single sections only when they appeared as full profiles, meaning that at least half of the vesicle was contained in the section. Vesicles that appeared exceptionally small (with a radius of <4nm) were excluded

because they were assumed to be sliced in a way that only the cap of the vesicle was contained in the section. Because vesicles that are partially contained in the section (≥50%) were also annotated as full profiles, we corrected our raw counts with the Abercrombie factor (Linderstrøm-Lang et al., 1935; Abercrombie, 1946). Abercrombie's method is reliable for spherical particles of similar size and requires the section thickness to exceed the particle height by a factor of at least 1.5 (Clarke, 1992). We made a histogram of the distribution of the vesicle lumen radius in unlabeled boutons. The mean radius was 9 nm and, by adding 6 nm for each vesicle membrane, we estimated the mean vesicle height $\bar{H}$ (external diameter) to be 30 nm (Schikorski and Stevens, 1997). Because synaptic vesicles fulfill the criteria imposed by Abercrombie's method, we were able to use it in its original form, adopted from Clarke (1992), as follows:

$$\frac{N}{n} = \frac{T}{T + \bar{H}}$$

where N is the corrected number of vesicles, n the raw count, T the section thickness (50 nm), and $\bar{H}$ the mean height. The corrected vesicle count was divided by the respective bouton volume in which the vesicles were counted (the bouton area minus the area of the mitochondria contained in the bouton multiplied by the section thickness).
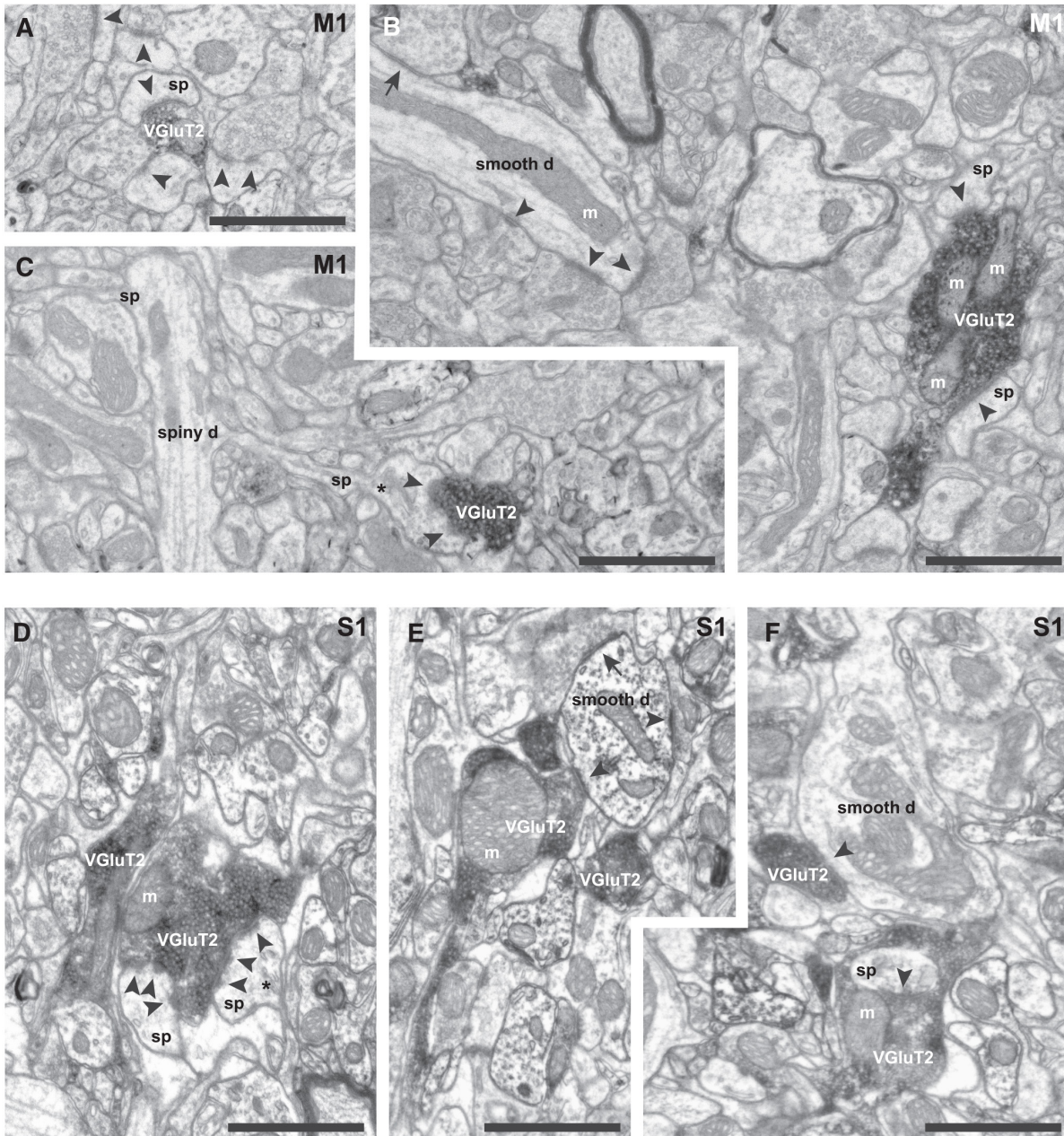
Figure 2. Electron micrographs of VGluT2-labeled boutons in L4 of motor cortex (**A**–**C**) and vibrissal barrel cortex (**D**–**F**). Scale bars in all panels, 1 μm. **A**, VGluT2^{+} bouton forming an asymmetric synapse (arrowhead) with a spine (sp) in L4 of M1. VGluT2 label appears as electron-dense material on synaptic vesicles. Unlabeled boutons in the surrounding neuropil also form asymmetric synapses with spines (arrowheads). **B**, Single VGluT2^{+} boutons often appeared large in cross-section, contained mitochondria (m), and formed synapses with multiple target spines (sp; arrowheads). A smooth (putative GABAergic) dendrite (smooth d) traverses and forms three asymmetric synapses (arrowheads) and one symmetric synapse (arrow) with unlabeled boutons. **C**, A VGluT2^{+} bouton forms a perforated synapse (two arrowheads) with a spine head containing a spine apparatus (asterisk). The spine originates from a dendrite traversing through (spiny d). **D**, A large VGluT2^{+} bouton in L4 of vibrissal barrel cortex forms two perforated synapses (arrowheads) on spines (sp), one of which contains a spine apparatus (asterisk). A second elongated VGluT2-labeled bouton (left) formed no synapses in this section. **E**, A VGluT2^{+} boutons forms a synapse (arrowhead) with a smooth dendrite (smooth d). The dendrite forms another asymmetric synapse with an unlabeled bouton (arrowhead) and a symmetric synapse (arrow) with an unlabeled (putative GABAergic) bouton, which contains pleomorphic vesicles. **F**, Some target spine heads are enveloped completely by the VGluT2^{+} bouton. In the same section, a VGluT2^{+} bouton forms an asymmetric synapse (arrowhead) with a smooth dendrite (smooth d).

Table 1. Summary of unbiased disector counts of synapses made by VGluT2 $^+$ boutons in M1 and S1 L4 for 3 mice

Mouse	M1			S1		
	No. of synapses	Synapses density per μm^3 $\pm$ SEM (N_V^{VGluT2} and N_V^{asym})	Percentage of VGluT2 synapses	No. of synapses	Synapse density per μm^3 $\pm$ SEM (N_V^{VGluT2} and N_V^{asym})	Percentage of VGluT2 synapses
1	VGluT2: 85 (218) all asym: 594 (154)	VGluT2: 0.156 $\pm$ 0.018 all asym: 1.543 $\pm$ 0.059	10.1%	VGluT2: 162 (316) all asym: 724 (228)	VGluT2: 0.205 $\pm$ 0.017 all asym: 1.270 $\pm$ 0.046	16.1%
2	VGluT2: 45 (82) all asym: 278 (72)	VGluT2: 0.220 $\pm$ 0.033 all asym: 1.544 $\pm$ 0.080	14.2%	VGluT2: 46 (80) all asym: 208 (72)	VGluT2: 0.230 $\pm$ 0.038 all asym: 1.156 $\pm$ 0.083	19.9%
3	VGluT2: 44 (88) all asym: 310 (74)	VGluT2: 0.200 $\pm$ 0.030 all asym: 1.676 $\pm$ 0.080	11.9%	VGluT2: 48 (80) all asym: 261 (68)	VGluT2: 0.240 $\pm$ 0.036 all asym: 1.535 $\pm$ 0.084	15.6%
			12.1%			17.2%

We counted VGluT2 $^+$ and unlabeled asymmetric synapses ("all asym" is the sum of labeled and unlabeled synapses) in a large number of disectors (indicated in parentheses). Then, we derived the density of VGluT2 $^+$ synapses (N_V^{VGluT2}) and all asymmetric synapses (VGluT2 $^+$ plus unlabeled, N_V^{asym}) by dividing the synapse count by the respective number of disectors analyzed, and by the disector volume (2.5 μm ^{3}). Synapse densities are given with SEM. Finally, we calculated the percentage of VGluT2 $^+$ synapses out of all asymmetric synapses by dividing N_V^{VGluT2} by N_V^{asym}.
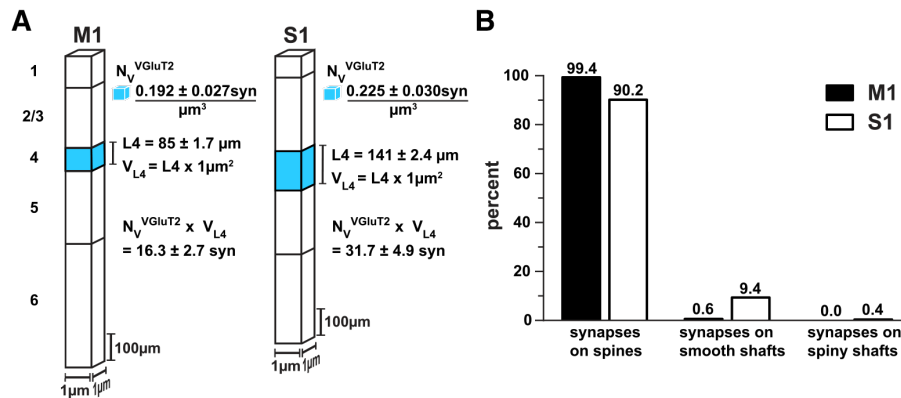
Figure 3. Summary of the unbiased disector counts. **A**, Thalamocortical pathway to M1 L4 provides approximately half as many synapses compared with S1. The density of thalamocortical synapses in the neuropil of a layer (N_V^{VGluT2} $\pm$ SEM) and the absolute thickness of the target layer (L4 $\pm$ SEM) determine how many synapses (syn) that thalamic projection contributes to the respective area. To compare the absolute number of VGluT2 synapses in M1 and S1 L4, we constructed hypothetical cuboid tissue blocks of M1 and S1 with a base area of 1 μm^2. By multiplying N_V^{VGluT2} by the volume of the respective L4 (V_{L4}), we derived an absolute number of VGluT2$^+$ synapses for M1 and S1 L4. In M1, the absolute number of VGluT2$^+$ synapses was only half that of S1 (the statistical range is determined by the accumulated SEM of N_V^{VGluT2} and L4 thickness). Scale bars indicate scales for cortical surface and individual layers. **B**, Postsynaptic targets of VGluT2$^+$ boutons in unbiased physical disector counts for M1 and S1. The respective percentage is indicated above each bar (spine synapses: n = 173 in M1 and 231 in S1, smooth shaft synapses: n = 1 in M1 and 24 in S1, spiny shaft synapses: n = 0 in M1 and 1 in S1).

Results

VGluT2 immunohistochemistry reveals the thalamorecipient middle layer in motor cortex

To obtain a qualitative comparison between the termination zones of thalamic afferents in M1 and S1, coronal sections containing these areas were immunostained with an antibody directed against VGluT2. In addition, an antibody directed against NeuN was used to identify the cortical lamination on the basis of its cytoarchitecture. The coronal slice shown in Figure 1, A–C, contained anterior S1, the forelimb representation of M1, and posterior secondary motor cortex (M2). In such slices, VGluT2 labeling revealed three distinct bands of high fluorescence in parallel to the pia and white matter, which could be traced through all three areas (Fig. 1A–C). The most dorsal band was located directly beneath the pia, in upper L1. The middle band was most prominent in S1: it was coextensive with the granular L4, as identified by the NeuN staining (Fig. 1C,F). From there, it extended medially into M1 and M2, where it narrowed, moved slightly more superficial, and had decreased fluorescence intensity. The third, most ventral band was located at the L5/6 border. In M1, it appeared diffuse and had a less sharp separation toward L5 compared with S1.

In S1, VGluT2-labeling revealed the location of barrels in L4 (Fig. 1D–F), which appeared as patches of high fluorescence sep-

arated by horizontal stripes of lower fluorescence, which are the interbarrel septa (Fig. 1E). There were also bands of fainter fluorescence in upper L5 directly below the barrels (Fig. 1E, brackets), in lower L2/3, and a thin band in L1 (Fig. 1E).

VGluT2$^+$ boutons in S1 and M1 reveal features attributed to thalamocortical boutons in sensory areas

VGluT2 is expressed primarily on synaptic vesicles (Hisano et al., 2000; Fremeau et al., 2001; Varoqui et al., 2002), so in the EM, the vesicle membranes appeared intensely stained by reaction product and only the paler lumen could be used to distinguish between individual vesicles (Fig. 2). The VGluT2$^+$ boutons were filled with synaptic vesicles. The synaptic cleft and PSD were unaffected by the staining and the mitochondria inside labeled boutons could be identified and traced easily. All VGluT2$^+$ boutons formed asymmetric (Gray's type 1) synapses (Fig. 2, arrowheads). In single electron micrographs, cross-sections of labeled boutons in M1 and S1 showed a similar morphology: they were often relatively large compared with unlabeled boutons in the surrounding neuropil, with diameters of up to 2 μm (Fig. 2B,D–F). In some cases, they formed synapses with two or three different targets in the same section (Fig. 2B,D) and often formed perforated synapses (Fig. 2C,D). The predominant targets were dendritic spines (Fig. 2, "sp"), which sometimes contained a
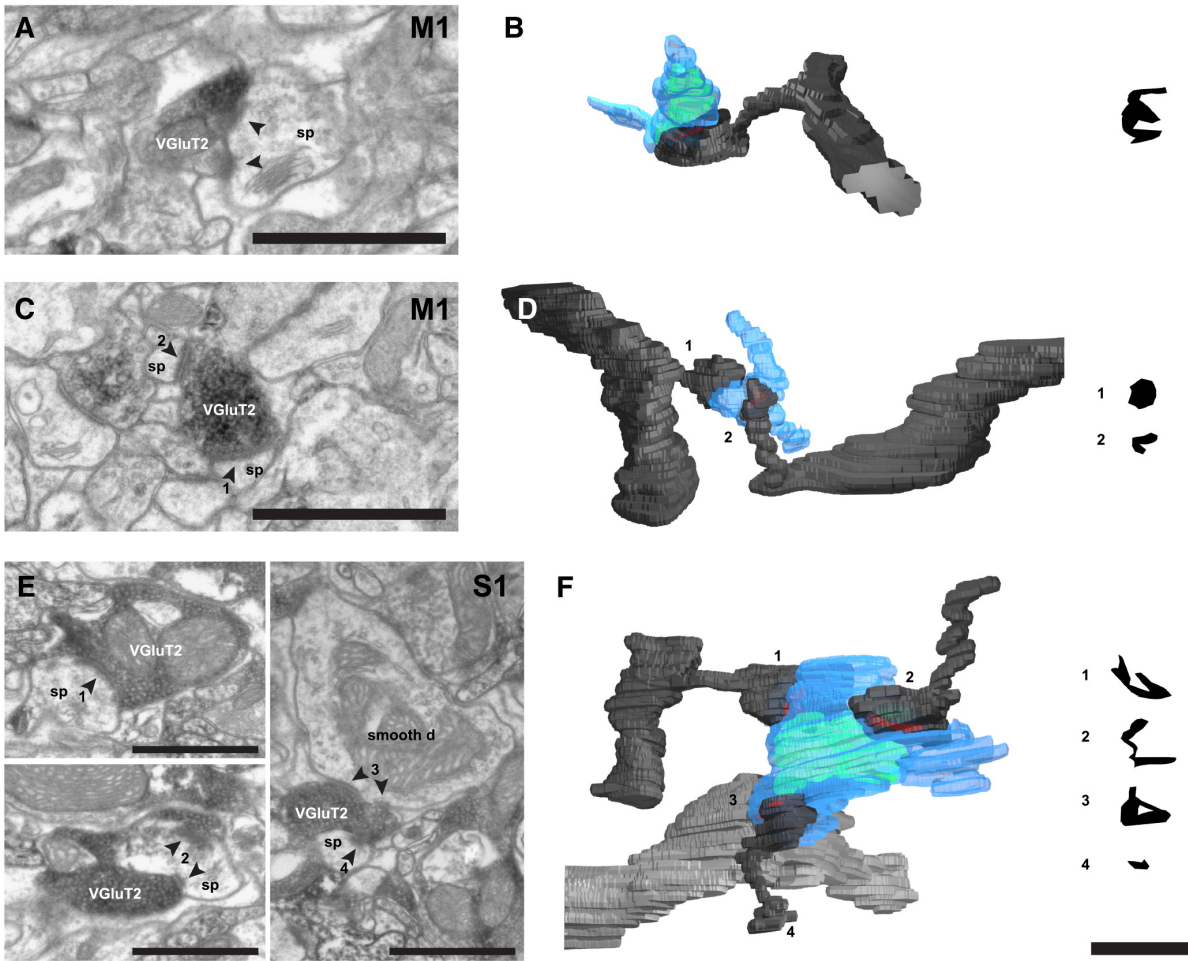
Figure 4. Representative 3D reconstructions of VGluT2$^+$ boutons and their postsynaptic densities and targets in L4 of M1 and S1. **A–D**, VGluT2$^+$ boutons in M1 L4. **E, F**, VGluT2$^+$ bouton in S1 L4. **A**, Electron micrograph of a VGluT2$^+$ bouton forming a single perforated synapse (arrowheads) on a dendritic spine (sp). **B** Left, Reconstruction of the VGluT2$^+$ bouton from **A** (blue), mitochondrion inside the bouton (green), PSD (red), and dendritic spine with a segment of its parent dendrite (black). Right, *en face* representation of the PSD. **C**, Electron micrograph of a VGluT2$^+$ bouton in L4 of M1, forming two synapses, which are numbered. **D** Left, Reconstruction of the VGluT2$^+$ bouton and its targets shown in **C**. Spines are indicated with numbers corresponding to the synapses that they receive, as seen in **C**. Right, *en face* representations of the two PSDs. **E**, Electron micrographs of a VGluT2$^+$ bouton in L4 of S1, forming four synapses (numbered). Synapse 3 was formed with the shaft of a smooth dendrite. **F** Left, Reconstruction of the VGluT2$^+$ bouton and its postsynaptic targets shown in **E** (smooth dendrite in gray). Right, *En face* representations of the four PSDs made by this bouton. Scale bars, 1 μm.
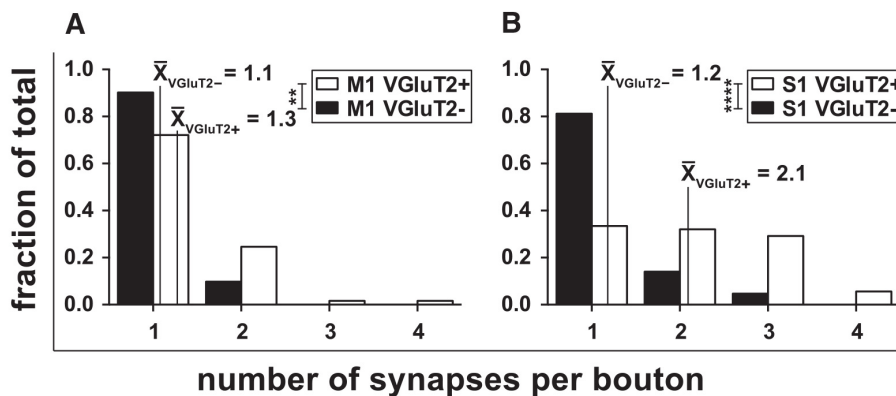
Figure 5. Comparison of the number of synapses made by VGluT2$^+$ boutons in M1 and S1 L4. **A**, VGluT2$^+$ boutons in M1 L4 ($n = 61$) predominantly form a single synapse, as did unlabeled boutons forming asymmetric synapses (VGluT2$^-$, $n = 82$). **B**, VGluT2$^+$ boutons in S1 L4 ($n = 72$) predominantly form multiple synapses (VGluT2$^-$, $n = 64$). $\bar{X}$ gives the arithmetic mean. The nonparametric M–W test was used for statistical analysis. **$p \leq 0.01$; ****$p \leq 0.0001$.

26
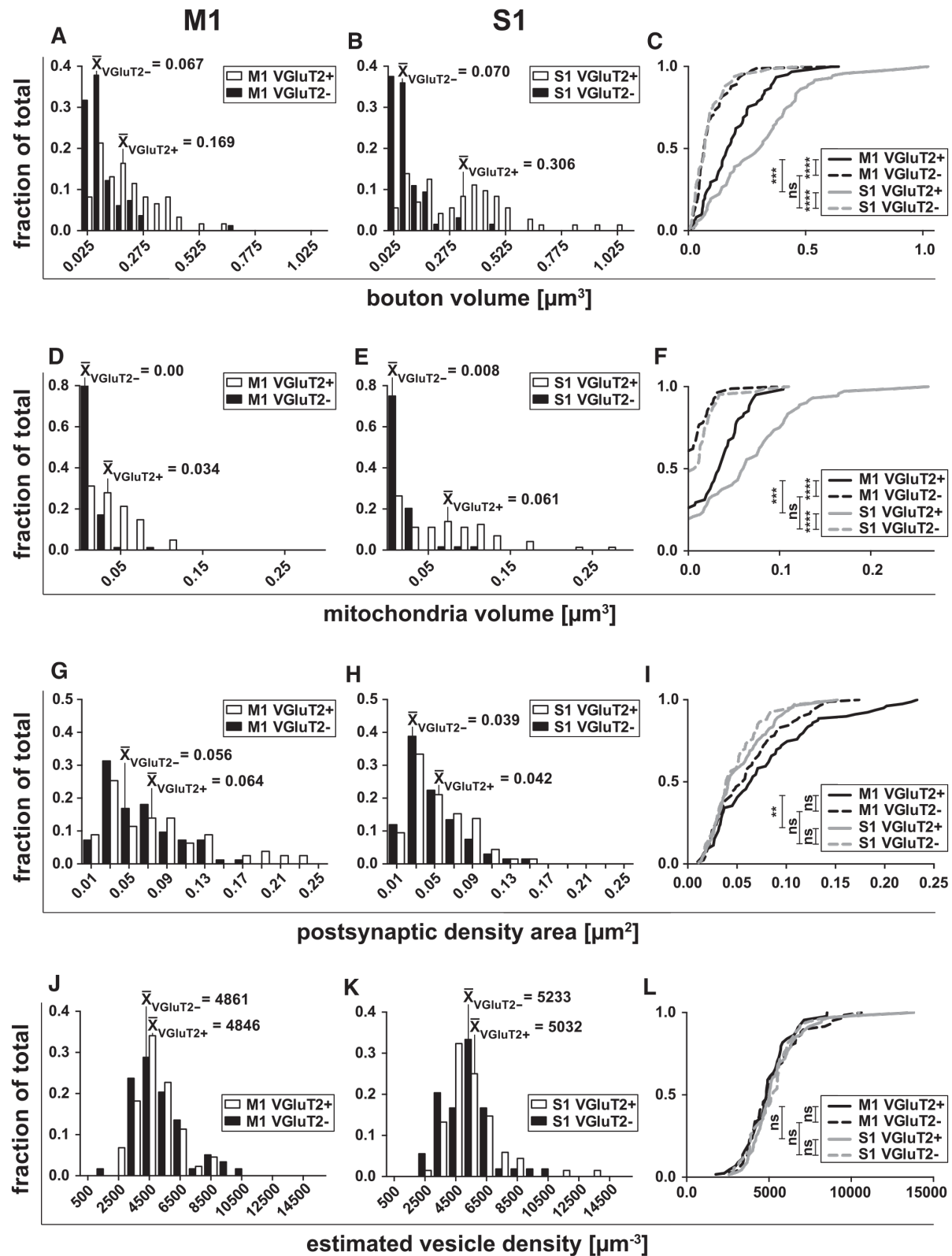
Figure 6. Morphological features of reconstructed VGluT2^{+} and VGluT2^{−} boutons in M1 and S1 L4. **A–C**, Distributions of the total volume of boutons in M1 (**A**; VGluT2^{+}, $n = 61$; VGluT2^{−}, $n = 82$) and in S1 (**B**; VGluT2^{+}, $n = 72$; VGluT2^{−}, $n = 64$); $\bar{X}$ is the median. **C**, Cumulative histogram of the data in **A** and **B**. **D–F**, Distributions of the (*Figure legend continues.*)

prominent spine apparatus (Fig. 2C,D, asterisks). In S1, we observed that VGluT2$^+$ boutons occasionally formed synapses with a smooth dendrite (Fig. 2E,F, "smooth d") and, more rarely, the soma of a cell. From this first qualitative assessment, it was evident that VGluT2$^+$ boutons in both areas exhibited features that are commonly attributed to thalamocortical boutons in L4 of sensory areas. These features include a large size, the formation of asymmetric synapses, many of which had perforated PSDs, and multisynaptic boutons (Winfield and Powell, 1983; Freund et al., 1985b; Keller et al., 1985; Freund et al., 1989; Peters et al., 1991).

Thalamocortical pathway to M1 L4 provides approximately half as many synapses per unit surface area as S1 L4

Nothing is known about the anatomical "weight" of the thalamocortical projection to L4 of motor cortex. VGluT2 fluorescence appeared less intense in L4 of M1 compared with S1 (Fig. 1), suggesting a lower number of thalamocortical boutons. We used EM to determine the proportion of synapses being made by VGluT2$^+$ boutons in L4 of M1 and compared it with L4 in S1. This analysis in M1 and S1 allowed us to validate the VGluT2 method against previous quantitative estimates of the thalamic afferents to S1 and to compare the numbers against a well studied sensory thalamocortical projection.

We counted the asymmetric synapses made by VGluT2-labeled boutons and the asymmetric synapses made by unlabeled boutons (VGluT2$^-$) using an unbiased physical disector method for rare events (da Costa et al., 2009). We randomly assigned sampling sites on ultrathin reference sections and took photographs of the sampling sites only when they contained a labeled profile. Synapses were counted when they disappeared from the reference to a lookup section, which were separated by one intervening section. From this, we calculated the mean density of all asymmetric synapses (labeled and unlabeled) in the neuropil within the volume of the disectors that were photographed (N_V^{asym}). The mean density of labeled synapses (N_V^{VGluT2}) was calculated from the number of labeled synapses over the volume of all sampling sites, both those photographed and those not photographed.

Our data are summarized in Table 1. Synapses made by VGluT2$^+$ boutons constituted 17.2% of the total number of asymmetric synapses in the neuropil of L4 in S1 and 12.1% of L4 in M1 (388 sites sampled in M1 and 476 sites sampled in S1 over 3 mice). This difference was due to the higher density of synapses formed by VGluT2$^+$ boutons (N_V^{VGluT2}) in L4 of S1 (0.225 μm^{-3}) than in M1 (0.192 μm^{-3}).

The absolute anatomical "weight" of the thalamocortical projection must include not just the density of VGluT2$^+$ synapses in L4, but also the volume of the thalamocortical termination zone. We thus estimated the absolute number of thalamocortical synapses in L4 of M1 and S1 that would be present in a hypothetical

←

(Figure legend continued.) mitochondria volume inside reconstructed boutons in M1 (**D**; VGluT2$^+$, $n = 61$; VGluT2$^-$, $n = 82$) and in S1 (**E**; VGluT2$^+$, $n = 72$; VGluT2$^-$, $n = 64$); $\overline{X}$ is the median. **F**, Cumulative histogram of the data in **D** and **E**. **G–I**, Distributions of the area of the PSDs in M1 (**G**; VGluT2$^+$, $n = 79$; VGluT2$^-$, $n = 83$) and in S1 (**H**; VGluT2$^+$, $n = 138$, VGluT2$^-$, $n = 67$); $\overline{X}$ is the median. Synapses on dendritic shafts were excluded for comparability. **I**, Cumulative histogram of the data in **G** and **H**. **J–L**, Vesicle density estimates for VGluT2$^+$ and VGluT2$^-$ boutons in M1 (**J**; VGluT2$^+$, $n = 44$; VGluT2$^-$, $n = 59$) and in S1 (**K**; VGluT2$^+$, $n = 68$; VGluT2$^-$, $n = 54$); $\overline{X}$ is the median. **L**, Cumulative histogram of the data in **J** and **K**. Statistical analysis was performed using the nonparametric M–W test, the results are shown in the box insets of the rightmost panels. ns: $p > 0.05$; *$p \leq 0.05$; **$p \leq 0.01$; ***$p \leq 0.001$; ****$p \leq 0.0001$.

cuboid block that spans the entire cortical thickness and has a base area of 1 μm^2. For this, we measured the thickness of L4 in M1 and S1 in the same osmicated sections that were used for the unbiased disector counts and then multiplied the density of synapses formed by VGluT2$^+$ boutons (N_V^{VGluT2}) by the volume of L4 in this hypothetical cuboid. For M1, this number was 16.3 $\pm$ 2.7 synapses and, for S1, it was 31.7 $\pm$ 4.9 synapses (Fig. 3A). The thalamocortical projection to L4 of M1 thus provides approximately half as many synapses as the equivalent projection to S1 per unit volume of the L4 thalamocortical termination zone.

Thalamocortical boutons rarely form synapses with smooth neurons in M1

In both areas, the principal targets of synapses formed by VGluT2$^+$ boutons were spines. In barrel cortex, 9.4% of the synapses were formed with smooth dendritic shafts that had the ultrastructural features of GABAergic neurons (Fig. 3B). We followed these dendrites over multiple sections to confirm that they did not form spines; therefore, all of the synapses found were formed with the dendritic shaft (Fig. 2B,E,F). Smooth dendrites often contained large mitochondria (Fig. 2B,E,F) and occasionally formed beads (see Fig. 8). These features are characteristic for smooth, putatively GABAergic neurons (Somogyi et al., 1983; Kisvárday et al., 1985; Keller and White, 1987; Peters et al., 1991; Ahmed et al., 1997). In contrast, in M1 we found only one VGluT2$^+$ synapse out of the 174 synapses sampled that was formed with a smooth dendritic shaft. All other VGluT2$^+$ boutons formed synapses with dendritic spines (Fig. 3B).

3D reconstructions of thalamocortical boutons in M1 and S1 L4

The thalamocortical afferents to sensory areas are known to drive cortical activity in sensory areas, but how they achieve this effect is still being actively discussed. To explore further the detailed anatomical features of the thalamocortical synapses in M1 and S1, we reconstructed a large sample of VGluT2$^+$ boutons in L4 of M1 ($n = 61$) and S1 ($n = 72$) and compared them with unlabeled boutons that formed asymmetric synapses (VGluT2$^-$) in M1 ($n = 82$) and S1 ($n = 64$). Within these full reconstructions, we measured the volume of each bouton, the total mitochondria volume inside the bouton, the number of synapses it made, the volume of the spine heads it formed synapses with, and the area of the PSD. We also estimated the vesicle density inside boutons from single sections. Figure 4 shows a representative set of reconstructed boutons selected for morphological features that were characteristic of their area.

The first striking difference we found between the two areas (Fig. 5) was that VGluT2$^+$ boutons in M1 only formed 1.3 synapses on average, whereas, in S1, VGluT2$^+$ boutons formed significantly more: 2.1 synapses per bouton on average [$p < 0.0001$, Mann–Whitney (M–W) test]. VGluT2$^-$ boutons in M1 made 1.1 synapses on average, similar to the 1.2 synapses made by VGluT2$^-$ boutons in S1 (not significant, $p = 0.10$, M–W test). In comparison, only 33% of VGluT2$^+$ boutons in S1 formed a single synapse (vs 81% of the VGluT2$^-$ boutons in S1) and ~30% of the VGluT2$^+$ boutons formed 2 and 3 synapses each, with some even making 4 synapses. In M1, by contrast, 72% of the VGluT2$^+$ boutons formed only 1 synapse and VGluT2$^+$ boutons rarely made >2 synapses (Fig. 5).

Individual VGluT2$^+$ boutons that made more than one synapse (multisynaptic) tended to be larger than boutons making only one synapse (unisynaptic) (Figs. 6A–C, 7C–F). VGluT2$^+$

28

Figure 7. Relationships of various morphological features of VGluT2$^+$ and VGluT2$^-$ boutons in M1 and S1 L4. **A, B,** Comparison of PSD sizes made by VGluT2$^+$ boutons that either formed single synapses (unisynaptic) or multiple synapses (multisynaptic) in M1 (**A**; unisynaptic, $n = 44$; multisynaptic, $n = 37$) and in S1 (**B**; unisynaptic, $n = 24$; multisynaptic, $n = 125$); $\overline{X}$ is the median (M–W test). **C, D,** Scatter plots showing the relationship between the bouton volume and all individual PSDs made by a bouton in M1 (**C**; VGluT2$^+$, $n = 81$; VGluT2$^-$, $n = 90$) and in S1 (**D**; VGluT2$^+$, $n = 149$; VGluT2$^-$, $n = 79$). In **C–H,** boutons are marked by different symbols indicating whether they were unisynaptic or multisynaptic (see box inset). **E, F,** Scatter plots showing the

boutons were significantly larger than VGluT2$^-$ boutons in both areas ($p < 0.0001$, M–W test). At the same time, the median VGluT2$^+$ bouton volume in S1 (0.31 μm^3) was larger than in M1 (0.17 μm^3) ($p < 0.001$, M–W test) due to the longer tail in the bouton volume distribution in S1 (Fig. 6A–C). In contrast, the volumes of VGluT2$^-$ boutons in both areas were not significantly different ($p = 0.55$, M–W test). The volume occupied by mitochondria inside VGluT2$^+$ boutons in S1 (median of 0.06 μm^3) was larger and had a longer tail in the distribution compared with M1 (median of 0.03 μm^3) (Fig. 6D–F). The volume of the mitochondria inside a bouton always followed a strong linear correlation with the bouton volume itself (Fig. 7G,H).

PSDs made by VGluT2$^+$ boutons in S1 (median 0.042 μm^2) were not significantly larger ($p = 0.40$, M–W test) than those made by the VGluT2$^-$ boutons (median 0.039 μm^2) (Fig. 6H). Intriguingly, we found that PSDs made by VGluT2$^+$ boutons in M1 (median 0.064 μm^2) were significantly larger than their counterparts in S1 ($p < 0.01$, M–W test), but not significantly larger ($p = 0.10$, M–W test) than the PSDs of M1 VGluT2$^-$ boutons (median 0.056 μm^2) (Fig. 6G–I). A similar picture emerged from the volumes of the targeted spine heads. The distribution had a longer tail in M1 compared with S1, but not significantly so ($p = 0.09$, M–W test). It has been reported previously that the volume of the spine head is correlated to the area of its PSD (Harris and Stevens, 1989; Schikorski and Stevens, 1999; Arellano et al., 2007), a relationship that was evident in our data (Fig. 7I,J). Importantly, PSDs made by multisynaptic boutons in M1 and S1 were not larger than those made by unisynaptic boutons (Fig. 7A–D) ($p^{M1} = 0.09$, $p^{S1} = 0.25$, M–W test). Only by summing up the areas of all PSDs that a bouton made was this "summed PSD" linearly correlated to the volume of the bouton (Fig. 7E,F).

←

relationship between the bouton volume and the sum of all PSDs made by a bouton in M1 (**E**; VGluT2$^+$, $n = 61$; VGluT2$^-$, $n = 82$), and in S1 (**F**; VGluT2$^+$, $n = 72$; VGluT2$^-$, $n = 64$). **G, H,** Scatter plots showing the relationship between bouton volume and volume of mitochondria they contain in M1 (**G**; VGluT2$^+$, $n = 61$; VGluT2$^-$, $n = 82$) and in S1 (**H**; VGluT2$^+$, $n = 72$; VGluT2$^-$, $n = 64$). **I, J,** Scatter plots of the relationship between spine head volume and the PSD area made on the spine head in M1 (**I**; VGluT2$^+$, $n = 79$; VGluT2$^-$, $n = 83$) and in S1 (**J**; VGluT2$^+$, $n = 138$; VGluT2$^-$, $n = 67$). Synapses formed with dendritic shafts were excluded for comparability. In **E–J,** r is the nonparametric Spearman correlation coefficient ($p \leq 0.0001$ for all, t test).
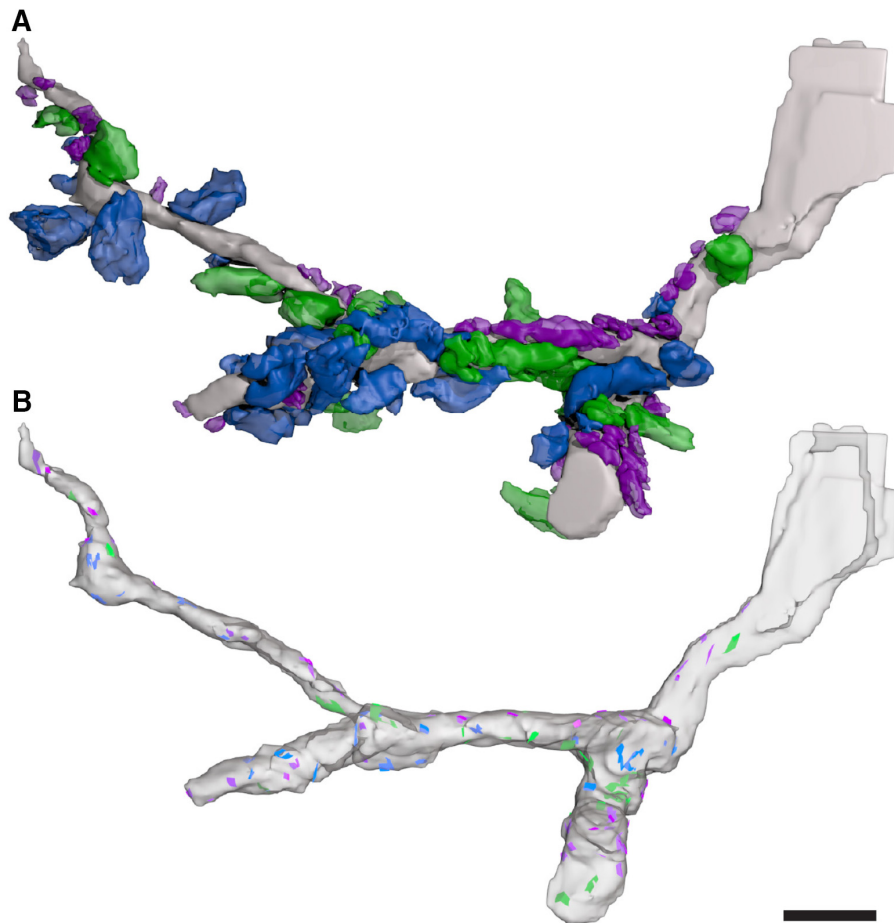
Figure 8. Proximal portion of a smooth, putatively GABAergic dendrite reconstructed from a tissue block in L4 of S1. The dendrite emerged directly from its parent soma (thickening to the right). We reconstructed a total length of 31 μm, including two branch points and a local varicosity (to the left). **A**, Dendrite fragment formed a total of 90 synapses: 19 with VGluT2$^+$ boutons (blue), 51 with VGluT2$^-$ boutons (purple), and 20 symmetric synapses with putative GABAergic boutons (green). **B**, To visualize individual postsynaptic densities, the dendrite was made transparent. Asymmetric synapses made by VGluT2$^+$ boutons are shown in blue, asymmetric synapses made by VGluT2$^-$ boutons in purple, and symmetric synapses in green. Scale bar, 2 μm.

Synaptic vesicle density estimation

For a number of reconstructed boutons, we estimated the packing density of presynaptic vesicles by counting the number of profiles in single sections and dividing by the respective bouton volume contained in the section that was not occupied by mitochondria. The estimated vesicle densities had a similar median and characteristically large variation. In both areas, there was no significant difference between VGluT2$^+$ and VGluT2$^-$ boutons ($p^{M1} = 0.73, p^{S1} = 0.93$, M–W test), similarly, the vesicle packing density of VGluT2$^+$ boutons was not significantly different between M1 and S1 ($p = 0.33$, M–W test) (Fig. 6J–L).

VGluT2$^+$ boutons in barrel cortex form synapses with smooth neurons

During the reconstructions of thalamic boutons in S1, we discovered two portions of smooth dendrites that were proximal to their soma and surrounded by VGluT2$^+$ boutons forming synapses with the shaft. Thalamocortical synapses constituted 30% of all the asymmetric synapses formed with these two segments of the smooth dendrites. A full reconstruction of the longer dendrite segment, including all its presynaptic partners, is shown in Figure 8. This segment emerged directly from the soma and included

two branch points and one local varicosity, which is a typical feature of smooth, putatively GABAergic dendrites. Over a total reconstructed length of 31 μm, this dendrite segment received a total of 90 synapses, of which 51 were asymmetric and made by VGluT2$^-$ boutons, 19 were asymmetric and made by VGluT2$^+$ boutons, and 20 were symmetric synapses made by unlabeled boutons (putatively GABAergic). The high proportion of VGluT2$^+$ boutons exceeded what would be expected from the distribution of postsynaptic partners of VGluT2$^+$ boutons that we found (Fig. 3B). Furthermore, we found two pairs of VGluT2$^+$ boutons that were made by the same axon and three pairs of boutons forming symmetric synapses that came from the same axon. Of the VGluT2$^-$ boutons, we did not find any two boutons coming from the same axon. Interestingly, almost all VGluT2$^+$ boutons were clustered either around the 2 branch points or at a local varicosity ~4 μm away from the branch point. Conversely, the unlabeled boutons forming symmetric synapses and the VGluT2$^-$ boutons were distributed more uniformly along the entire length of dendrite.

The VGluT2$^-$ boutons were visibly smaller than the VGluT2$^+$ boutons and the boutons forming symmetric synapses (Fig. 8). Many of the VGluT2$^+$ boutons that formed synapses

30
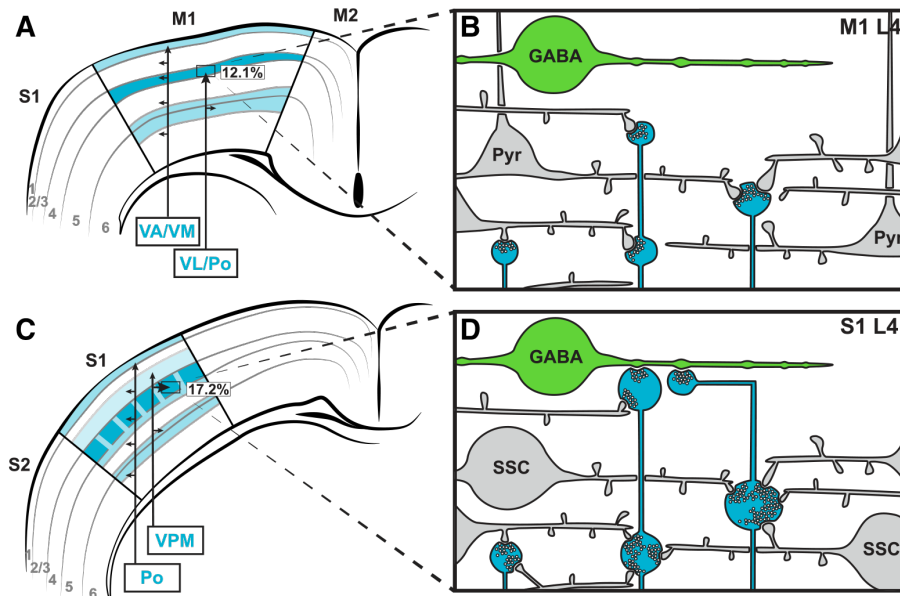
Figure 9. Schematic comparison of thalamic input to L4 of S1 and M1. **A**, In L4 of M1, ~12.1% of synapses originate from the thalamus, most of them presumably from VL and Po; other termination zones include L1 (from VA and VM) and the L5/6 border (from VL and Po). **B**, Thalamic boutons (blue) in M1 L4 usually form one synapse, innervate pyramidal cells (Pyr) (Yamawaki et al., 2014) due to the absence of spiny stellate cells, make on average larger PSDs than in S1, and almost completely avoid dendrites of smooth (putative GABAergic) cells. **C**, In S1, VPM projects into the L4 barrels, where it makes ~17.2% of all asymmetric synapses, and to the L5/6 border. Po projects to all laminae, in particular to L1 and into the septa and upper L5. **D**, Thalamic boutons in S1 L4 are larger compared with M1 and usually form >1 synapse. They innervate spiny stellate cells (SSCs) and the dendrites of inhibitory cells, yet their PSDs are smaller compared with M1.

with the shaft were multisynaptic and formed other synapses with spines in the neuropil (not illustrated). A similar picture emerged from the second, smaller dendrite segment (not shown), which formed a total of 11 synapses over a length of ~2.5 μm. VGluT2$^+$ boutons and VGluT2$^-$ boutons made five synapses each and one bouton formed a symmetric synapse. This fragment was most likely relatively close to its cell soma because of its large-diameter shaft.

Identifying thalamocortical boutons at EM in unlabeled sections of S1 L4

Taken together, thalamic boutons in L4 of S1 and M1 share many features with boutons made by corticocortical axons. In barrel cortex L4, however, our analyses revealed that, unlike other boutons in the neuropil of L4, individual thalamocortical boutons typically formed synapses with two or more targets (Figs. 4, 5). In S1, this feature alone can be used to distinguish boutons of thalamic origin from others forming asymmetric synapses in the surrounding neuropil in the EM without requiring specific labeling of thalamocortical axons. Therefore, if sufficient length of an unlabeled axon in L4 of S1 is reconstructed, then the presence of multisynaptic boutons in the sample will indicate with a high degree of certainty that the axon originates from the thalamus.

Discussion

We found that, under a unit area of cortex, L4 in mouse M1 receives half as many thalamocortical synapses as S1 does. Synaptic boutons in M1 are smaller than those in S1 and usually form only one synapse. Nonetheless, the median synapse size is bigger in M1 than in S1. Atypically, the thalamic projection to M1 L4 forms virtually all of its synapses with spiny neurons, whereas 9% of synapses are formed with smooth neurons in S1.

VGluT2 labeling reveals the termination laminae of thalamic afferents

VGluT1 mRNA is predominantly expressed in the neocortex, cerebellar cortex, and hippocampus, whereas VGluT2 is expressed in the thalamus, brainstem, hypothalamus, and deep cerebellar nuclei (Fremeau et al., 2001; Herzog et al., 2001; Sakata-Haga et al., 2001; Kaneko et al., 2002; Varoqui et al., 2002). Because VGluT2 mRNA is expressed at high levels by cells in all thalamocortical relay nuclei of the dorsal thalamus in rodents (Hisano et al., 2000), VGluT2-immunohistochemistry has become the state-of-the-art method for labeling the thalamocortical systems of all sensory modalities in rodents (Kubota et al., 2007; Kuramoto et al., 2009; Coleman et al., 2010; Li et al., 2013).

The laminar pattern of VGluT2 labeling in both M1 and S1 corresponds to the known termination zones of thalamic afferents (Fig. 9). The ventral posteromedial nucleus (VPM) is a "core" projection into L4 barrels, lower L2/3, and to the L5/6 border of S1, whereas the posteromedial nucleus (Po) projects in a "matrix-type" pattern sparsely to all laminae and densely to the barrel septa, upper L5, and L1 (Killackey, 1973; Donaldson et al., 1975; Wise and Jones, 1978; Koralek et al., 1988; Meyer et al., 2010; Viaene et al., 2011a). The projection from Po to L4 is very weak (Meyer et al., 2010) and boutons originating from Po are visibly smaller in the light microscope than boutons originating from VPM (Viaene et al., 2011a, 2011b).

In M1, the ventrolateral nucleus (VL) forms a core projection to L4 and the L5/6 border (and possibly also Po, see Yamawaki et al., 2014), while the ventroanterior (VA) and the ventromedial nuclei (VM) project in matrix-type patterns sparsely to all layers and densely to L1 (Strick and Sterling, 1974; Jones, 1975; Yamamoto et al., 1990; Kuramoto et al., 2009, 2015). VA and VM receive input from GABAergic afferents of the basal ganglia,

whereas VL is driven by strong glutamatergic input from cerebellar nuclei (Jones, 2012).

Thalamus contributes only a small fraction of the synapses in L4

For the quantifications of thalamic synapses, it was instructive to compare our approach of using VGluT2 as a marker for thalamic boutons against previous methods. Using degeneration techniques to identify thalamocortical boutons, White (1978) found that 20% of synapses in L4 of S1 originate from the thalamus. Anterograde transport of lectin yielded 18–21% (Keller et al., 1985). With VGluT2 staining, we found that, in both S1 and M1, thalamocortical synapses form a small fraction of the asymmetric (excitatory) synapses in L4 (17.2% and 12.1%, respectively).

The barrel L4 in S1 contained the strongest VGluT2 fluorescence and was continuous with L4 of M1. In M1, L4 had strong VGluT2 staining, but was considerably thinner compared with S1. The quantitative EM revealed that the total number of synapses that the thalamus contributes to the cortical circuitry in L4 of M1 was only half that of S1. Commonly, the number of axon varicosities seen at the light microscope level are thought to equal the number of synapses (Meyer et al., 2010; Oberlaender et al., 2012). With this assumption, one would underestimate the number of thalamocortical synapses in S1 L4 by a factor of 2. For M1, it is an approximation (1.3 synapses per VGluT2$^+$ bouton).

Thalamocortical synapses in S1 are similar in size to corticocortical synapses but smaller than thalamocortical synapses in M1

Although thalamocortical synapses form a minority of synapses in L4, they nonetheless are clearly effective in driving sensory cortices. The number of AMPA receptors in the postsynaptic membrane is proportional to the area of the PSD itself (Nusser et al., 1998; Tanaka et al., 2005). We found that PSDs of thalamocortical boutons in S1 are no larger than unlabeled asymmetric synapses in the surrounding neuropil and thus the amplitudes of thalamocortical and the corticocortical EPSPs are likely quite similar, as shown by *in vivo* experiments (Schoonover et al., 2014). Minimal stimulation of single thalamocortical fibers in slices of mouse S1 (Gil et al., 1999) and cat V1 (Stratford et al., 1996), however, evokes stronger responses in L4 neurons than do single corticocortical fibers. Thalamocortical synapses depress more strongly than corticocortical synapses (Stratford et al., 1996; Lee and Sherman, 2008), so it is to be expected that the high spontaneous activity of thalamic afferents causes relative depression (Banitt et al., 2007) that largely cancels out the amplitude difference between thalamocortical and corticocortical EPSPs *in vivo* (Castro-Alamancos et al., 1995; Chung et al., 2002; Boudreau and Ferster, 2005; Schoonover et al., 2014).

It has been suggested that the characteristically large thalamocortical "driver" boutons correlate with larger synapses and stronger EPSPs in S1 (Viaene et al., 2011b). Although VGluT2$^+$ boutons in S1 are large and usually multisynaptic, we found that the individual synapses were no bigger than those formed by VGluT2$^-$ boutons. PSDs of VGluT2$^+$ boutons in M1 were significantly larger than those in S1, indicating that they might elicit larger EPSPs. The disproportionately strong influence of thalamocortical input on cortical firing indicates that synchronous activation of thalamocortical synapses is critical (Hubel and Wiesel, 1962; Bruno and Sakmann, 2006; Banitt et al., 2007). Other circuit properties, such as amplification of thalamic input by the recurrent circuits within L4 (Douglas et al., 1989, 1995;

Stratford et al., 1996; Lübke et al., 2000), likely play a significant role in signal restoration.

Lack of feedforward inhibition in the thalamocortical projection to M1

VGluT2$^+$ boutons virtually never formed synapses with smooth dendrites in M1 L4. This is very different from S1 L4, where 9% of VGluT2$^+$ synapses innervated smooth dendrites, which is similar to the thalamocortical projections to cat and monkey V1 (Ahmed et al., 1994; Latawiec et al., 2000; da Costa et al., 2009). The proximal location of VGluT2$^+$ synapses on smooth neurons is reminiscent of the pattern in the cat, where some thalamocortical synapses are even formed directly on somata of GABAergic neurons (Freund et al., 1985a). This dense proximal input is likely a mechanism to ensure fast, reliable, and large-amplitude depolarization of interneurons after thalamic activation (Bagnall et al., 2011) and is probably why, in the sensory areas of all species studied, smooth (inhibitory) cells are more strongly and reliably driven by thalamic input than spiny (excitatory) neurons (Swadlow and Gusev, 2000; Porter et al., 2001; Swadlow, 2002; Gabernet et al., 2005; Cruikshank et al., 2007; Schiff and Reyes, 2012; Kloc and Maffei, 2014). Synchronous thalamocortical firing will thus drive monosynaptic activation of spiny cells in L4, followed by strong disynaptic feedforward inhibition (Ferster and Lindström, 1983; Douglas et al., 1989; Swadlow, 1989, 1990; Agmon and Connors, 1992; Gil and Amitai, 1996). Because one important role of feedforward inhibition in L4 of sensory areas is thought to be fast gain control (Douglas and Martin, 1991; Ohana et al., 2012), our observations raise the interesting question of why thalamic afferents in L4 of M1 do not follow this typical motif.

M1 processing

Various interpretations have emerged as to the flow of processing through M1. Weiler et al. (2008) proposed a "top-down" flow, with activity generated by inputs from S1 to L2/3 flowing down to L5 and then out of M1. Shipp et al. (2013) proposed an inference model in which a prediction error signal arrives via ascending inputs to L4 in sensory cortical areas and is corrected by a prediction signal arising from descending projections. Because M1 drives action, its prediction error is not revised, but instead is conveyed to the muscles, where the resulting action nulls the prediction error. They claim their theory demands an absence of L4 (Shipp et al., 2013). Both models thus assume the canonical thalamic input to L4 in M1 can be neglected.

An alternative model has been proposed by Kuramoto et al. (2009) whereby thalamic matrix-type (VA and VM) projections to L1 relay a gain increase or "ready" signal from the basal ganglia to the apical tuft of L5 pyramidal cells, whereas the thalamic core (VL) projection to L4 relays a motor command, or "go" signal from the cerebellum. This model fits our observations better and offers an explanation as to why the feedforward fast inhibitory gain control offered by direct thalamic input to smooth (GABAergic) cells appears to be missing in L4 of M1: the gain control is instead mediated via the matrix input to L1 inhibitory cells and pyramidal cell apical tufts.

Our study confirms that mouse M1 shares with S1 the canonical circuit motif of a core thalamic input to L4 and poses new questions about the role of the thalamic input to M1, which has been largely ignored in models of "agranular" cortical circuits.

References

Abercrombie M (1946) Estimation of nuclear population from microtome sections. Anat Rec 94:239–247. CrossRef Medline

Agmon A, Connors BW (1992) Correlation between intrinsic firing pat-

terns and thalamocortical synaptic responses of neurons in mouse barrel cortex. J Neurosci 12:319–329. Medline

Ahmed B, Anderson JC, Douglas RJ, Martin KA, Nelson JC (1994) Polyneuronal innervation of spiny stellate neurons in cat visual cortex. J Comp Neurol 341:39–49. CrossRef Medline

Ahmed B, Anderson JC, Martin KA, Nelson JC (1997) Map of the synapses onto layer 4 basket cells of the primary visual cortex of the cat. J Comp Neurol 380:230–242. Medline

Arellano JI, Benavides-Piccione R, Defelipe J, Yuste R (2007) Ultrastructure of dendritic spines: correlation between synaptic and spine morphologies. Front Neurosci 1:131–143. CrossRef Medline

Bagnall MW, Hull C, Bushong EA, Ellisman MH, Scanziani M (2011) Multiple clusters of release sites formed by individual thalamic afferents onto cortical interneurons ensure reliable transmission. Neuron 71:180–194. CrossRef Medline

Banitt Y, Martin KA, Segev I (2007) A biologically realistic model of contrast invariant orientation tuning by thalamocortical synaptic depression. J Neurosci 27:10230–10239. CrossRef Medline

Barbas H, García-Cabezas MÁ (2015) Motor cortex layer 4: less is more. Trends Neurosci 38:259–261. CrossRef Medline

Boudreau CE, Ferster D (2005) Short-term depression in thalamocortical synapses of cat primary visual cortex. J Neurosci 25:7179–7190. CrossRef Medline

Brodmann K (1909) Vergleichende Lokalisationslehre der Groβhirnrinde. Leipzig: JA Barth.

Bruno RM, Sakmann B (2006) Cortex is driven by weak but synchronously active thalamocortical synapses. Science 312:1622–1627. CrossRef Medline

Castro-Alamancos MA, Donoghue JP, Connors BW (1995) Different forms of synaptic plasticity in somatosensory and motor areas of the neocortex. J Neurosci 15:5324–5333. Medline

Chung S, Li X, Nelson SB (2002) Short-term depression at thalamocortical synapses contributes to rapid adaptation of cortical sensory responses in vivo. Neuron 34:437–446. CrossRef Medline

Clarke PG (1992) How inaccurate is the Abercrombie correction factor for cell counts? Trends Neurosci 15:211–212. CrossRef Medline

Coleman JE, Nahmani M, Gavornik JP, Haslinger R, Heynen AJ, Erisir A, Bear MF (2010) Rapid structural remodeling of thalamocortical synapses parallels experience-dependent functional plasticity in mouse primary visual cortex. J Neurosci 30:9670–9682. CrossRef Medline

Colonnier M (1968) Synaptic patterns on different cell types in the different laminae of the cat visual cortex: an electron microscope study. Brain Res 9:268–287. CrossRef Medline

Cruikshank SJ, Lewis TJ, Connors BW (2007) Synaptic basis for intense thalamocortical activation of feedforward inhibitory cells in neocortex. Nat Neurosci 10:462–468. Medline

da Costa NM, Martin KA (2009) The proportion of synapses formed by the axons of the lateral geniculate nucleus in layer 4 of area 17 of the cat. J Comp Neurol 516:264–276. CrossRef Medline

da Costa NM, Hepp K, Martin KA (2009) A systematic random sampling scheme optimized to detect the proportion of rare synapses in the neuropil. J Neurosci Methods 180:77–81. CrossRef Medline

Donaldson L, Hand PJ, Morrison AR (1975) Cortical-thalamic relationships in the rat. Exp Neurol 47:448–458. CrossRef Medline

Douglas RJ, Martin KA (1991) A functional microcircuit for cat visual cortex. J Physiol 440:735–769. CrossRef Medline

Douglas RJ, Martin KA, Whitteridge D (1989) A canonical microcircuit for neocortex. Neural Comput 1:480–488. CrossRef

Douglas RJ, Koch C, Mahowald M, Martin KA, Suarez HH (1995) Recurrent excitation in neocortical circuits. Science 269:981–985. CrossRef Medline

Ferster D, Lindström S (1983) An intracellular analysis of geniculo-cortical connectivity in area 17 of the cat. J Physiol 342:181–215. CrossRef Medline

Fremeau RT Jr, Troyer MD, Pahner I, Nygaard GO, Tran CH, Reimer RJ, Bellocchio EE, Fortin D, Storm-Mathisen J, Edwards RH (2001) The expression of vesicular glutamate transporters defines two classes of excitatory synapse. Neuron 31:247–260. CrossRef Medline

Freund TF, Martin KA, Somogyi P, Whitteridge D (1985a) Innervation of cat visual areas 17 and 18 by physiologically identified X- and Y- type thalamic afferents. II. Identification of postsynaptic targets by GABA immunocytochemistry and Golgi impregnation. J Comp Neurol 242:275–291. CrossRef Medline

Freund TF, Martin KA, Whitteridge D (1985b) Innervation of cat visual areas 17 and 18 by physiologically identified X-and Y-type thalamic afferents. I. Arborization patterns and quantitative distribution of postsynaptic elements. J Comp Neurol 242:263–274. CrossRef Medline

Freund TF, Martin KA, Soltesz I, Somogyi P, Whitteridge D (1989) Arborisation pattern and postsynaptic targets of physiologically identified thalamocortical afferents in striate cortex of the macaque monkey. J Comp Neurol 289:315–336. CrossRef Medline

Gabernet L, Jadhav SP, Feldman DE, Carandini M, Scanziani M (2005) Somatosensory integration controlled by dynamic thalamocortical feedforward inhibition. Neuron 48:315–327. CrossRef Medline

García-Cabezas MÁ, Barbas H (2014) Area 4 has layer IV in adult primates. Eur J Neurosci 39:1824–1834. CrossRef Medline

Gil Z, Amitai Y (1996) Properties of convergent thalamocortical and intracortical synaptic potentials in single neurons of neocortex. J Neurosci 16:6567–6578. Medline

Gil Z, Connors BW, Amitai Y (1999) Efficacy of thalamocortical and intracortical synaptic connections: quanta, innervation, and reliability. Neuron 23:385–397. CrossRef Medline

Gray EG (1959) Axo-somatic and axo-dendritic synapses of the cerebral cortex. J Anat 93:420–433. Medline

Harris KM, Stevens JK (1989) Dendritic spines of CA 1 pyramidal cells in the rat hippocampus: serial electron microscopy with reference to their biophysical characteristics. J Neurosci 9:2982–2997. Medline

Herzog E, Bellenchi GC, Gras C, Bernard V, Ravassard P, Bedet C, Gasnier B, Giros B, El Mestikawy S (2001) The existence of a second vesicular glutamate transporter specifies subpopulations of glutamatergic neurons. J Neurosci 21:RC181. Medline

Hisano S, Hoshi K, Ikeda Y, Maruyama D, Kanemoto M, Ichijo H, Kojima I, Takeda J, Nogami H (2000) Regional expression of a gene encoding a neuron-specific Na+-dependent inorganic phosphate cotransporter (DNPI) in the rat forebrain. Mol Brain Res 83:34–43. CrossRef Medline

Hubel DH, Wiesel TN (1962) Receptive fields, binocular interaction and functional architecture in the cat's visual cortex. J Physiol 160:106–154. CrossRef Medline

Jones EG (1975) Lamination and differential distribution of thalamic afferents within the sensory-motor cortex of the squirrel monkey. J Comp Neurol 160:167–203. CrossRef Medline

Jones EG (2012) The thalamus. New York: Springer Science and Business Media.

Kaneko T, Fujiyama F, Hioki H (2002) Immunohistochemical localization of candidates for vesicular glutamate transporters in the rat brain. J Comp Neurol 444:39–62. CrossRef Medline

Keller A, White EL (1987) Synaptic organization of GABAergic neurons in the mouse SmI cortex. J Comp Neurol 262:1–12. CrossRef Medline

Keller A, White EL, Cipolloni PB (1985) The identification of thalamocortical axon terminals in barrels of mouse SmI cortex using immunohistochemistry of anterogradely transported lectin (Phaseolus vulgarisleucoagglutinin). Brain Res 343:159–165. CrossRef Medline

Killackey HP (1973) Anatomical evidence for cortical subdivisions based on vertically discrete thalamic projections from the ventral posterior nucleus to cortical barrels in the rat. Brain Res 51:326–331. CrossRef Medline

Kisvárday ZF, Martin KA, Whitteridge D, Somogyi P (1985) Synaptic connections of intracellularly filled clutch cells: a type of small basket cell in the visual cortex of the cat. J Comp Neurol 241:111–137. CrossRef Medline

Kloc M, Maffei A (2014) Target-specific properties of thalamocortical synapses onto layer 4 of mouse primary visual cortex. J Neurosci 34:15455–15465. CrossRef Medline

Koralek KA, Jensen KF, Killackey HP (1988) Evidence for two complementary patterns of thalamic input to the rat somatosensory cortex. Brain Res 463:346–351. CrossRef Medline

Krieg WJ (1946) Connections of the cerebral cortex. I. The albino rat. B. Structure of the cortical areas. J Comp Neurol 84:277–323. CrossRef Medline

Kubota Y, Hatada S, Kondo S, Karube F, Kawaguchi Y (2007) Neocortical inhibitory terminals innervate dendritic spines targeted by thalamocortical afferents. J Neurosci 27:1139–1150. CrossRef Medline

Kuramoto E, Furuta T, Nakamura KC, Unzai T, Hioki H, Kaneko T (2009) Two types of thalamocortical projections from the motor thalamic nuclei of the rat: a single neuron-tracing study using viral vectors. Cereb Cortex 19:2065–2077. CrossRef Medline

Kuramoto E, Ohno S, Furuta T, Unzai T, Tanaka YR, Hioki H, Kaneko T (2015) Ventral medial nucleus neurons send thalamocortical afferents

more widely and more preferentially to layer 1 than neurons of the ventral anterior–ventral lateral nuclear complex in the rat. Cereb Cortex 25:221–235. CrossRef Medline

Latawiec D, Martin KA, Meskenaite V (2000) Termination of the geniculo-cortical projection in the striate cortex of macaque monkey: a quantitative immunoelectron microscopic study. J Comp Neurol 419:306–319. CrossRef Medline

Lee CC, Sherman SM (2008) Synaptic properties of thalamic and intracortical inputs to layer 4 of the first- and higher-order cortical areas in the auditory and somatosensory systems. J Neurophysiol 100:317–326. CrossRef Medline

Li H, Fertuzinhos S, Mohns E, Hnasko TS, Verhage M, Edwards R, Sestan N, Crair MC (2013) Laminar and columnar development of barrel cortex relies on thalamocortical neurotransmission. Neuron 79:970–986. CrossRef Medline

Linderstrøm-Lang K, Holter H, Søeborg Ohlsen A (1935) Studies on enzymatic histochemistry. XIII. The distribution of enzymes in the stomach of pigs as a function of its histological structure. C R Trav Lab Carlsberg 20:66–127.

Lübke J, Egger V, Sakmann B, Feldmeyer D (2000) Columnar organization of dendrites and axons of single and synaptically coupled excitatory spiny neurons in layer 4 of the rat barrel cortex. J Neurosci 20:5300–5311. Medline

Meyer HS, Wimmer VC, Hemberger M, Bruno RM, de Kock CP, Frick A, Sakmann B, Helmstaedter M (2010) Cell type-specific thalamic innervation in a column of rat vibrissal cortex. Cereb Cortex 20:2287–2303. CrossRef Medline

Nahmani M, Erisir A (2005) VGluT2 immunochemistry identifies thalamocortical terminals in layer 4 of adult and developing visual cortex. J Comp Neurol 484:458–473. CrossRef Medline

Nakano K, Tokushige A, Kohno M, Hasegawa Y, Kayahara T, Sasaki K (1992) An autoradiographic study of cortical projections from motor thalamic nuclei in the macaque monkey. Neurosci Res 13:119–137. CrossRef Medline

Nusser Z, Lujan R, Laube G, Roberts JD, Molnar E, Somogyi P (1998) Cell type and pathway dependence of synaptic AMPA receptor number and variability in the hippocampus. Neuron 21:545–559. CrossRef Medline

Oberlaender M, de Kock CP, Bruno RM, Ramirez A, Meyer HS, Dercksen VJ, Helmstaedter M, Sakmann B (2012) Cell type–specific three-dimensional structure of thalamocortical circuits in a column of rat vibrissal cortex. Cereb Cortex 22:2375–2391. CrossRef Medline

Ohana O, Portner H, Martin KA (2012) Fast recruitment of recurrent inhibition in the cat visual cortex. PLoS One 7:e40601. CrossRef Medline

Paxinos G, Franklin KBJ (2004) The mouse brain in stereotaxic coordinates. Amsterdam: Elsevier.

Peters A, Palay SL (1996) The morphology of synapses. J Neurocytol 25:687–700. CrossRef Medline

Peters A, Palay SL, Webster, H (1991) The fine structure of the nervous system: neurons and their supporting cells, Ed 3. New York: OUP.

Porter JT, Johnson CK, Agmon A (2001) Diverse types of interneurons generate thalamus-evoked feedforward inhibition in the mouse barrel cortex. J Neurosci 21:2699–2710. Medline

Sakata-Haga H, Kanemoto M, Maruyama D, Hoshi K, Mogi K, Narita M, Okado N, Ikeda Y, Nogami H, Fukui Y, Kojima I, Takeda J, Hisano S (2001) Differential localization and colocalization of two neuron-types of sodium-dependent inorganic phosphate cotransporters in rat forebrain. Brain Res 902:143–155. CrossRef Medline

Schiff ML, Reyes AD (2012) Characterization of thalamocortical responses of regular-spiking and fast-spiking neurons of the mouse auditory cortex in vitro and in silico. J Neurophysiol 107:1476–1488. CrossRef Medline

Schikorski T, Stevens CF (1997) Quantitative ultrastructural analysis of hippocampal excitatory synapses. J Neurosci 17:5858–5867. CrossRef Medline

Schikorski T, Stevens CF (1999) Quantitative fine-structural analysis of olfactory cortical synapses. Proc Natl Acad Sci U S A 96:4107–4112. CrossRef Medline

Schoonover CE, Tapia JC, Schilling VC, Wimmer V, Blazeski R, Zhang W, Mason CA, Bruno RM (2014) Comparative strength and dendritic organization of thalamocortical and corticocortical synapses onto excitatory layer 4 neurons. J Neurosci 34:6746–6758. CrossRef Medline

Shepherd GM (2009) Intracortical cartography in an agranular area. Front Neurosci 3:337–343. CrossRef Medline

Shinoda Y, Kakei S (1989) Distribution of terminals of thalamocortical fibers originating from the ventrolateral nucleus of the cat thalamus. Neurosci Lett 96:163–167. CrossRef Medline

Shipp S (2005) The importance of being agranular: a comparative account of visual and motor cortex. Philos Trans R Soc Lond B Biol Sci 360:797–814. CrossRef Medline

Shipp S, Adams RA, Friston KJ (2013) Reflections on agranular architecture: predictive coding in the motor cortex. Trends Neurosci 36:706–716. CrossRef Medline

Skoglund TS, Pascher R, Berthold CH (1997) The existence of a layer IV in the rat motor cortex. Cereb Cortex 7:178–180. CrossRef Medline

Somogyi P, Kisvárday ZF, Martin KA, Whitteridge D (1983) Synaptic connections of morphologically identified and physiologically characterized large basket cells in the striate cortex of cat. Neuroscience 10:261–294. CrossRef Medline

Stratford KJ, Tarczy-Hornoch K, Martin KA, Bannister NJ, Jack JJB (1996) Excitatory synaptic inputs to spiny stellate cells in cat visual cortex. Nature 382:258–261. CrossRef Medline

Strick PL, Sterling P (1974) Synaptic termination of afferents from the ventrolateral nucleus of the thalamus in the cat motor cortex: a light and electron microscope study. J Comp Neurol 153:77–106. CrossRef Medline

Swadlow HA (1989) Efferent neurons and suspected interneurons in S-1 vibrissa cortex of the awake rabbit: receptive fields and axonal properties. J Neurophysiol 62:288–308. Medline

Swadlow HA (1990) Efferent neurons and suspected interneurons in S-1 forelimb representation of the awake rabbit: receptive fields and axonal properties. J Neurophysiol 63:1477–1498. Medline

Swadlow HA (2002) Thalamocortical control of feed–forward inhibition in awake somatosensory "barrel" cortex. Philos Trans R Soc Lond B Biol Sci 357:1717–1727. CrossRef Medline

Swadlow HA, Gusev AG (2000) The influence of single VB thalamocortical impulses on barrel columns of rabbit somatosensory cortex. J Neurophysiol 83:2802–2813. Medline

Tanaka J, Matsuzaki M, Tarusawa E, Momiyama A, Molnar E, Kasai H, Shigemoto R (2005) Number and density of AMPA receptors in single synapses in immature cerebellum. J Neurosci 25:799–807. CrossRef Medline

Tennant KA, Adkins DL, Donlan NA, Asay AL, Thomas N, Kleim JA, Jones TA (2011) The organization of the forelimb representation of the C57BL/6 mouse motor cortex as defined by intracortical microstimulation and cytoarchitecture. Cereb Cortex 21:865–876. CrossRef Medline

Varoqui H, Schäfer MK, Zhu H, Weihe E, Erickson JD (2002) Identification of the differentiation-associated Na+/PI transporter as a novel vesicular glutamate transporter expressed in a distinct set of glutamatergic synapses. J Neurosci 22:142–155. Medline

Viaene AN, Petrof I, Sherman SM (2011a) Properties of the thalamic projection from the posterior medial nucleus to primary and secondary somatosensory cortices in the mouse. Proc Natl Acad Sci U S A 108:18156–18161. CrossRef Medline

Viaene AN, Petrof I, Sherman SM (2011b) Synaptic properties of thalamic input to layers 2/3 and 4 of primary somatosensory and auditory cortices. J Neurophysiol 105:279–292. CrossRef Medline

Weiler N, Wood L, Yu J, Solla SA, Shepherd GM (2008) Top-down laminar organization of the excitatory network in motor cortex. Nat Neurosci 11:360–366. CrossRef Medline

White EL (1978) Identified neurons in mouse SmI cortex which are postsynaptic to thalamocortical axon terminals: a combined Golgi-electron microscopic and degeneration study. J Comp Neurol 181:627–661. CrossRef Medline

Winfield DA, Powell TP (1983) Laminar cell counts and geniculo-cortical boutons in area 17 of cat and monkey. Brain Res 277:223–229. CrossRef Medline

Wise SP, Jones EG (1978) Developmental studies of thalamocortical and commissural connections in the rat somatic sensory cortex. J Comp Neurol 178:187–208. CrossRef Medline

Yamamoto T, Kishimoto Y, Yoshikawa H, Oka H (1990) Cortical laminar distribution of rat thalamic ventrolateral fibers demonstrated by the PHA-L anterograde labeling method. Neurosci Res 9:148–154. CrossRef Medline

Yamawaki N, Borges K, Suter BA, Harris KD, Shepherd GM (2014) A genuine layer 4 in motor cortex with prototypical synaptic circuit connectivity. eLife 3:e05422. CrossRef Medline

1.3   Conclusion

1.3.1   Summary

M1 has traditionally been thought to lack the granular L4, which is the principal target for thalamic input in sensory areas. This led to suggestions how M1 could employ different modes of interlaminar processing compared to sensory areas, while the role of thalamic input to M1 has often been largely neglected in these frameworks. Over time, however, accumulating anatomical and physiological evidence has suggested that M1 could in fact also possesses a thin thalamo-recipient middle layer, which in turn inspired speculations that M1 is actually similar to sensory cortex. We reasoned that decisive evidence for the importance of a L4 in M1 should not be the existence of a cytologically-identifiable band of neurons, but rather the anatomical weight and nature of the thalamocortical synapses in the main thalamocortical termination zone in M1. In this study, we used the vesicular glutamate transporter 2 as a reliable and exclusive marker of thalamic presynaptic boutons. We showed that, like S1, mouse M1 also possesses one of the key canonical circuit motifs of core thalamic input to the cortical middle layer and that thalamocortical synapses form a small fraction of all asymmetric synapses in L4 of both areas. This suggests that similar mechanisms for the amplification of thalamic input could be implemented in M1 L4 compared to sensory areas. Intriguingly, however, we found that the thalamic afferents in M1 – unlike those in S1 – do not form synapses with smooth cells (i.e. the GABAergic neurons), which raises interesting questions as to the mechanism of inhibitory gain control in M1. This observation has opened up new avenues of research that are currently followed up by other groups.

1.4   Outlook

1.4.1   Does M1 possess the canonical microcircuit motif?

We showed that M1 possesses the anatomical circuit motif of thalamic input to the middle cortical layer. As in S1, only a small fraction of synapses in L4 originated from the thalamus. However, in M1 L4 only half as many thalamocortical synapses terminated compared to S1 L4. Whether the thalamocortical projection to M1 L4 possesses the same function as in sensory areas is beyond the experimental resolution of this anatomical study.

The canonical microcircuit of the neocortex was discovered by modeling the electrophysiological responses of cortical neurons to a pulse stimulus (Douglas et al., 1989; Douglas and Martin, 1991). Because our study was purely anatomical, we cannot finally conclude that the canonical microcircuit is implemented in M1. The shunning of GABAergic targets by thalamocortical synapses in M1 L4 could indicate a violation of the canonical circuit motif. One of its central elements is the strong recruitment of inhibition, which terminates the polysynaptic wave of excitation that reverberates in the recurrent circuits (Douglas et al., 1989; Douglas and Martin, 1991). This inhibition does not necessarily have to be recruited by thalamocortical synapses, it could also be recurrent inhibition, which is also a key feature of the canonical circuit, but clearly the physiology and the anatomy agree that feedforward inhibition is a hallmark of the thalamocortical input in sensory areas. How excitation and inhibition are balanced in M1 L4 emerged as a central question from our study, which is discussed in more detail below.

We discovered that S1 receives approximately twice as many VGluT2^{+} synapses per unit surface area of cortex compared to M1. To assess whether the thalamic synapses can drive L4 neurons in M1 – as they do in sensory areas, it is important to estimate how many thalamic synapses converge onto a single L4 neuron in M1 in comparison to S1. This number can be computed by dividing the synapse density by the neuron density [see for example (Cragg, 1967; Schüz and Palm, 1989)].

Our NeuN staining revealed that the neuron density in L4 of M1 is lower compared to L4 in S1. Other EM studies have provided quantitative evidence that the neuron density in the motor areas is indeed lower compared to sensory areas in different species (Cragg, 1967), including data on the densities in the middle layers of M1 and V1 in the mouse (Schüz and Palm, 1989).

Thus, the lower VGluT2^{+} synapse density in M1 L4 compared to S1 L4 (0.192 synapses/μm^3, and 0.225 synapses/μm^3, respectively) should coincide with a lower density of neurons in L4 of M1 compared to S1, on which these synapses converge on. Furthermore, VGluT2^{+} boutons in M1 L4 do not form synapses with GABAergic interneurons, which effectively reduces the density of available target neurons in L4 of M1 by 20%.

Taken together, it is probable that a single neuron in L4 of M1 receives comparable absolute numbers of VGluT2^{+} synapses as a L4 neuron in S1. A quick back-of-the-envelope calculation exemplifies this idea: in their EM study in the mouse, Schüz and Palm (1989) provided neuron densities for L4 of M1 and V1 (M1 L4: $13*10^4$ neurons/mm^3, V1 L4: $19*10^4$ neurons/mm^3). If we permit ourselves to borrow these numbers and assume for simplicity that S1 L4 contains similar neuron densities as V1 L4 and if we consider that 20% of these neurons are GABAergic interneurons that are not targeted by VGluT2^{+} boutons in M1, then a single L4 neuron receives 1800 VGluT2^{+} synapses in M1 and only 1200 VGluT2^{+} synapses in S1. Even if we accept a lower proportion of interneurons in M1 L4 (e.g. 10%) – and lower overall neuron densities in S1 L4, as they have been reported by other groups [e.g. $13*10^4$ neurons/mm^3 in (Meyer et al., 2010)], the number of VGluT2^{+} synapses per L4 neuron are roughly unity between S1 and M1 and not larger by a factor of 2 in S1, as the total number of synapses per unit area of cortex might suggest. Thus, thalamic synapses could have a similar driving effect on single L4 neurons in M1 as in S1.

To tackle conclusively the question of whether the canonical microcircuit is implemented in M1, electrophysiology is needed. The experiments by Yamawaki and colleagues (2015) were performed in the slice and thus could not provide sufficient detail about the *in vivo* behavior of the local M1 circuitry. We suggest a similar experiment as Douglas and Martin (1989): the combination of *in vivo* recordings of M1 neurons with stimulation of the motor thalamus or thalamocortical pathway.

1.4.2   Identification of thalamic synapses in S1 without the need for specific labeling

We suggested that our observation that thalamocortical boutons in S1 usually formed multiple synapses (whereas corticocortical boutons usually formed single synapses) could be exploited to identify thalamocortical synapses in S1 L4 with high probability in EM, without the need for specific labeling. Indeed, in a recent dense reconstruction of a volume of 500.000 μm^3 of L4 of mouse S1, our data could be used to successfully distinguish between corticocortical and thalamocortical axons using only measurements of the frequency of multisynaptic boutons, bouton size, and the number of synapses per bouton (Motta et al., 2018).

1.4.3 The lack of feedforward inhibition in the thalamocortical projection to M1

An unexpected and certainly very intriguing observation that emerged from our study was the lack of VGLuT2$^+$ synapses on GABAergic neurons in L4 of M1. Because of the purely anatomical nature of this work, we could only speculate about the implications for the physiological behavior of the circuit. Fortunately, this unexpected qualitative difference between the local circuitry in M1 and S1 has caught the interest of other research groups, who are currently investigating its electrophysiological effects (personal communications with Gordon Shepherd). However, a closer analysis of the comparative anatomy of different long-distance projections may allow us to raise interesting hypothesis, which could be tested with electrophysiological experiments.

Long-range projections that largely avoid GABAergic dendrites are known to exist in at least three pathways in the neocortex: corticocortical feedback projections (Johnson and Burkhalter, 1996), colossal projections (Jones and Powell, 1970; White and Czeiger, 1991; Czeiger and White, 1993) – but for a contrary view, see (Anderson and Martin, 2016) – and the developing thalamocortical system. In the latter, GABAergic inhibition matures during the critical period, when the afferent connections from the thalamus have already been formed. During this period, stimulation of the thalamocortical pathway in slices of rat somatosensory and visual cortex evokes only a monosynaptic EPSP in cells of the middle layers. These early EPSPs contain both a N-methyl-D-aspartate-receptor (NMDAr) and non-NMDAr-mediated component. Importantly, the NMDAr-gated conductance is capable of inducing long-term potentiation (LTP) in the young rat visual cortex. This ability is ultimately lost in the adult thalamocortical pathway, when the GABAergic system is mature (Kato et al., 1991). Then, stimulation of the thalamic afferents causes an EPSP that is immediately followed by a disynaptic inhibitory postsynaptic potential (IPSP). The EPSP triggered in the adult animal is largely lacking a NMDAr-mediated component because the trailing IPSP lowers the membrane potential again and strongly reduces the voltage-gated, long-latency NMDAr conductance (Luhmann and Prince, 1991; Agmon and O'Dowd, 1992). With the loss of the NMDAr-dependent component of the EPSP, the ability to produce LTP ceases. Importantly, it can be rescued by bicuculline, showing that the effect is indeed GABA$_A$-mediated and that NMDAr do remain expressed in the adult thalamocortical pathway (Artola and Singer, 1987).

This raises the intriguing possibility that the shunning of GABAergic targets by the thalamocortical projection reaching L4 of M1 might be a functional preservation of an immature developmental feature, which allows us to speculate about its physiological effects.

Our anatomical findings suggest that EPSPs triggered in M1 L4 pyramidal cells by thalamocortical boutons could likewise lack strong disynaptic inhibition and we may speculate that the NMDAr-dependent component of the EPSP could be retained in this connection. This would constitute a major functional difference to the thalamocortical projection to S1 L4 and could be the footprint of a cellular mechanism, by which the thalamocortical pathway to M1 has preserved the ability for LTP through NMDAr-dependent plasticity.

Intriguingly, at the same time, it could explain the larger average postsynaptic density (PSD) sizes made by thalamocortical boutons on M1 cells: a major mechanism involved in LTP is the activity-dependent increase of the number of AMPA (α-amino-3-hydroxy-5-methyl-4-isoxazolepropionic acid) receptors (AMPAr) in the postsynaptic membrane (Shi et al., 1999, 2001; Hayashi et al., 2000; Takahashi et al., 2003) and the estimated

number of AMPAr in synaptic sites is proportional to the synaptic area in EM (Nusser et al., 1998; Tanaka et al., 2005).

Recently, a study in the mouse has hinted that in the connection from the posterior nucleus of the thalamus (Po) to the superficial layers of M1, NMDAr play a dominant role in activating postsynaptic neurons *in vivo* (Casas-Torremocha et al., 2019).

A further important difference between L4 of M1 and S1, which could have profound functional implications, is that M1 L4 neurons possess an apical tuft that extends into the superficial layers. Therefore, they have access to an additional source of synaptic inputs, which S1 L4 neurons lack. Thus, it is conceivable that we have missed the disynaptic inhibitory mechanism for gain control in the thalamocortical pathway to M1 because it could be implemented via the apical tufts of the L4 pyramidal neurons in the superficial layers.

In this scenario, VGluT2$^+$ boutons should innervate smooth dendrites of interneurons in L1 and L2/3 in a similar fashion as interneurons are innervated in S1 L4. At the same time, apical tufts of L4 neurons should receive direct inhibition from the VGluT2$^+$ innervated interneurons. However, the observed density of VGluT2 staining in the superficial layers was lower than in L4 and unless there is a high specificity of VGluT2$^+$ boutons forming synapses with smooth dendrites in L2/3, the number of thalamic synapses per inhibitory neuron should be small. These suggestions are readily testable with a similar experimental approach as employed by us. In fact, the tissue used in our JNeurosi (2017) paper contains portions of L2/3 and could be reused for this purpose.

To conclude, the question of whether or not the thalamocortical projection to M1 has preserved the ability for LTP through NMDAr-dependent plasticity remains entirely speculative. This question could become relevant with respect to recent findings that have challenged the classical dogma of M1 being the executer of motor skills: Surprisingly, when M1 was lesioned in rats, the animals' performance in producing learned, spatiotemporally precise movement tasks were unaffected (Kawai et al., 2015). (It is important to note that these tasks did not involve dexterity.) Intriguingly, however, the ability to acquire novel motor sequences was entirely lost after lesions. This suggested that subcortical circuits must possess a strong capacity for performing acquired motor skills and that cortex plays a crucial role in acquiring novel motor skills. It is tempting to speculate whether LTP in the thalamocortical projection to M1, which links subcortical to cortical circuits, could contribute to the role of M1 in acquiring novel motor sequences.

On a more abstract explanatory level, the lack of disynaptic inhibition and potential preservation of the ability for LTP could constitute an interesting example of how a canonical circuitry in the brain can adapt to a variety of different functions by tweaking only a few components of its circuit, while preserving its general anatomy and connectivity. Ultimately, this could be a step towards understanding how the canonical microcircuit of neocortex was able to adapt to its mesmerizing variety of different functions, including its ability to mesmerize itself, throughout the course of evolution.

1.4.4 Suggestions for further experiments

To elucidate further the function of the thalamocortical projections to M1, the next experiments could be aimed at identifying the precise physiological responses in adult M1 L4 neurons after activating thalamocortical afferents. It is not trivial to tackle this question experimentally because it is desirable to preserve much of the M1 circuitry and to record subthreshold responses of L4 neurons intracellularly, while selectively blocking NMDAr and AMPAr-mediated components of EPSPs pharmacologically. At the same time, thalamocortical afferents have to be stimulated. These requirements demand an *in vivo* experiment, in which L4 neurons are recorded with whole-cell patch clamp, while the motor thalamus or the white matter below cortex are stimulated electrically. An alternative option is optical stimulation of the motor thalamus following transfection with viral vectors expressing Channelrhodopsin.

In parallel, the targets of VGluT2$^+$ boutons in L1 and L2/3 of M1 could be assessed using a similar anatomical approach as used by us. This could elucidate whether gain control through disynaptic inhibition could be mediated through the apical tufts of L4 pyramidal neurons in M1.

Chapter 2

Structure and function of cortical synapses

2.1 Introduction

In the previous chapter, we investigated the ultrastructural features of thalamocortical and corticocortical synapses. In this chapter, we will tackle the question of how these anatomical features of neocortical synapses relate to the physiological properties of synaptic transmission.

2.1.1 A short history of synaptic transmission

2.1.1.1 Neurone Doctrine and principle of dynamical polarization

One of the most important developments in the history of biology that opened the door to a previously hidden universe was the invention of the microscope. It allowed the early microscopists Antoni van Leeuwenhoek and Robert Hooke to discover unicellular organisms and to observe that plant tissue is made up of discrete entities, which Hooke called "cells" (Hooke, 1664; Gest, 2004). Ultimately, this discovery led to the formulation of the *Cell Theory* by Schwann and Schleiden in 1839 as a unifying framework of biological cells, which continues to be one of the fundamental theories of modern biology. It postulated that all living organisms are made up of cells, that the cell is the basic structural and organizational unit of organisms, and that cells develop from precursor cells (Schwann, 1839; Südhof et al., 2003).

However, some neuroscientists were more reluctant to recognize that this theory should likewise apply to the nervous system and a fierce battle was fought well into the latter part of the 19th century between the supporters of the *Neuron Doctrine* and the camp of the *reticularists* (Südhof et al., 2003).

The Neurone Doctrine emerged conceptually from the experimental observations of several anatomists including Waldeyer, Forel, His, Kölliker, Retzius, Gudden, and van Gehuchten (Jones, 1994; Südhof et al., 2003). Its most prominent advocate and contributor, who is often cited as its sole originator (DeFelipe and Swanson, 2017), was the famous Spanish anatomist Santiago Ramón y Cajal. Cajal employed the chrome silver impregnation technique that had been developed by Camillo Golgi in 1873 and which is often referred to as the *reazione nera*, because it produces a black precipitate in the labeled neurons. The method labels randomly a very small fraction of neurons and thus allows to study the morphology of individual cells. Depending on the preparation, it can stain the neuron's entire neurites and thus reveals the different cellular specializations, such as the cell body, dendrites, axons, or growth cones (Südhof et al., 2003). Through his life, Cajal produced an impressive collection of almost 3000 drawings from his microscopic observations. These drawings are of remarkable accuracy and exceptional artistic beauty and enabled Cajal to arrive at a deep conceptual understanding of the microanatomy of the brain (DeFelipe and Swanson, 2017). Amongst many other things, Cajal realized that axon terminals in many different brain regions

ended freely on the surface of other cells and that they were discontinuous with the neuron they impinged on [(Ramón y Cajal, 1937), but see (Südhof et al., 2003)].

The Neurone Doctrine implied that the nerve impulses had to be transmitted through the contact points made between two neurons and also in this domain Cajal contributed an important concept by supporting the *Principle of Dynamic Polarization*, first formulated by van Gehuchten. It proposed that nerve impulses flow in a directional manner through neurons: they originate in the dendrites and flow through the cell body and into the axons, from where they are transmitted to other neurons (Südhof et al., 2003). This principle is manifested in Cajal's drawings as arrows that indicate the direction in which nerve impulses are transmitted through neuronal circuits (DeFelipe and Swanson, 2017).

The reticularists' view opposed the Neurone Doctrine and proposed that the nervous system did not consist of segregated neurons, but that it was instead composed of a syncytium, in which the axons and dendrites of neurons where continuous with the axons and dendrites of the neighboring neurons (Südhof et al., 2003). The theory had powerful supporters, including – most prominently – Camillo Golgi himself. It is remarkable that Cajal and Golgi arrived at opposing conclusions given that they employed the same method, in particular as this happened in the acceptance speeches they delivered back-to-back when they were jointly awarded the 1906 Nobel Prize in Physiology and Medicine [Robert Tigerstedt in (Granit, 1966) (Douglas and Martin, 2007)]. Despite the fact that unequivocal morphological evidence for the Neurone Doctrine emerged only with the advent of EM 50 years later (Palay and Palade, 1955; Robertis and Bennett, 1955), it was widely accepted by the end of the 19th century (Südhof et al., 2003).

The Neurone Doctrine and Principle of Dynamic Polarization raised an intriguing question that has occupied neuroscientists to this day: what happens at the contact points between neurons? Many of the scientists that embarked on the endeavor to answer this question have become neuroscience legends and their paths towards understanding synaptic transmission have been paved with Nobel Prizes (Südhof et al., 2003).

2.1.1.2   *Sherrington's synapsis*

These contact points eventually received their euphonious name "synapse" from Charles Sherrington (Foster and Sherrington, 1897), who was a strong advocate of Cajal in defending the Neurone Doctrine (Südhof, 2013). The concept of the synapse was a means for explaining the *busy time*, a brief delay in the latency of reflexes, which could not be accounted for by the conduction velocity of impulses through the neurites. Sherrington's physiological studies on the spinal reflex arcs formed by muscle spindles onto lower motor neurons laid many of the foundations for future discoveries on synaptic transmission and won him the 1932 Nobel Prize in Physiology or Medicine (Südhof, 2013). For example, he noted that *"… each synapse offers an opportunity for a change in character of nervous impulses, that the impulse as it passes over from the terminal arborescense of an axon into the dendrite of another cell, starts in that dendrite an impulse having characters different from its own, …"* [(Foster and Sherrington, 1897), p. 969].

From his studies, Sherrington appreciated the unidirectional flow of nerve impulses across the synapse and understood that each afferent fiber contributes only a mild effect to the activation of the downstream motor neuron and that temporal summation of signals from many afferent fibers was necessary for the motor neuron to discharge itself. He realized that all motor signals ultimately converge onto lower motor neurons, which he termed the *final common pathway*. One of his most important contributions was evidence that central inhibition was an active phenomenon. From studies on reflexes involving flexor and extensor muscles, Sherrington realized that excitation of a muscle was always accompanied by inhibition of the antagonistic muscles (Sherrington, 1906, 1908a, 1908b; Südhof et al., 2003).

2.1.1.3   The soup versus spark controversy

The question of whether synaptic transmission is mediated by electrical signals or by chemical compounds dates back to the late 19th century and initiated one of the fiercest controversies in the young field of neuroscience. Neuropharmacologists injected animals with extracts from glands or plants (including compounds like nicotine and adrenaline) while monitoring physiological effects, such as changes of heart rate or blood pressure, and responses of musculature. They concluded that chemical compounds were responsible for the transmission of signals at synapses. In the meantime, electrophysiologist objected: they probed physiological responses that could be elicited by electrical stimulation and reasoned that synaptic transmission must be mediated electrically (Südhof et al., 2003).

The saga holds that the tide-shifting experiment was finally dreamed of by Otto Loewi in his sleep. Loewi isolated two beating frog hearts in Ringer solution and electrically stimulated the afferent vagus nerve of one heart. He observed the well-characterized inhibitory effects of vagus stimulation, such as a slowing of the heart rate. Loewi now transferred some of the Ringer solution from the stimulated heart to the unstimulated heart and observed the same slowing of the heart rate. The transferred Ringer solution must have contained an unknown chemical compound, which Loewi called "Vagusstoff" that mediated the signal transmission between the vagus nerve and the heart muscle. Later, this compound was characterized by Henri Dale to be acetylcholine (ACh) and Dale and Loewi shared the 1936 Nobel Prize for their discoveries (Eccles, 1982; Südhof et al., 2003).

The serendipity of Loewi's discovery is remarkable: his experiment was allegedly conducted on Easter Sunday 1921, at a time of year when the cholinesterase content in amphibian hearts is low, a mechanism to allow increased inhibition of the cardiovascular system during hibernation. The low cholinesterase levels in the heart neuromuscular junction (NMJ) permitted the released ACh to remain active and exert its inhibitory effect also on the second heart (Südhof et al., 2003).

However, the *soup versus spark controversy* was not settled until the 1950s. The NMJ of skeletal muscles showed much faster conduction times (~ 1 ms) compared to that of the heart (~ 100 ms), and these were assumed to be too short to allow for chemical diffusion. Also, the beautifully clear experiments at the easy-to-isolate NMJ could not be carried out at central synapses (Eccles, 1982; Südhof et al., 2003).

The matter was finally resolved by Eccles in a heroic and ingenious act of self-falsification, which would eventually win him the 1963 Nobel Prize. Influenced by the philosopher Karl Popper, Eccles used his models of

how inhibition could be implemented by electrical transmission to produce hypotheses that were experimentally testable. The advent of intracellular recordings allowed Eccles to record from lower motor neurons while stimulating inhibitory afferents (a central synapse). His results were incompatible with his own theory of electrical transmission and Eccles immediately abandoned his views without reservation and suggested that also excitation should be carried by chemical transmission (Eccles, 1982; Südhof et al., 2003).

2.1.1.4   The quantal hypothesis of synaptic transmission

With the controversy of electrical versus chemical transmission settled, the mechanics behind synaptic release became a focus of research (Südhof, 2013). Bernard Katz, a former student of Eccles, and Paul Fatt used the same intracellular recording techniques as Eccles, but on the NMJ of skeletal muscles in the frog and made several key discoveries that would define our modern understanding of synaptic transmission. They found small, spontaneously occurring depolarizations of the muscle fiber in the absence of stimulation of the afferent motor neuron. These miniature end-plate potentials (mEPP) were of discrete size and Fatt and Katz concluded correctly that they occurred because fairly large, but discrete quantities of ACh were released from the presynaptic terminal by chance (Fatt and Katz, 1950, 1951). In a subsequent experiment, del Castillo and Katz lowered the calcium concentration of the extracellular medium, because they had found that then the end-plate potential (EPP) amplitude declined and approached the amplitude of the mEPP, which remained unaffected by the decreased calcium concentration (Fatt and Katz, 1952). Under these conditions, stimulation of the motor neuron evoked EPPs that varied in amplitude in a stepwise, *quantized* manner. Each EPP was an integral multiple of the mEPP amplitude. Thus, by lowering the calcium concentration, an increasing number of quanta were blocked from being released in an all-or-none manner (del Castillo and Katz, 1954a).

From these and subsequent experiments, which resulted in Bernard Katz's winning of the Nobel Prize in 1970, the modern *quantal hypothesis* was developed. It states that neurotransmitter is released in discrete, quantized multimolecular packages in an all-or-none manner and that release of each quantum is probabilistic. In the event of an action potential, multiple quanta are released simultaneously and their effect summates in the postsynaptic structure (del Castillo and Katz, 1954a, 1954b; Südhof et al., 2003).

The subsequent advent of EM in neuroscience showed that presynaptic and postsynaptic structures were indeed separated by a thin physical cleft and that the presynaptic nerve terminals contained synaptic vesicles, which provided impressive visual validation for both the quantal hypothesis and the Neurone Doctrine (Palay and Palade, 1955; Robertis and Bennett, 1955; Südhof et al., 2003).

Today we know that when the synaptic terminal is depolarized by an action potential, voltage-gated calcium channels proximal to vesicle fusion pores open and calcium enters the terminal and binds to the transmembrane protein synaptotagmin. The un-ligated synaptotagmin forms a ring around the SNARE-complex that prevents the primed vesicle from fusing with the plasma membrane. When synaptotagmin binds calcium, it undergoes a conformational change that ultimately enables the fast release of the energetically primed vesicle (Südhof et al., 2003; Südhof and Rothman, 2009; Südhof, 2013). Also this research has resulted in the awarding of a Nobel Prize in Physiology and Medicine (to Thomas Südhof, James Rothman, and Randy Schekman in 2013).

2.1.1.5   Quantal Analysis

Much of the groundbreaking work that would define our understanding of synaptic transmission was conducted at the NMJ. The NMJ is a specialized synapse, optimized to evoke movement reliably and it differs significantly in several ways from synapses in the central nervous system and in the neocortex. For example, a single action potential in the ascending motor neuron causes EPPs of ~ 70 mV under normal conditions, which elicit action potentials in the innervated muscle fiber. The reliability is achieved because a large number of "unreliable" quanta can be released simultaneously (Kandel et al., 2000; Südhof et al., 2003).

Amplitude responses of postsynaptic potentials or currents can be described in statistical terms using three *quantal parameters*: the maximum number of quanta that can be released simultaneously is called the *number of release sites*, N. The probability of release of each quantum in the event of an action potential is termed *release probability*, P. The electrical effect that a single quantum exerts on the postsynaptic structure is the *quantal size*, Q. The statistical methods to extract these quantal parameters from recordings of evoked synaptic potentials or currents is referred to as *quantal analysis* and was pioneered by del Castillo and Katz. It allowed them to establish that release at the NMJ under low extracellular calcium concentrations can be statistically captured with Poisson law (del Castillo and Katz, 1954a, 1954b; Korn et al., 1981).

   At the muscle, the axon of the motor neuron branches extensively and each branch forms several synaptic boutons with a specialized region of the muscle membrane, called *end-plate*. Each bouton contains multiple active zones, from which synaptic vesicles are released. Below the bouton, the end-plate forms invaginations (junctional folds), which increase the membrane surface to house a high number of ACh receptors. This design enables a high capacity for releasing vesicles simultaneously: the NMJ is capable of *multivesicular release* (Kandel et al., 2000; Südhof et al., 2003).

The NMJ provided several advantages for quantal analysis, which are not present at central synapses. Each muscle fiber is innervated by a single nerve and thus it is possible to obtain mEPP recordings and evoked EPP recordings from the same synapse. The mEPP amplitudes can then be used to obtain a measurement of Q. Furthermore, the preparation is easily accessible and the recording pipette can be placed proximal to the end plate, which allows for electrotonically close recordings (Redman, 1990).

   When researchers turned their attention towards understanding transmission at central synapses, they developed a battery of quantal analysis methods that circumvented the experimentally more challenging preparation. Some of these methods will be mentioned in the *Discussion*. It became apparent that release at many central synapses was better described with binomial statistics, of which the Poisson law constitutes a limiting case (when N is high and P is low) (Korn et al., 1981). Central synapses – and in particular synapses in the neocortex – tend to possess fewer release sites in comparison to the NMJ, although also some specialized synapses in the central nervous system have exceptionally large pools of readily-releasable vesicles, such as ribbon synapses in the retinal photoreceptors and hair cells and the Calyx of Held in the auditory brainstem (Kandel et al., 2000; Sakaba et al., 2002; Südhof et al., 2003).

   Today, many synapses in the neocortex have been characterized with different forms of quantal analysis. The synaptic connections between excitatory neurons are much weaker than the connection of the motor nerve

with the muscle fiber; in rodents and felines, the EPSPs they evoke are typically on the order of 0.1 to 4 mV. They usually contain on the order of $1-20$ release sites and can operate under a wide range or release probabilities. Quantal sizes typically range between 0.1 and 0.6 mV [see for example (Feldmeyer et al., 1999, 2006; Silver et al., 2003; Hardingham et al., 2006, 2007, 2010; Ohana et al., 2012; Rollenhagen et al., 2018)]. Like at the NMJ, these values reflect the particular functional specializations of neocortical synapses: single pyramidal neurons receive several thousand synapses from hundreds to thousands of different presynaptic neurons – none of which can drive the postsynaptic neuron to discharge single-handedly. The firing of the postsynaptic neuron is determined by the integration of many presynaptic inputs (Koch, 2004).

A rich body of literature is dedicated to link the range of synaptic efficacies and distributions of quantal parameters of neocortical synapses to the functional properties of the circuits they are embedded in (see references in this section). However, our understanding of how the physiological properties of transmission relate to the anatomical phenotype of neocortical synapses, as seen in the EM, remains very limited.

2.1.2   The missing link between structure and function of neocortical synapses

2.1.2.1   The pillars of the ultrastructural world

In search for an explanation of how the thalamic input to M1 could shape cortical processing in M1, we set out to investigate the anatomical substrate of this connection. We counted the number of synapses made by thalamic axons and measured their PSD areas, as an indicator for anatomical "weight". Finally, we compared our data between two areas, because we understand the function of the thalamic input to one area (S1) better than the function of the thalamic input to the other area (M1). From this comparison, we inferred what the function of the thalamocortical projection to M1 could be.

The logic behind this approach assumes that the physiological strengths of thalamocortical synapses are encoded in their anatomical phenotype, in particular their size. At the same time, this same encoding is expected to be conserved between thalamocortical synapses in S1 and M1. This assumption is certainly not without merit and several experimental observations, which are described in the following sections, point to the fact that in particular the PSD area most likely correlates with the strength of synaptic transmission.

However, conclusive experimental validation is lacking of how the anatomical features of neocortical synapses might relate to their physiological properties of transmission. Therefore, it remains experimentally unproven that quantitative EM studies at synaptic resolution, such as the one performed here, can provide any insights about the physiology of the underlying circuit.

2.1.2.2   Implications for systems neuroscience

The work described in chapter 1 constitutes a quantitative EM study on a small scale and was conducted from sparse reconstructions. Recent technological developments have made it feasible to acquire complete wiring diagrams (micro-connectomes) of extended brain volumes at synaptic resolution using EM. While the missing experimental validation of the structure-function relationship of neocortical synapses constitutes an experimental caveat of sparse-reconstruction studies on small-scales (as ours), it could emerge as a profound limitation for the multi-million-dollar industry of connectomics, which has been founded on the promise that the full anatomical

reconstructions of entire brain regions will inform about the function of the circuitry that is embedded in these brain regions.

The fact that inferences about function from synaptic structure remain largely speculative results in two profound caveats for systems neuroscience. (1) It remains experimentally unconstrained whether a connectome – and in fact quantitative EM studies at synaptic resolution in general – can inform about the physiology of the underlying circuit. (2) Experimental data is lacking that would be necessary to calibrate a connectome or sparse reconstructions in such a way that the physiological behavior of the underlying circuits could be simulated.

The field of micro-connectomics currently remains at an early state, where it is focused on producing quantitative descriptions and statistics of selected features of connectivity within a large and densely-reconstructed brain volume [see for example (Mishchenko et al., 2010; Kasthuri et al., 2015; Motta et al., 2018)]. However, in particular when connectomicists will turn towards generating quantitative simulations of reconstructed brain circuits to explain brain function, the question of whether and how anatomical synapse size can be translated into physiological properties will become pertinent (personal communication with Moritz Helmstaedter). For such simulations, structure-function data will be needed to tune and calibrate models in such a way that their physiological behavior could be interpreted in a meaningful way.

2.1.3 Current evidence for structure-function relationships

Several synaptic structure-function relationships have been elucidated, which indicate how anatomical features of synapses seen in the EM relate to some of the physiological properties of synaptic transmission.

2.1.3.1 Release probability

In hippocampus and barrel cortex, the size of the active zone in the presynaptic terminal determines the number of membrane-bound vesicles in the readily-releasable pool (RRP) and the physiological neurotransmitter release probability is positively correlated with active zone size and the number of docked vesicles (Harris and Stevens, 1989; Branco and Staras, 2009; Matz et al., 2010; Holderith et al., 2012; Rollenhagen et al., 2014).

2.1.3.2 The number of AMPA receptors

On the postsynaptic side, the number of AMPAr has been estimated and the estimates have been found to be proportional to the area of the PSD in hippocampal and cerebellar synapses (Nusser et al., 1998; Tanaka et al., 2005).

2.1.3.3 Other observations

Since the area of the active zone in the presynaptic bouton is identical with the area of the PSD in the dendrite (Schikorski and Stevens, 1997, 1999; Murthy et al., 2001; Rollenhagen et al., 2014, 2018), the active zone area is also directly related to the number of postsynaptic receptors and – vice versa – the PSD area is related to the number of bound vesicles in the presynaptic bouton and the release probability.

An additional important observation is that when EPSPs are evoked between synaptically connected neocortical pyramidal neurons, their amplitudes typically span an order of magnitude and follow roughly a log-normal distribution [see for example (Hardingham et al., 2010)]. Likewise, the PSD sizes of synapses in the cerebral cortex span an order of magnitude and also follow lognormal statistics (Harris and Stevens, 1989; Schikorski and Stevens, 1997, 1999; Bopp et al., 2017).

Unfortunately, how many vesicles are released by presynaptic boutons at neocortical synapses in the event of an action potential is a much more debated question. As will be discussed in detail below, this question is central for reconciling how structure and function should relate at single synapses.

2.1.3.4   The search for the release site

Historically, central synapses have been believed to release only a single vesicle. First evidence for the *one-site one-vesicle hypothesis* was based on the observation that N made by inhibitory synapses onto the goldfish Mauthner cell matched the number of appositions between presynaptic axon and the postsynaptic dendrites in the light microscope (LM) (Korn et al., 1981). In retrospect, a concern with this study, which challenges its interpretation, is that the method of fitting binomial models to EPSP histograms that display equally-spaced peaks is associated with a large error in predicting N (Hardingham et al., 2010). This error should be reflected as large variability associated with N, but the data of Korn et al. (1981) are very clean and a surprisingly precise one-to-one relationship of physiological N and number of LM contacts emerged. Similar results were obtained for excitatory connections onto interneurons in rodent hippocampus (Gulyás et al., 1993; Buhl E H et al., 1997; Biró et al., 2005) and between excitatory neurons of several layers of sensory cortex (Silver et al., 2003; Hardingham et al., 2010). Intriguingly, it was noticed that within single experiments, often the estimate of N did not match the number of LM appositions and that the relationship emerged only from averages across experiments (Biró et al., 2005).

Compelling experimental evidence for multivesicular release emerged for excitatory synapses made ono CA1 pyramidal neurons in the hippocampus (Oertner et al., 2002; Christie and Jahr, 2006), excitatory synapses on cultured hippocampal neurons (Tong and Jahr, 1994) and climbing fiber-Purkinje cell synapses in the cerebellum (Christie and Jahr, 2006), when it was discovered that increasing the release probability led to an increase in the concentration of glutamate in the synaptic cleft. Thus, multiple vesicles had to be released at single anatomical synapses under high release probabilities (Tong and Jahr, 1994; Wadiche and Jahr, 2001; Oertner et al., 2002; Christie and Jahr, 2006).

At the same time, new biophysical insights allowed scientists to refine their computer simulations of synaptic release events and receptor binding [see for example (Rosenmund et al., 1998; Smith and Howe, 2000)]. Newer simulations that incorporated these data overruled the original verdict: activated AMPAr resided only within a hotspot of 250 nm diameter around the vesicle fusion pore, while AMPAr outside the hotspot were not bound. Because typical synapse sizes far exceed the area of activation hotspots, they were predicted to include multiple release sites (Franks et al., 2002, 2003; Raghavachari and Lisman, 2004). These models also revealed that the quantal variability of postsynaptic responses following release of single presynaptic vesicles was strongly

dependent on the location of the release event on the postsynaptic membrane and on the overall shape of the active zone-PSD complex (Franks et al., 2003). This is an important finding given the rich myriad of different PSD sizes and shapes that are observed in the neocortex. PSD areas span an order of magnitude in size and larger synapses have the tendency of forming PSDs with complex shapes, most prominently perforations, which must act as barriers for the diffusion of glutamate across the synaptic cleft (Peters et al., 1991; Peters and Palay, 1996; Bopp et al., 2017).

Captivating visual confirmation for multivesicular release has now emerged through the advent of super-resolution microscopy and the discovery that AMPAr are organized in multiple dense clusters in synapses of the hippocampus, called *nanodomains*. The number of nanodomains per synapse is strongly correlated with PSD area (Fukata et al., 2013; MacGillavry et al., 2013; Nair et al., 2013). Intriguingly, nanodomains are intricately aligned to presynaptic fusion pores through scaffolding proteins in so-called *trans-synaptic nanocolumns* (Tang et al., 2016; Haas et al., 2018). When this alignment is disrupted, the strength of synaptic transmission is reduced, suggesting that the tight alignment is critical for synaptic function (Haas et al., 2018). In conjunction with the modeling studies suggesting glutamate concentrations are sufficient to open AMPAr only proximal to fusion pores, this is compelling evidence that trans-synaptic nanocolumns could constitute the anatomical substrate of release sites as measured through quantal analysis.

Despite overwhelming support that the *modus operandi* of synapses between excitatory hippocampal neurons is multivesicular release, evidence for neocortical synapses remains elusive and contradictory. Correlating quantal analysis with anatomical reconstructions in rodent barrel cortex showed that for the excitatory connections between L4 spiny stellate cells and L2/3 pyramidal cells (Silver et al., 2003) and between L2/3 pyramidal cells (Hardingham et al., 2010) the average N was not significantly different from the number of axodendritic appositions seen in LM ("putative synapses"). Hence, it was postulated that only a single vesicle was released per anatomical synapse and that each active zone contains only a single release site. A drawback of these studies was that EM was used to confirm the existence of synapses only on a small subset of experiments and that the images were self-admittedly compromised by the electron-dense biocytin reaction-product (Silver et al., 2003).

Furthermore, these and related structure-function studies were built on the strong assumption that almost all axodendritic appositions seen in LM are anatomical synapses, or in other words, that most putative synapses in fact are real synapses (Markram et al., 1997; Feldmeyer et al., 1999, 2002, 2006; Lübke et al., 2003; Silver et al., 2003; Hardingham et al., 2010). An insightful calculation showing that this is incorrect was carried out by Reimann et al. (2015): if an artificial brain was constructed containing neuron densities as found in the cortex and in which all axodendritic appositions observed in biology were converted to synapses, estimated synapse densities would exceed biological observations by a factor of 18 (Reimann et al., 2015).

Anatomists have captured this important observation with the concept of the *potential synapse*. This is a location in the neuropil, at which an actual synapse could be formed; the essential criterion being that an axon passes a dendrite within the radius of a spine length. Importantly, the ratio of synapses on a dendrite to the potential synapses of the dendrite (called *filling fraction*) has been quantified for rodent hippocampus and cortex

and is a relatively uniform number, ranging between 0.22 and 0.34 (Stepanyants et al., 2002; Stepanyants and Chklovskii, 2005).

Furthermore, the studies that related the number of release sites with the number of putative synapses and concluded that each active zone contains only a single release site are contradicted by work that have produced evidence for multivesicular release also in neocortex, for example between L5 pyramidal neurons in rat barrel cortex (Prange and Murphy, 1999; Loebel, 2009; Rollenhagen et al., 2018).

In conclusion, it still remains an open question how many vesicles are released by neocortical synapses in the event of an action potential. As will be discussed in the following sections, this question is central for hypothesizing how the observed structure-function dependencies should relate to the strength of transmission at single neocortical synapses.

2.1.4   The gaps in our understanding of synaptic structure-function relationships

The previous sections highlight several limitations in our understanding of how the anatomical phenotype of neocortical synapses relates to the physiological properties of synaptic transmission and whether and how quantitative EM studies at synaptic resolution can inform about the physiology of the reconstructed synapses:

(1)   Ultimately, the physiologically most meaningful metric is the strength of synaptic transmission, which is the product of all three quantal parameters and can be measured experimentally as the EPSP amplitude that is elicited in the postsynaptic neuron upon action potential stimulation in the presynaptic neuron. Unfortunately, it remains experimentally entirely unconstrained whether large synapses produce indeed "strong" EPSPs and small synapses produce indeed "weak" EPSPs. Very importantly, also the question needs to be answered of what the precise size-strength relationship is, or in other words: what is the EPSP amplitude of a synapse, given its PSD area?

(2)   Much of the available data for the structure-function relationship of neocortical synapses are derived from circumstantial evidence and were acquired in different brain areas.

(3)   Only few of the quantal parameters have been comprehensively mapped onto the anatomy of synapses of the cerebral cortex within the same experiment.

(4)   There remains a question mark about the interpretation that single anatomical synapses in neocortex contain only a single vesicle release site, which continues to be a dogma in systems neuroscience. As will become clear from the following section, the question of whether neocortical synapses are capable of multivesicular release or if they release only single vesicles is central to reconciling how the other quantal parameters can be mapped onto the anatomical features of neocortical synapses.

Thus, relating structure and function is not only crucial for identifying functional correlates of synapse anatomy for quantitative EM approaches, it also holds the potential for gaining a deeper understanding of synaptic transmission in the neocortex.

2.1.5 Structure-function relationships should depend on the mode of vesicle release

To reconcile how the observed structure-function dependencies could relate to the strength of transmission at single anatomical synapses in the neocortex, it is important to understand the mode of vesicle release and receptor saturation. Specifically, the key lies in understanding how many release sites exist per active zone in a single anatomical synapse.

The *one-site one-vesicle hypothesis* states that a maximum of one vesicle can be released at a single synapse (Wadiche and Jahr, 2001). This implies that either all postsynaptic receptors are saturated following release of only a single presynaptic vesicle (Redman, 1990; Korn and Faber, 1991) or that a cellular mechanism is implemented that prohibits more than one vesicle from being released in the event of an action potential (Tong and Jahr, 1994).

In the first case, it would be experimentally indistinguishable whether one or multiple vesicles were released per action potential, as receptor saturation would produce a stereotyped quantal current at the synapse. If all postsynaptic receptors were saturated from release of a single vesicle, Q should be determined by the total number of AMPAr in the PSD. Because the number of AMPAr scale with PSD area, Q is predicted to correlate with PSD area (Lim et al., 1999).

The alternative scenario of a cellular mechanism to prohibit multivesicular release seems highly unlikely for two reasons: at most neocortical synapses, multiple membrane-bound vesicles can be identified in EM, which are thought to comprise the RRP (Rollenhagen and Lübke, 2006; Rollenhagen et al., 2018) and PSD areas of neocortical synapses span an order of magnitude, which would not be required in this scheme.

In both scenarios, the number of release sites should match the number of anatomical synapses of a connection. Thus, the transmission strength at a single anatomical synapse would depend only on Q and P, while N would be determined by the number of anatomical synapses.

If, on the other hand, the neurotransmitter content of a single vesicle would not suffice to saturate the postsynaptic receptors, multiple release events within the same anatomical synapse would lead to a larger number of occupied postsynaptic receptors compared to the release of only a single presynaptic vesicle, because elevated glutamate concentrations in the synaptic cleft would cause increased receptor binding.

If we assume – for simplicity – the special case that only a single anatomical synapse capable of multivesicular release is formed between two connected neurons, then all three quantal parameters could be anatomically mapped onto this single synapse. In binomial statistics, the EPSP amplitude is simply the product of the three quantal parameters and therefore, the PSD area should correlate with EPSP amplitude and not with Q.

In the case when multiple anatomical synapses were formed by a connection, the cumulative PSD area should correlate with EPSP amplitude and the number of release sites should exceed the number of anatomical synapses. It is important to notice that also under the one-site one-vesicle hypothesis, the cumulative PSD area of all individual synapses should correlate with the EPSP amplitude. The distinctive difference is that if multivesicular release is taking place, fewer anatomical synapses would be formed by a connection and the number of release sites would significantly exceed the number of anatomical synapses.

To conclude, we hypothesize that if single anatomical synapses contain only a single release site, the PSD area would likely correlate with Q. If, on the other hand, an anatomical synapse contains multiple vesicle release sites, N should exceed the number of anatomical synapses and the PSD area should correlate with the EPSP amplitude in the case when only a single synapse is formed – and with the cumulative PSD (cPSD) area in the case of connections comprised of multiple synapses.

Thus, the question of whether and how EPSP amplitude can be predicted from the anatomical phenotype of neocortical synapses and the question of whether these synapses are capable of multivesicular release are mechanistically linked and can be answered together.

2.1.6 Experimental challenges of relating structure and function

Several groups have attempted to relate structure and function of neocortical synapses, but have prematurely terminated their efforts (personal communications with Moritz Helmstaedter and Kevan Martin).

Experimentally, this requires first to record transmission through a single or few synapses physiologically and then to recover all recorded synapses in the EM and measure their anatomical features.

On the physiology side, paired *in vitro* patch-clamp recordings of synaptically connected neurons offer several advantages over optical methods. Electrical stimulation of the presynaptic neuron enables greater precision in time and magnitude than optical stimulation techniques, such as glutamate uncaging (Tanaka et al., 2005; Ellis-Davies, 2007, 2019). Likewise, the resolution of whole-cell electrophysiology and the fact it records subthreshold voltage changes directly, which are the physiologically relevant signal for neuronal firing, makes it desirable to record synaptic transmission with an intracellular electrode. Optical recording methods, such as calcium imaging, allow to image single spines (Oertner et al., 2002; Nimchinsky et al., 2004), but produce indirect measurements, which are difficult to calibrate against the membrane potential (Canepari et al., 2008). At the same time, calcium imaging records NMDAr-mediated currents and not the AMPAr component of the EPSP (Oertner et al., 2002; Nimchinsky et al., 2004).

However, slice recordings of synaptically-connected neurons contain drawbacks of their own, not least because much of the circuit has been lost, which results – amongst other difficulties – in a low probability of finding connected neurons. The major bottleneck, however, is combining slice electrophysiology with EM. Extended recording durations and the artificial nature of the pipette recording solution that dialyses the neuron and of the artificial cerebral fluid, in which slices are incubated in, usually cause severe structural damage of the recorded neurons and the surrounding neuropil [for example (Ohana et al., 2012)]. Following the electrophysiology, biocytin that has been added to the intracellular solution is visualized through histochemistry to allow the identification and reconstruction of the recorded neurons. Complete fillings of both the presynaptic and postsynaptic neuron are essential to ensure that all recorded synapses can be recovered, which requires the use of high biocytin concentrations. The product of the reaction is an electron-dense precipitate, which in turn obscures synaptic membrane specializations in presynaptic bouton and postsynaptic spine (Markram et al., 1997; Feldmeyer et al., 2002, 2006; Silver et al., 2003; Rollenhagen et al., 2018) – probably more severely so if biocytin is used in high concentrations.

Thus, relating structure and function of single synapses by combining whole-cell recordings and EM can only be successful if several, partly conflicting antagonistic experimental requirements are balanced to find an

optimal equilibrium that enables both sufficient recordings and high-quality ultrastructure to recover all recorded synapses and measure their anatomical features.

With these considerations in mind we set out to bridge the gap in our understanding of how the anatomical features of single synapses seen in the EM correlate with their physiological strength in one of today's most in-depth studied brain regions – L2/3 of mouse barrel cortex. Our results are laid out on the following pages.

2.2 Methods

2.2.1 Slicing

Slices were obtained from adult male B6/C57 mice between postnatal days 21 to 40 under the license of K.A.C.M. (approved by Cantonal Veterinary Office, Zurich). Briefly, animals were anesthetized with isoflurane and quickly decapitated, their brains were removed and sliced in ice-cold artificial cerebrospinal fluid (ACSF; containing, in mM, 87 NaCl, 75 sucrose, 26 $NaHCO_3$, 2.5 KCl, 1 NaH_2PO_4 , 0.5 $CaCl_2$, 7 $MgSO_4$, 10 glucose and continuously oxygenated with 95% O_2 , 5% CO_2). We used a para-coronal slicing angle optimized to maintain apical dendrites oriented in parallel to the cutting plane, which greatly enhanced the probability of finding connected neurons. 300 µm thick sections were allowed to recover in oxygenated recording ACSF (containing, in mM, 119 NaCl, 2.5 KCl, 26 $NaHCO_3$, 1.25 NaH_2PO_4 , 1.3 $MgSO_4$, 2.5 $CaCl_2$, and 10 glucose constantly perfused with a mixture of 95% O_2 and 5% CO_2) warmed to 36 °C for 30 minutes and then transferred to room temperature (RT).

2.2.2 Electrophysiology

A crucial technical necessity of the study was to recover axons and dendrites of recorded cells completely and prevent structural damage to preserve the ultrastructure for subsequent EM. We achieved this by intricately optimizing the composition of pipette solution and the shape of recording pipettes. The pipette solution contained, in mM: 115 K-Gluconate, 20 KCl, 2 Mg-ATP, 2 Na-ATP, 10 Na-Phosphocreatin, 0.3 GTP, 10 Hepes, the pH was set to 7.2 with KOH. In a subset of experiments, K-Gluconate was decreased to 105 mM to allow us to increase the biocytin concentration. High biocytin concentrations (~ 1%) were found to greatly enhance complete fillings.

The osmolarity of the pipette solution including biocytin was adjusted to 290–300 mOsm, which slightly exceeded the osmolarity of the recording ACSF and greatly reduced rapid swelling of dendrites while allowing for complete diffusion of biocytin throughout fine neurites. No significant differences in input resistance and membrane time-constants were found between the two recording conditions. Patch pipettes were pulled from borosilicate capillaries (1.5 mm outer diameter, 1.17 mm inner diameter, Warner Instruments) using a P-97 Flaming/Brown micropipette puller (Sutter Instrument). Pipettes with elongated tapers significantly reduced swellings of dendrites. Pipette tip diameters ranged between 2-3 µm and pipette resistance was between 6 and 8 MOhm.

Slices were placed in a submersion chamber and constantly perfused with warmed, oxygenated ACSF (2-3 ml/min), the temperature at the center of the chamber was maintained at 33–35 °C. Cells were visualized under an upright microscope (Olympus BX61W1) equipped with infrared differential-interference contrast (IR-DIC) optics and 10x and 60x water-immersion objectives. Whole-cell somatic patch-clamp recordings were established from pyramidal neurons in L2/3 of mouse barrel cortex in current-clamp mode (Multiclamp-700A amplifier, Axon Instruments). Data was sampled at 10 kHz, filtered at 3 kHz, and digitized using an AD converter (Digidata 1322, Axon Instruments). Recordings were visualized and controlled using the pClamp software (Molecular Devices). After establishing the whole-cell configuration, the access resistances (R_a) was measured; it typically ranged from 15 to 25 MOhm. Recordings with R_a > 30 MOhm were discarded. The bridge potential was compensated for and the liquid-junction potential was not corrected for. The resting membrane potential (V_m) immediately after

establishing whole-cell access ranged between -85 to -75 mV. De- and hyperpolarizing current pulses were injected to measure input resistance (R_{in}) and membrane time constant (tau_m) from the current-voltage (I-V) traces.

We simultaneously recorded pairs of closely proximate L2/3 pyramidal neurons and tested for synaptic connections by evoking single action potentials alternatingly in the two cells at 0.2 Hz. We identified connections by averaging 20 – 50 sweeps and searching for evoked EPSPs immediately following action potential firing. Once a synaptic connection was identified, we evoked single action potentials in the presynaptic neuron at 0.1 Hz or 0.2 Hz. If necessary, we used a holding current to maintain V_m of the postsynaptic neuron below -70 mV to ensure that EPSPs were dominated by AMPAr currents (Hardingham et al., 2006, 2007, 2010); however, this was rarely needed. Evoked EPSPs were recorded for up to two hours or for as long as the preparation remained stable. To further confirm that evoked EPSPs were AMPAr mediated, the decay phase of averaged EPSP waveforms were fit with single exponentials, which was successful in all experiments. Thus, NMDA currents did not contribute significantly to our EPSPs recorded below -70 mV (Hestrin et al., 1990).

2.2.3   Measurements of EPSP amplitudes

For each EPSP recorded, the peak amplitude was measured offline using a custom-written Matlab package. Briefly, the baseline membrane potential was computed by averaging the membrane voltage in a 1.5 - 2 ms time window before EPSP onset and subtracted from a measurement of the peak EPSP using the same window at the EPSP peak. Window width was chosen so it included the EPSP peak and excluded rise and decay phase. Spacing of baseline and peak windows was chosen so the baseline potential was measured as closely to EPSP onset as possible to minimize noise in the EPSP recording. Typical window spacings ranged from 5 to 6 ms (range: 4.5 – 7). Width and spacing of windows remained constant within experiments. To obtain an independent measure of the baseline potential noise, a separate set of identical windows was used on a portion of the membrane potential preceding the evoked EPSP.

2.2.4   Selection of EPSP data

To allow for reliable measurement of mean EPSP amplitude and to be able to extract quantal parameters, we required extended periods of stable EPSP recordings. Thus, we imposed stability criteria on our data and analyzed only a single epoch of EPSP recording that remained stable for at least 100 consecutive sweeps (see Fig. 15 A). Stable epochs were defined as those in which mean and standard deviation of evoked EPSPs, as measured in blocks of 25 sweeps, remained close to their values in a reference block. The mean was required to remain within 3x the standard error of the mean and the standard deviation was not allowed to change by more than 30% (Hardingham et al., 2006, 2007, 2010). Wherever possible, we sought to analyze the earliest epochs of recording. Therefore, when using the initial block of recording as reference block yielded a stable epoch of at least 100 consecutive sweeps, this stable epoch was used for further analysis. Otherwise, we iteratively assigned the remaining blocks as reference blocks and computed the stable epoch for each of them. The maximum stable epoch was then chosen for further analysis.

2.2.5   Measurements of EPSP kinetics

50 – 100 sweeps of stable epochs of recordings, in which EPSPs were evoked, were aligned to the presynaptic action potential peak, their baseline potential subtracted, and averaged. Measurements were performed on the averaged traces in Stimfit (Guzman et al., 2014). EPSP rise-time was calculated as the interval between 20% and 80% of EPSP peak amplitude.

2.2.6   Histology

Immediately following recordings, slices were fixed overnight in 4% paraformaldehyde (PFA), 0.5% glutaraldehyde, and 15% picric acid in 0.1 M phosphate buffer (PB), pH 7.4. Slices were then washed in PB, incubated in an increasing sucrose ladder for cryoprotection, and rapidly frozen in liquid nitrogen. To quench endogenous peroxidases, sections were incubated in 10% methanol, 3% hydrogen peroxide (H_2O_2) in phosphate buffered saline (PBS). After washing, sections were reacted with the Vectastain ABC Kit (Vector Laboratories, catalog # PK-6100, RRID:AB_2336819) overnight at 4 °C. After washing, biocytin was visualized with a protocol containing nickel-diaminobenzidine (Ni-DAB) tetrahydrochloride and H_2O_2 treatment. The reaction was terminated with a series of washes in PB.

2.2.7   Re-slicing and embedding

To allow for complete reconstructions of recorded neurons in LM, sections were re-sliced to 80 μm. Briefly, sections containing completely filled neurons, as assessed by LM after the Ni-DAB reaction, were carefully glued flat onto and block of agar using UHU superglue gel (UHU GmbH & Co. KG) so that the slice surface that was recorded from pointed upwards. Slices were immediately embedded with warm agar, which was allowed to solidify at 4 °C. Then, the block was trimmed and placed under a vibratome in PB. The embedding agar provided the necessary stability to carefully re-slice sections to 80 μm and completely prevented tissue loss in the process. Thin sections were carefully collected in PB and treated in 1% osmium tetroxide in PB for 10 – 20 min, depending on section thickness and the speed of the reaction. Sections were dehydrated using an ascending series of ethanol and propylene oxide (including treatment in 1% uranyl-acetate in 70% ethanol), and flat-mounted in Durcupan resin (Sigma-Aldrich).

2.2.8   LM reconstructions

3D morphologies of pre- and postsynaptic neuron were completely reconstructed in the Neurolucida Software package (MicroBrighField) under an Olympus BX 51 light microscope equipped with a 60x and 100x oil objective. Shrinkage in the z-dimension was corrected for (factor of 1.3, unpublished observations), no shrinkage was observed in the x-y-plane. Neuron pairs were included only when the entire axon of the presynaptic neuron and all dendrites of the postsynaptic neuron were completely filled and could be fully reconstructed. To assess completeness of filling, we examined whether biocytin-staining of neurites faded out within sections. If this was the case, experiments were discarded. Only experiments, in which all neurites terminated as low or high endings at the surfaces of the original 300 μm section, or ended in well-labeled terminals, were used in the study. It was critical to recover all anatomical synapses and thus we identified and marked all appositions between presynaptic

axon and postsynaptic dendrite in LM. The morphological criteria for determining a contact were the existence of an axonal bouton and no discernable gap between axon and postsynaptic dendrite or spine. Axons crossing within 8 µm above or below a postsynaptic dendrite and formed a bouton close to the crossing point were also marked as contacts and subjected to EM. They could in principle – and in fact in two cases did – consist of a dendritic spine extending in the z-direction towards the axon, which remained disguised by the axon and dendrite below and above the spine (see *Discussion*, Fig. 25). In the rare cases when a contact point was obscured because the postsynaptic dendrite had leaked biocytin into the tissue, we completely reconstructed the respective contact in the EM, which allowed us to verify the existence of synapses unambiguously in all cases.

2.2.9   *Correlated LM-EM*

To relate successfully structure and function, it was crucial to recover all anatomical synapses of connections we had recorded from for all experiments. Therefore, we fully reconstructed presynaptic axon and postsynaptic dendrite in LM and marked all axodendritic contact points as LM appositions (Fig. 10 A-D; Fig. 13 A, B).

Tissue blocks containing appositions were serially sectioned at 60 nm and collected on pioloform-coated single-slot copper grids. Low-magnification electron micrographs were taken and correlated with LM overview images of the same region taken before ultrathin sectioning using the TrakEM2 plugin of ImageJ. By comparing blood vessel patterns and labeled neurites across the neuropil, we were able to recover all axodendritic appositions in EM (Fig. 10 D-F). To verify whether LM appositions were synapses, serial electron micrographs (13,500x) were generated for all appositions and loaded into TrakEM2 for reconstruction. When synapses were found, series of high-magnification images (46,000x) were acquired for all sections that contained the synapse to generate high-magnification reconstructions. We have not corrected for shrinkage through the histology procedures in any of our quantitative EM measurements reported in the *Results*. We have measured shrinkage throughout all stages of processing in both cat (da Costa and Martin, 2009) and mouse cortex (unpublished observations). Aldehyde fixation–perfusion produced a consistent 11% shrinkage.
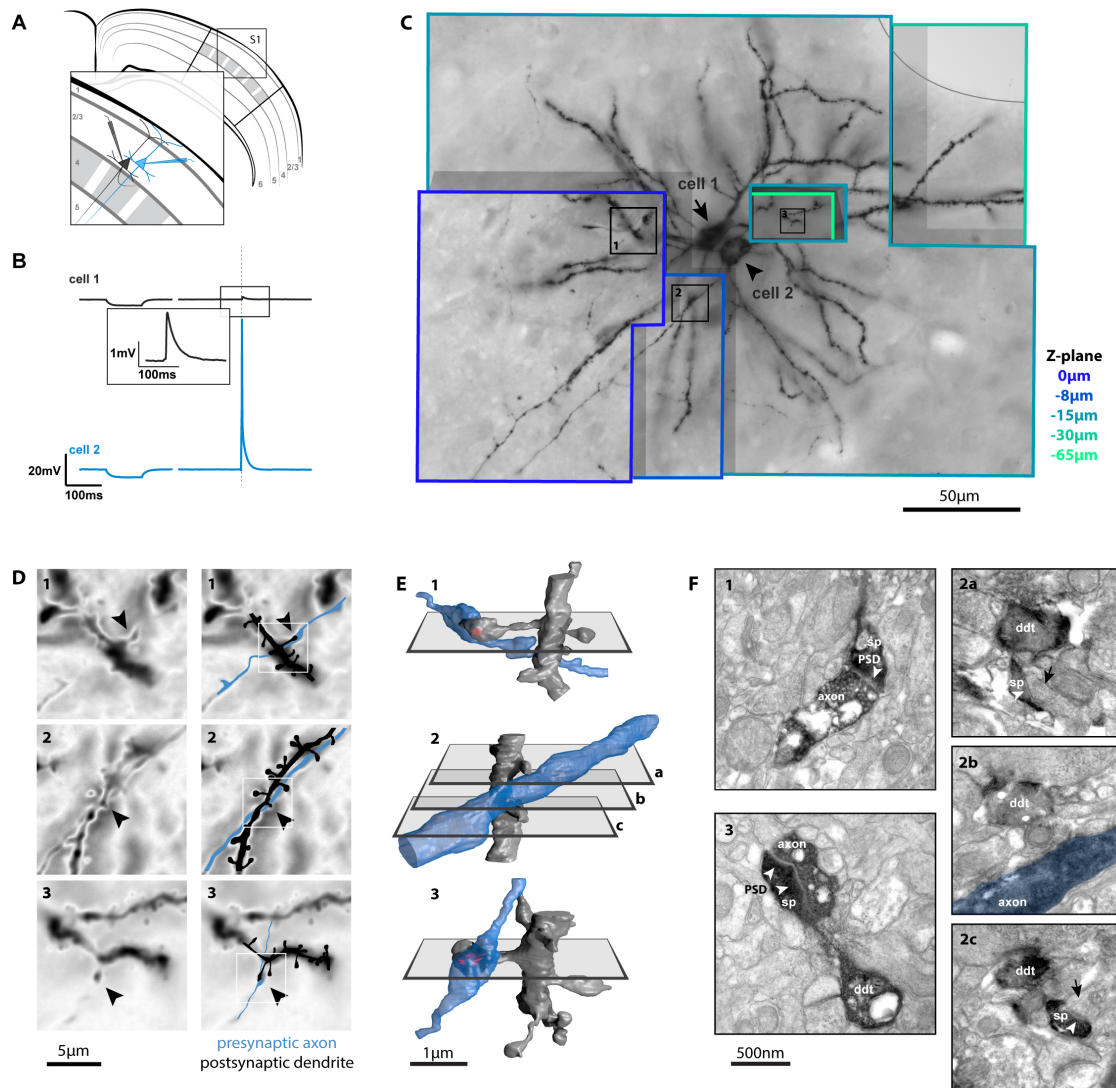
Figure 10. Experimental procedures: recording synaptic transmission between L2/3 pyramidal neurons combined with correlated LM-EM of all axodendritic appositions. A Schematic of *in vitro* dual whole-cell patch-clamp recordings of L2/3 pyramidal neurons in barrel cortex. **B** Single action potentials were evoked at 0.5 Hz to probe connectivity and record evoked EPSPs. Inset, evoked EPSP; dashed line, time-locked to action potential peak. Traces are averages of 100 sweeps. **C** 3D LM stack (60x) of biocytin-reacted neurons following paired recording (traces in B were recorded from this pair). Several z-planes are depicted to visualize the three identified LM appositions (numbered boxes, magnified in D) between presynaptic axon (cell 2) and postsynaptic dendrite (cell 1). Z coordinates are color-coded and normalized to topmost section; grey line, cortical surface. **D** Left, high-magnification LM images of the three axodendritic appositions; numbering corresponds to C. Right, overlays of manual drawings of contact points made from LM stacks and EM reconstructions (not shown). White boxes indicate the positions of the EM reconstructions in E. Arrowheads, locations of potential synapses. **E** 3D EM reconstructions of the three LM appositions. In EM, appositions 1 and 3 were found to be anatomical synapses between presynaptic neuron and postsynaptic dendrite. Planes indicate positions of electron micrographs shown in F. Red, PSD. *(Figure legend continues ->)*

2.2.10 Synapse identification and reconstruction in EM

To relate the electrophysiological properties of synaptic transmission of a connection to the anatomical features of its synapses, we reconstructed the PSD areas of all synapses from series of high-magnification micrographs. Synapses between biocytin-filled presynaptic axon and postsynaptic dendrite were identified from series of high-magnification electron micrographs as follows: they were required to possess a vesicle-filled presynaptic bouton, form an axodendritic contact separated by a synaptic cleft over multiple consecutive sections, and contain a PSD in the dendrite. Identification of synaptic vesicles and synaptic cleft was largely unaffected by biocytin staining. Identifying PSDs in biocytin-filled dendrites after patch-clamp recordings is notoriously difficult (Markram et al., 1997; Silver et al., 2003) and it has not been attempted to measure PSD areas in such tissue. To ensure that we could reliably reconstruct and measure the PSD area, we implemented four additional procedures. First, we tilted electron micrographs containing synapses along the dimension of the synaptic cleft at six angles (-45 °, -30 °, -15 °, +15 °, +30 °, +45 °). This allowed us to obtain an optimal perpendicular imaging plane through the synaptic cleft for all sections (Fig. 11 C; Fig. 13 D; Fig. 14 A). Second, colors of micrographs were inverted, which highlighted subtle contrast differences and aided the identification of the PSD. Third, each synapse was reconstructed by two experts independently and in a blinded manner with respect to the physiological features of synaptic transmission. Finally, a consensus reconstruction was found between the two independent reconstructions. Fourth, we exploited the fact that the PSD area is strongly correlated with the volume of its parent spine head (Harris and Stevens, 1989; Schikorski and Stevens, 1999; Arellano et al., 2007; Bopp et al., 2017); therefore, we reconstructed a large number of unlabeled PSDs and their dendritic spine heads (n = 75) from the adjacent neuropil to acquire a "ground-truth" dataset of the relationship between PSD area and spine head volume in L2/3 of mouse S1. To verify that we had reliably recovered PSD areas of labeled synapses, we measured the volume of the corresponding filled spine heads and compared the PSD-spine head relationships for unlabeled, naïve synapses to the biocytin-filled synapses. 3D reconstructions of representative structures were exported into the Blender software, fitted with a skin, and rendered to offer a 3D impression.

(<- Figure legend continued)
F Single electron micrographs of the three appositions. At appositions 1 and 3, the presynaptic axon formed an anatomical synapse on a dendritic spine (sp) that emerged from the labeled postsynaptic dendrite (ddt). Synaptic specializations (presynaptic vesicles, synaptic cleft, PSD) could be distinguished despite biocytin-reaction-product. Arrowheads, PSD. At apposition 2, two spines (micrographs 2a, 2c) emerged from the postsynaptic dendrite and formed synapses (arrowheads) with unlabeled boutons (arrows). The presynaptic axon (blue) remained separated from the postsynaptic dendrite at the point of closest proximity (micrograph 2b). Same color-scheme throughout figure.
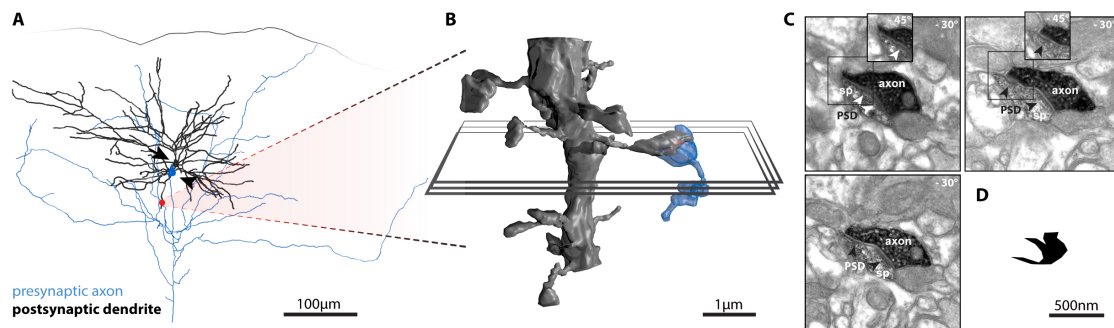
Figure 11. Experimental procedures: correlated LM-EM and tilt series of cross-sections containing synapses. (Different experiment than shown in figure 10.) **A** Full 3D LM reconstruction of presynaptic axon (blue) and postsynaptic dendrite (black) of a biocytin-stained pair that was synaptically connected. A single axodendritic apposition was identified between the cells in LM (red dot). Presynaptic dendrite and postsynaptic axon not shown for clarity. Arrowhead, presynaptic soma; arrow, postsynaptic soma; cortical surface indicated. **B** 3D EM reconstruction of the apposition revealed that a synapse was formed between presynaptic axon and postsynaptic dendrite. Same color scheme as in A; red, PSD. Planes indicate the positions of electron micrographs shown in C. **C** Electron micrographs of consecutive cross-sections through the synapse. The dendritic spine (sp) was clearly stained, but the biocytin appeared patchier than in other experiments, which allowed easy identification of the PSD (arrowheads). Micrographs were acquired at a tilted angle along the axis of the synaptic cleft for a clear view on the PSD (the tilt angle is indicated). Insets show additional tilts that were acquired for the regions surrounded by boxes. **D** *En-face* representation (2D-projection) of the reconstructed PSD.

2.2.11 Compartmental NEURON model

We chose a L2/3 neuron, whose total dendrite length, longest dendrite, input resistance, and membrane time constant best reflected the mean of all postsynaptic neurons in the study. A compartmental model was generated in the NEURON software package from a volumetric reconstruction of the cell's dendritic tree using the d-lambda rule. The experimentally recorded waveforms to two hyperpolarizing and one depolarizing current step (-40 pA, -80 pA, +40 pA) were used to fit the specific membrane resistance (R_m = 5245.2 Ohm cm^2), specific membrane capacitance (C_m = 4.26 µF/cm^2), and specific axial resistance (R_a = 114.3 Ohm cm) of the model. The high values for R_m and C_m reflect that spines were not modeled specifically (Schoonover et al., 2014). V_m was set to the experimentally observed -82.6 mV. Alpha synaptic conductances (g_{max} = 0.005 µS, t_{max} = 0.5 ms) were simulated at 810 different locations of the dendritic tree. The dendro-somatic attenuation factor (**a**) was calculated by dividing the evoked peak EPSP amplitude at the location of the synapse in the dendrite (ΔV) with the somatic peak EPSP amplitude ($\Delta V'$) and plotted as a function of the synaptic distance to soma. A single exponential was fit to the data. To quantify uncertainty associated with attenuation, dendritic distances were binned (into 10 µm windows or larger windows, which included at least 20 entries) and 2.5 and 97.5 percentiles of the attenuation factors calculated for each bin (Fig. 17 D).

2.2.12 Approximation of peak dendritic EPSP amplitudes

When a single synapse was found for a connection, ΔV was approximated by multiplying the experimentally recorded somatic EPSP amplitude with the attenuation factor **a** as derived from the exponential fit for the respective distance of the synapse to the soma that was measured from LM reconstructions for that connection. 95% confidence intervals (CIs) were constructed for the data point by using the 2.5 and 97.5 percentiles of **a** in the respective distance bin.

When a connection contained two synapses, we had to include two additional assumptions to be able to estimate ΔV for each PSD individually (ΔV_A and ΔV_B) (Fig. 12). Motivated by our finding that EPSP amplitude correlated with cPSD area (see *Results*), we assumed that in connections consisting of two synapses, the ratio **R** of the PSD areas (PSD_A to PSD_B) is reflected in the ratio of the local dendritic EPSPs (ΔV_A to ΔV_B) they evoke. Note that while this assumption constrains the ratio of ΔV_A to ΔV_B within an experiment, importantly, it does not bias the comparison of absolute ΔV_A and ΔV_B amplitudes between the experiments. The absolute amplitudes are computed as a function of somatic EPSP and the respective synaptic distances. Also, it does not imply that the two attenuated EPSPs at the soma ($\Delta V_A'$ and $\Delta V_B'$) follow the same ratio. Because of the different dendrite lengths of the synapses to the soma, they will be attenuated by different factors (a_A and a_B). Finally, we assumed that the two attenuated EPSPs ($\Delta V_A'$ and $\Delta V_B'$) summed linearly at the soma to generate the somatic EPSP amplitude ($\Delta V'$) (Koch, 2004). Using these assumptions, the respective ΔV was calculated for each of the two synapses (A, B) given $\Delta V'$, the distance of each synapse to soma (expressed as the attenuation factors a_A and a_B), and **R**, as follows:

$$\Delta V_A = \frac{R \, \Delta V'}{\frac{1}{a_B} + \frac{R}{a_A}} \tag{1}$$

$$\Delta V_B = -\frac{\Delta V'}{\frac{1}{a_B} + \frac{R}{a_A}} \tag{2}$$

As above, 95% CIs were constructed for ΔV_A and ΔV_B by using the values for the 2.5 and 97.5 percentile of **a** in the respective distance bins.
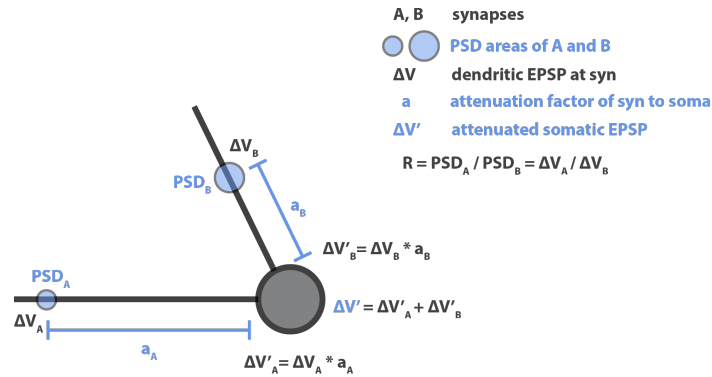
Figure 12. Assumptions for approximating the respective dendritic EPSP amplitudes when two synapses contributed to the somatic EPSP. In several experiments, two synapses with different PSD areas and at different dendritic distances to the soma contributed to the somatic EPSP ($\Delta V'$). We used our experimental data and the equations and assumptions shown to approximate the local dendritic peak EPSP (ΔV_A and ΔV_B) generated by each individual PSD (PSD_A and PSD_B) at its respective location in the dendrite. See text for details. Blue font, experimentally measured parameters; black font, model assumptions.

2.2.13 Statistical Moments Analysis of Quanta (SMAQ)

Under the assumption that quantal transmission can be approximated with a simple binomial model, mean (μ), standard deviation (σ), and skewness (γ) of the experimentally recorded EPSP distribution can be expressed as functions of the quantal parameters N, P, Q (Larkman et al., 1992, 1997; Hannay et al., 1993; Taschenberger et al., 2005):

$$\mu = N * P * Q \quad , [mV] \tag{3}$$

$$\sigma = \sqrt{N * P * (1 - P)} * Q \quad , [mV] \tag{4}$$

$$\gamma = \frac{1 - 2P}{\sqrt{N * P * (1 - P)}} \quad , [\,] \tag{5}$$

These equations were reshaped to derive unique analytical solutions for N, P, and Q, as functions of μ, σ, and γ:

$$N = - \frac{\gamma^2}{(\gamma * \mu - \sigma) * \sigma} \quad , [\,] \tag{6}$$

$$P = \frac{\gamma * \mu - \sigma}{\gamma * \mu - 2\sigma} \quad , [\,] \tag{7}$$

$$Q = \frac{-\gamma * \mu * \sigma + 2\sigma^2}{\gamma} \quad , [mV] \tag{8}$$

For each connection, μ, σ, and γ of the stable epoch of recording were computed, and the corresponding N, P, Q calculated. We termed this method *Statistical Moments Analysis of Quanta (SMAQ)*. Inspired by Bayesian logic, we then derived 95% CIs for the quantal parameters by asking: which underlying binomial models (combinations of N, P, Q) could have given rise to EPSP distributions that would have provided the same SMAQ solutions? We simulated all possible permutations of a large range of quantal parameters (N between 1 and 20, P between 0.1 and 0.9, Q between 0.1 mV and 1.5 mV, n = 2700). For each experiment, we generated tailored confidence intervals individually: we generated 10,000 realizations of EPSP distributions for each one of the 2700 binomial models that contained the same number of entries as the experimentally observed histogram. Additionally, we added the experimentally observed noise onto the quanta released by the model as a randomly drawn realization from a Gaussian with a mean of zero and the same standard deviation as the recording noise. We then used SMAQ to calculate N, P, and Q for each one of the $27 * 10^6$ simulated EPSP distributions and asked: which underlying binomial models could have produced the experimentally observed N, P, and Q at the 95% certainty level? For example, we generated the distribution of the Ns underlying all binomial models that had ever produced the same SMAQ solution for N as the experimental histogram. The 2.5 and 97.5 percentiles of that distribution gave the 95% CI of the experimentally observed N and indicated which underlying Ns, with 95% certainty, could have also produced the experimentally observed EPSP distribution.

In addition, we computed 95% CIs using the same bootstrap resampling algorithm, which is used to create CIs for quantal parameters derived by fitting binomial models to peaky histograms (see below). This allowed us to compare the uncertainties associated with the solutions of the two methods.

2.2.14 Fitting binomial models to peaky histograms

Amplitude histograms of stable EPSP recordings that revealed equally-spaced peaks were fit with a quantal binomial model as explained in Hardingham et al. (2006, 2007, 2010). We used the MATLAB implementation of the method available on *www.jennyreadresearch.com*. The model was constrained to search for a best-fit for N in the range between 1 and 20. Noise was not constrained to allow for negative quantal variance (Jack et al., 1990), which was observed in one experiment, and is otherwise not implemented in the method. To enable a fair comparison with SMAQ, conductance probability was set to 1 and offset was disabled unless no successful fit could be found. Only in one case, an offset of -0.053 mV had to be implemented. All seven available adequacy-of-fit tests were used, which include the Kolmogorov–Smirnov D statistic, the sum of squared differences between model and data cumulative distributions, and chi-squared statistics for five different bin sizes. A fit was considered successful only when it passed all tests. We used the inbuilt bootstrap-resampling function to calculate 95% CIs for the best-fit parameters. Briefly, new distributions were generated by drawing with replacement from the experimental EPSP histogram. A small amount of jitter was added to each selected EPSP and the resampled EPSP distributions were fit and tested for adequacy in the same manner as the experimental distribution. The procedure was repeated until 100 successful resampled fits had been generated. 95% CIs were constructed for N, P, and Q from the 100 estimates of N, P, and Q of the resampled distributions.

2.3   Results

We recorded from 59 synapses between L2/3 pyramidal neurons across 61 animals. Of these, 10 connections passed our electrophysiological and anatomical quality standards and were included in the final dataset. This required that we recorded ≥ 100 consecutive stable sweeps (mean ± standard deviation: 225 ± 80), that presynaptic axon and postsynaptic dendrite were completely filled with biocytin, and that synaptic features could be clearly identified in the EM. Unitary EPSP amplitudes during stable epochs of recording across the 10 connections ranged from 0.15 mV to 2.25 mV (mean ± standard deviation: 1.05 ± 0.70 mV) with a coefficient of variation of 0.39 ± 0.25.

2.3.1   The majority of LM appositions are not synapses between labeled structures in the EM

We found a total of 40 axodendritic appositions between the 10 connected pairs in LM (range: 1 to 7, mean ± standard deviation: 4.0 ± 1.9). EM revealed that 16 appositions were anatomical synapses (mean: 1.6). Of the 10 pairs, 6 pairs were connected by 2 synapses, and 4 by only a single synapse (Fig. 16). Identification of synaptic vesicles and synaptic cleft was largely unaffected by biocytin staining and vesicle lumen and cleft interior could be clearly distinguished. The PSD usually appeared as a negative staining against the biocytin in the postsynaptic dendrite and its existence could be clearly identified in all cases (Figs. 10 F; 11 C; 13 D, G; 14 A). In the 24 cases when appositions did not form anatomical synapses between presynaptic axon and postsynaptic dendrite, the labeled axonal bouton usually formed a synapse with an unlabeled dendritic spine in the neuropil and the labeled dendritic spine formed a synapse with an unlabeled axonal bouton (Fig. 10 D - F; Fig. 13 B - J). Presynaptic axon and postsynaptic dendrite usually remained separated by a gap that could be as small as a few nanometers (Fig. 10 F; Fig 13 G - J). Importantly, we were unable to predict from LM alone whether a LM apposition formed an anatomical synapse.

2.3.2   PSD area can be measured reliably despite of biocytin reaction-product in the spine

PSD area and spine head volume of the biocytin-filled synapses were strongly correlated (n = 15, one synapse on dendritic shaft, excluded). Significantly, the same correlation was found in a "ground-truth" dataset consisting of unlabeled dendritic spine heads and their PSDs (n = 75), which we acquired from the adjacent neuropil (Fig. 14 D). There was no significant difference between correlation coefficients of unlabeled and labeled synapses (p = 0.34, Fisher r-z transformation). All synapses reconstructed in the neuropil and the labeled synapses were asymmetric (Gray's type 1) (Gray, 1959; Colonnier, 1968). PSD areas of the 16 labeled synapses (mean ± standard deviation: 0.071 ± 0.044 μm^2) were significantly larger (p = 0.019, non-parametric Mann-Whitney (M-W) test) compared to PSD areas of unlabeled synapses in the neuropil (mean ± standard deviation: 0.045 ± 0.036 μm^2).
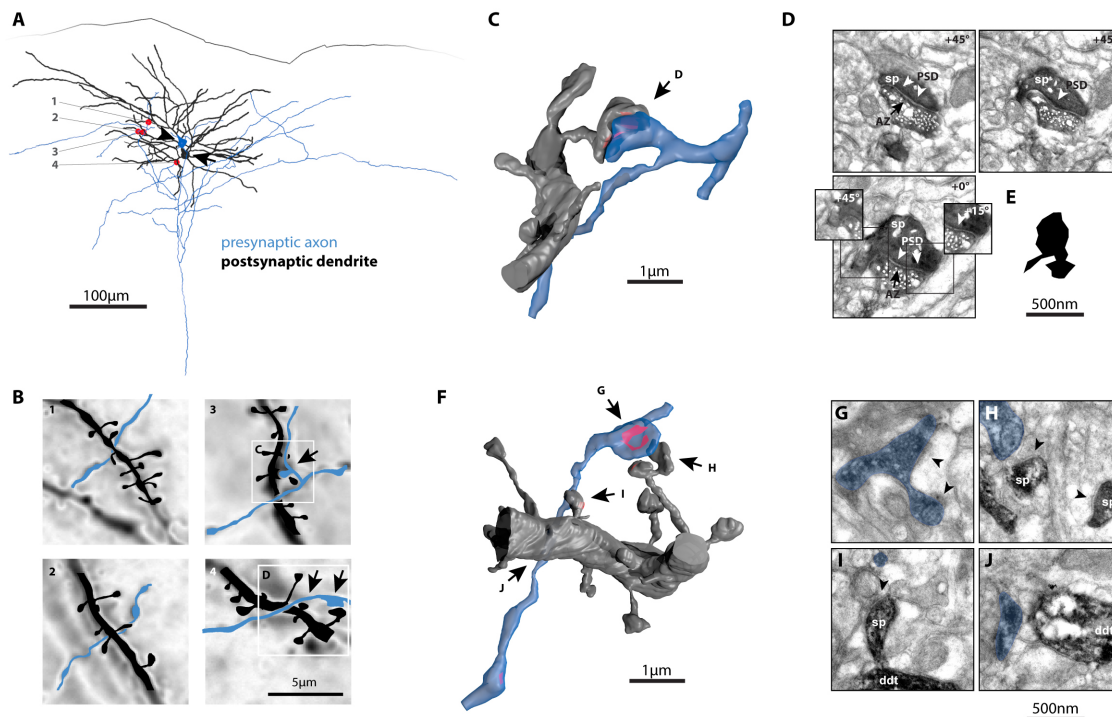
Figure 13. At the majority of LM appositions, no synapses were formed between the labeled pyramidal neurons. (Different experiment than shown in figures 10 and 11.) **A** Full 3D LM reconstruction of presynaptic axon (blue) and postsynaptic dendrite (black) of a biocytin-stained pair of synaptically connected pyramidal neurons. In LM, four appositions (red dots, numbered) were identified. Arrowhead, presynaptic soma; arrow, postsynaptic soma; presynaptic dendrite and postsynaptic axon excluded for clarity. **B** High-magnification LM images of the appositions overlaid with manual drawings of the contact points between presynaptic axon and postsynaptic dendrite. Numbering corresponds to A. Arrows, locations of potential synapses shown in C, F. White boxes indicate positions of EM reconstructions shown in C, F. At appositions 1 and 2, presynaptic axon and postsynaptic dendrite traversed with distances of 2-4 µm, and EM revealed that no synapses were formed (not shown). **C** 3D EM reconstruction of apposition 3 revealed that a synapse was formed between the presynaptic axon and a spine emerging from the postsynaptic dendrite. Arrow indicates position of micrographs shown in D. Red, PSD. **D** Electron micrographs of consecutive cross-sections through the synapse in C. The presynaptic bouton contains synaptic vesicles, the active zone (AZ) is visible as a positive staining against the biocytin reaction-product. Likewise, the PSD (arrowheads) appears as a dark staining against reaction-product in the postsynaptic spine (sp). Tilt angles, at which micrographs were acquired, are indicated at top right. Insets in third micrograph contain two additional tilts of regions indicated by boxes. **E** E*n-face* representation (2D projection) of the reconstructed PSD. **F** 3D EM reconstruction of apposition 4. Despite three potential synaptic locations (arrows G, I, J), the presynaptic axon did not form a synapse with the postsynaptic dendrite. Arrowheads indicate positions of micrographs shown in G – J. Red, PSDs formed with unlabeled elements of the neuropil. **G – J** Electron micrographs of locations indicated by arrows in F. Blue, presynaptic axon; arrowheads, synaptic specializations; sp, dendritc spine; ddt, dendritic shaft. **G** The prominent presynaptic bouton forms a synapse with an unlabeled dendritic spine. **H** Postsynaptic dendritic spines form synapses with unlabeled boutons and not the labeled bouton. **I** Postsynaptic spine forms synapse with unlabeled bouton. The labeled presynaptic axon traverses the section. **J** Presynaptic axon traverses in close proximity to postsynaptic dendrite without forming a bouton. No physical contact exists.
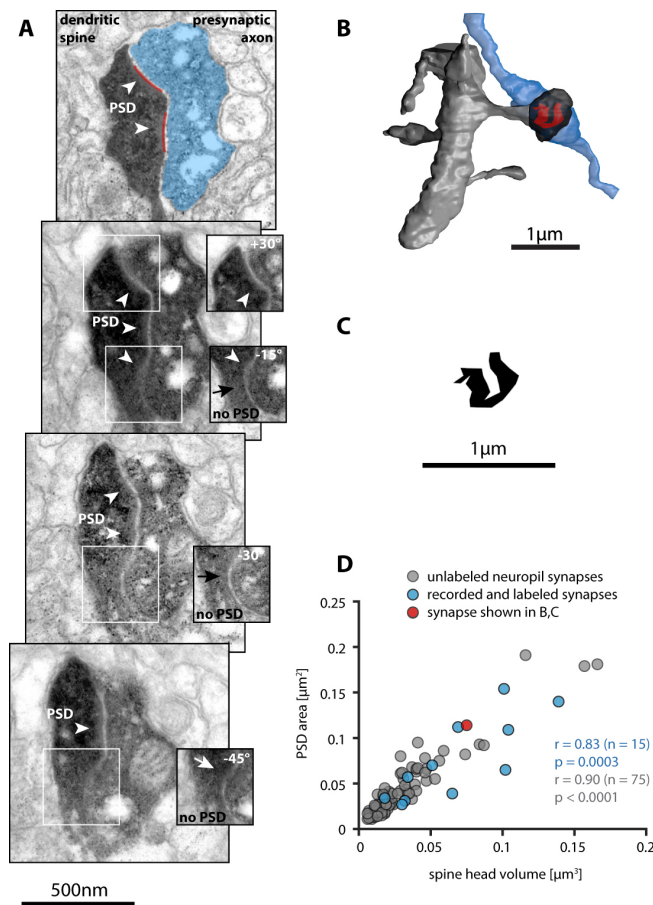
Figure 14. The PSD area can be reconstructed and measured reliably despite of biocytin reaction-product in dendritic spine and presynaptic bouton. A Series of electron micrographs showing 4 consecutive cross-sections through a synapse, acquired without a tilt angle. Same synapse as shown in figure 10 E (bottom). First section: blue, presynaptic axon; black, postsynaptic dendrite; red, PSD. White boxes indicate regions in which the imaging plane was not perpendicular to the synaptic cleft and the identification of the PSD was hindered. Insets show micrographs of these regions acquired at a tilted angle in the EM (angle indicated). In this experiment, the PSD appeared as a negative staining against the reaction-product. Arrowheads, PSD; arrows, locations where no PSD was identified. **B** 3D EM reconstruction of the entire synapse and a portion of the presynaptic axon and postsynaptic dendrite. Blue, presynaptic axon; grey, postsynaptic dendrite and spine neck; black, postsynaptic spine head; red, PSD. Same reconstruction as in figure 10 E (bottom), rotated by 180°. **C** *En-face* representation (2D projection) of the reconstructed PSD reveals a "horseshoe-like" morphology. **D** Scatter plot showing the correlation found between postsynaptic spine head volume and PSD area for biocytin-filled synapses (blue, red) and unlabeled, naive synapses that were reconstructed from the adjacent neuropil (grey). Red, synapse shown in this figure; r = non-parametric Spearman correlation coefficient. One biocytin-filled synapse excluded because it was formed on a dendritic shaft.

2.3.3   Synapse size predicts EPSP amplitude

We first asked how anatomical synapse size relates to the strength of synaptic transmission. Because 6 of 10 connections consisted of 2 anatomical synapses, we computed the cPSD of a connection to make our anatomy comparable to the electrophysiology. CPSD represents the total PSD area made by a connection. Importantly, we found it to be significantly correlated with the mean EPSP amplitude of the stable epoch of recording (Fig. 15 E). For subsequent quantal analysis, it was crucial to measure extended stable epochs of recording, which prevented us from including the initial phase of recording in some experiments (Fig. 15 A). In 5 out of 10 experiments, the initial block (containing the first 25 sweeps) could be included in the stable epoch and in all experiments, mean amplitude of the selected stable epoch did not fluctuate by more than 30% from the mean amplitude of the initial block. However, to exclude the possibility that different degrees of dialysis with pipette intracellular solution and resulting washout of the cytosol between experiments had compromised our dataset (Hardingham et al., 2010), we additionally measured the mean EPSP amplitude only from the initial block of 25 sweeps. Reassuringly, when we plotted this initial mean EPSP amplitude against the cPSD area, the same correlation efficient (r = 0.73) emerged (p = 0.02, not shown).
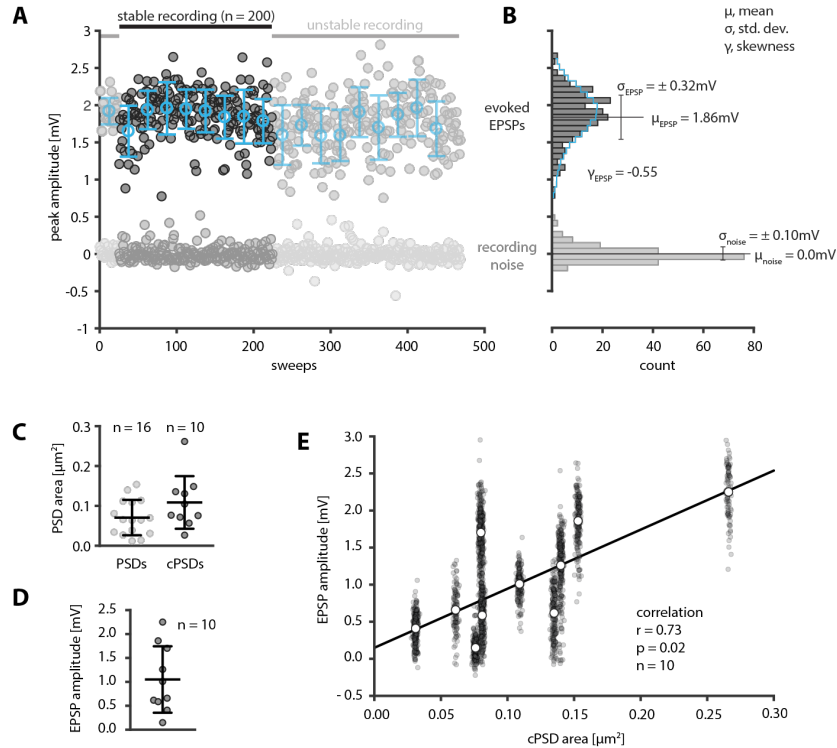
Figure 15. Cumulative PSD area correlates with somatic EPSP amplitude. A, B Evoked EPSP recording of the connection shown in figures 10, 14. **A** Evoked EPSP amplitudes (dark grey) and recording noise (light grey) over the course of the experiment. Blue bars indicate mean and standard deviation of EPSP amplitudes in bins of 25 sweeps. EPSPs that failed to meet our stability criteria (faded out) were not used for further analyses. **B** Histogram of EPSP amplitude (dark grey) and recording noise (light grey) during the stable period of recording (n = 200 sweeps). Values for mean, standard deviation, and skewness of the EPSP distribution are indicated. A 7-point moving average (blue) overlaid over the EPSP distribution highlights its left-skew. Tick marks on ordinate correspond to tick marks in A. **C** Distribution of PSD areas found between the 10 connected pairs in the study. Left, PSD areas of all 16 synapses between the 10 pairs. Right, for pairs that were connected by multiple synapses (n = 6), PSD areas were summed into a cumulative PSD area (cPSD). **D** Distribution of stable mean EPSP amplitudes recorded for the 10 connected pairs. **E** Scatter plot showing relationship of mean EPSP amplitude and cPSD area of the 10 connections (white dots). Transparent grey point clouds show all EPSP amplitudes of stable epochs of recording across all experiments (r = non-parametric Spearman correlation coefficient). The mean EPSP amplitudes could be well fit with a line using linear regression (slope = 7.97 ± 2.44).

2.3.4 Compartmental model to exclude differential dendritic attenuation of EPSP amplitudes

The 16 synapses were located at a mean dendritic distance to soma of 89 ± 45 µm (range: 33 µm to 235 µm) (Fig. 16 A, Fig. 17 A). Such a large variance of synaptic distances to the soma suggested that the somatic EPSPs we recorded could likely suffer from different degrees of attenuation across experiments. Furthermore, 6 connections formed two synapses and, in these cases, the two synapses were likewise located at different distances to the soma with respect to each other. Therefore, also the EPSPs that these two synapses evoked at the synaptic sites in the dendrites were subject to different amounts of attenuation to the soma, respectively.

In search of a footprint for attenuation, we found that EPSP rise-times were positively correlated with the average synapse-to-soma distance (Fig. 17 B), which suggested that our somatically-recorded EPSPs were indeed subject to significant attenuated as a function of the distance of the synapse to the soma.

To disentangle the effects of dendritic attenuation from our somatically recorded EPSPs, we estimated the local peak EPSP amplitude in the dendrite at the synaptic location for each of the 16 synapses.

We constructed a compartmental model from a volumetric reconstruction of a L2/3 pyramidal neuron (Fig. 17 C). We chose a pyramidal cell, whose anatomical and electrophysiological properties best represented the mean values of all postsynaptic neurons in the study (mean ± standard deviation of population in brackets). This pyramidal cell had a total dendrite length of 5285 µm (4611 ± 1440 µm), longest dendrite of 842 µm (857 ± 238 µm), an input resistance of 72.9 MOhm (67 ± 12 MOhm), and a membrane time constant of 11.8 ms (14.8 ± 3.9 ms). After tuning the model, its input resistance (R_{in} = 72.7 MOhm) matched the experimental R_{in} (72.9 MOhm). We then simulated synaptic conductances at 810 different locations on the dendritic tree (Fig. 17 C) and computed the attenuation factor as a function of dendritic distance, which could be fit with a single exponential function (Fig. 17 D). From these data, we then computed the local peak EPSP amplitude (ΔV), and its associated 95% confidence bounds, that was presumably evoked in the dendrite below the spine at the synaptic location. For the 6 connections formed by 2 synapses (marked PSD_A and PSD_B) we had to include two additional assumptions to be able to calculate ΔV for each PSD individually ($ΔV_A$ and $ΔV_B$) (Fig. 17 E), see *Methods* for further details (Fig. 12).

All spine necks were relatively short (mean length of 820 nm (range: 210 nm to 1.46 µm), mean diameter of 130 nm (range: 80 nm to 230 nm), uncorrected for shrinkage) and thus the synaptic current can be regarded as flowing directly into the dendrite and not lost across the spine head membrane (Harris and Stevens, 1989; Koch, 2004); i.e. from known spine dimensions, effectively all the synaptic charge injected into a spine head is transmitted to the parent dendrite. Of the 16 synapses, 15 were formed on dendritic spines and 1 on the dendritic shaft directly (Fig. 16). We found that the ΔV that we computed in this manner was correlated with the PSD areas of the respective synapses (n = 16) (Fig. 17 E). Finally, we sought to exclude that this correlation had emerged simply as a function of increasing the number of observations or because of our assumption that for connections with 2 synapses, $ΔV_A$ and $ΔV_B$ reflect the ratio of PSD_A to PSD_B (see *Methods*). Therefore, we collapsed the dataset back to 10 experiments by computing the average dendritic EPSP amplitude per synapse and the two synapse's average PSD area and plotted them with the 4 pairs that were connected by a single synapse. We found that the same positive correlation emerged significantly (r = 0.67, p = 0.039, n = 10, not shown).
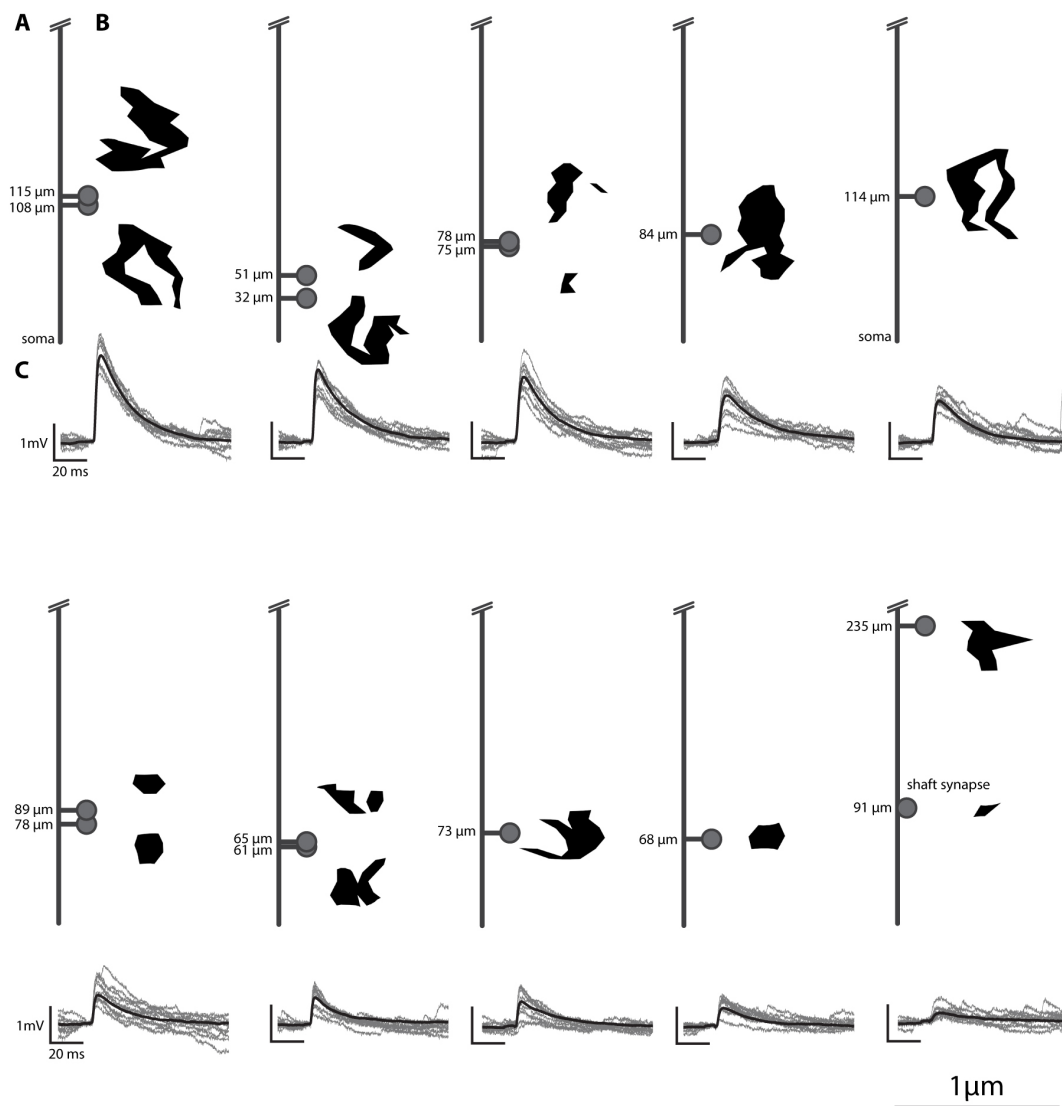
Figure 16. Overview across all 10 experiments showing for each connection the important anatomical properties of the recovered synapses and the corresponding evoked EPSP waveforms. Experiments are sorted by decreasing mean EPSP amplitude. **A** Dendritic distances of the identified synapses to the soma. The collapsed dendritic tree is represented schematically ranging from soma (bottom) to a distance of 250 μm (top, cut off). The dendritic distances at which the respective synapses were found are indicated by the spine locations. No distinction made between apical and basal dendrites. All synapses were made on dendritic spines, except for the proximal synapse in experiment 10, which was made on the dendritic shaft (indicated). **B** Morphologies of the reconstructed PSDs. *En-face* representations of PSDs highlight the ranges of identified sizes and shapes. PSDs are positioned next to spines according to their respective dendritic distances as indicated in A. Corresponding scale bar indicated at bottom right of figure. **C** Waveforms of evoked EPSP recordings. Black, average waveform of EPSP recordings during stable epochs for each connection. Grey, 10 randomly-selected evoked EPSP waveforms taken during stable epochs of recording.
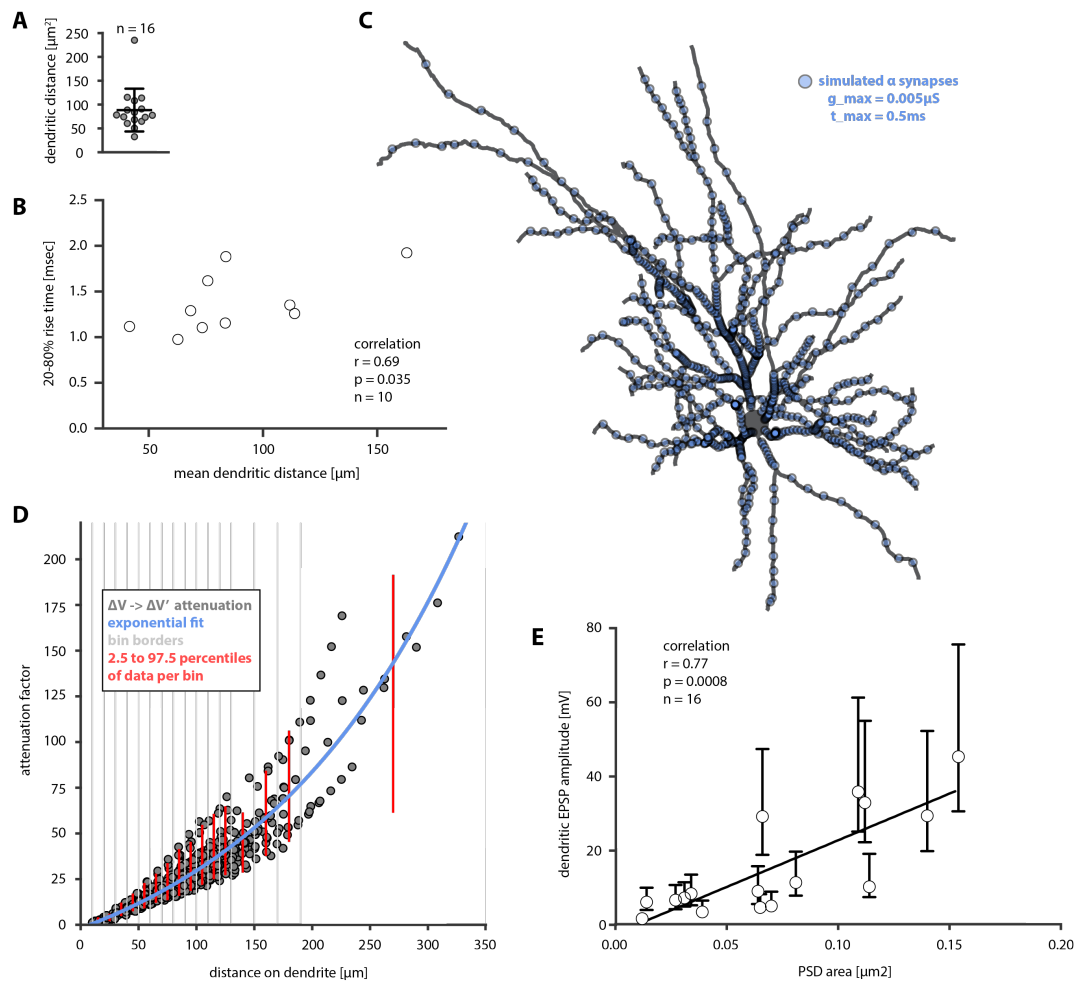
Figure 17. Compartmental model predicts that the EPSP amplitudes at the synaptic locations in the dendrite correlate with PSD area. A Distribution of dendritic distances to the soma for all identified synapses. **B** Scatter plot showing the correlation of EPSP rise-times and mean dendritic distances of the identified synapses to the soma (mean distances were computed for connections with 2 synapses). **C** Compartmental model of L2/3 pyramidal neuron that was recorded from and filled. 810 alpha synapses were simulated along the entire dendritic tree; properties of the alpha synapses are indicated. **D** Scatter plot showing the simulated attenuation of dendritic EPSPs to the soma as a function of synaptic distance to soma. For each of the 810 alpha synapses, the attenuation between peak EPSP amplitude in the dendrite at the synaptic location (ΔV) and the soma (ΔV') was computed. Blue curve, single exponential fit to data; vertical grey lines, distance bins, in which CIs were computed; vertical red lines, 95% CIs connecting the 2.5 and 97.5 percentiles of data points within bins (see *Methods*). **E** Scatter plot showing relationship of PSD area and approximated dendritic EPSP amplitude (ΔV) at the synaptic locations for all 16 synapses found in the study. 95% CIs are indicated (constructed from CIs shown in D). R = non-parametric Spearman correlation coefficient. The dendritic EPSP amplitudes could be well fit with a line using linear regression (slope = 252 ± 50).

2.3.5   Validation of the Statistical Moments Analysis of Quanta

Next, we asked how the anatomical features of cortical synapses relate to the quantal properties of synaptic transmission and in particular, if multiple release sites were contained within a single anatomical synapse. Of the 10 connections that passed our electrophysiological and anatomical quality standards, none displayed EPSP histograms with equally-spaced peaks. Thus, we developed a novel form of quantal analysis, which we termed *SMAQ*, see *Methods*. We additionally constructed 95% CIs for SMAQ using the Bayesian-inspired approach of approximating the distributions of quantal parameters, which could have produced the same solutions as the experimentally observed histogram.

To calibrate SMAQ, we exploited the fact that 5 EPSP histograms revealed equally-spaced peaks (but that had failed our anatomical quality criteria). This allowed us to analyze them both with SMAQ and by fitting binomial models to the histograms (Fig. 18 A - E). The histograms contained on average 130 sweeps (range: $100 - 200$) and none of the solutions provided for N, P, and Q by the method of fitting peaky histograms differed significantly from the solutions provided by SMAQ (mean ± standard deviation: N: 2.4 ± 1.1 and 1.9 ± 1.0; P: 0.44 ± 0.15 and 0.40 ± 0.08; Q: 0.25 ± 0.07 mV and 0.32 ± 0.10 mV, respectively; non-parametric Wilcoxon matched-pairs signed rank test).

We then compared the uncertainty associated with the solutions provided by the two methods: first we constructed 95% CIs from bootstrap resampling for both methods and found that their solutions were associated with significant uncertainty, which depended on the number of entries in the histograms (Fig. 18 F). The uncertainty in predicting N and Q was similar between methods, while the uncertainty in predicting P seemed slightly higher for the method of fitting histograms (not pursued statistically).

When we constructed 95% CIs for SMAQ using our Bayesian-inspired approach, these CIs were larger compared to the CIs for SMAQ constructed from bootstrap resampling (Fig. 18 F).
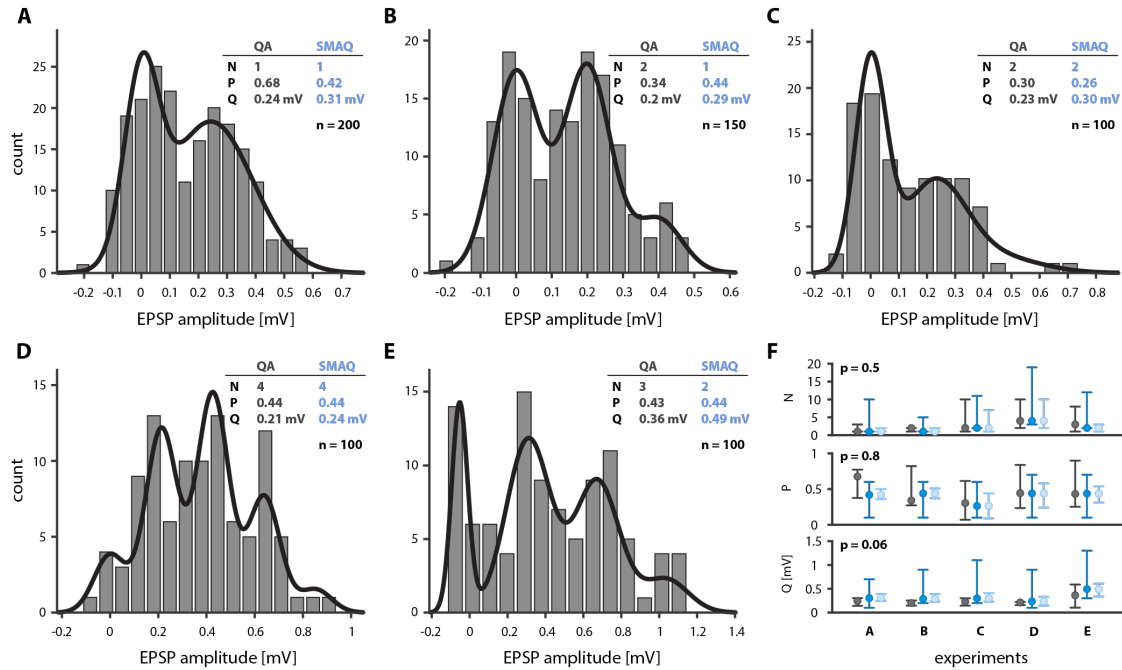
Figure 18. Quantal analysis using SMAQ provides similar results and uncertainty as the method of fitting binomial models to peaky histograms. A – E Five EPSP amplitude histograms contained equally-spaced peaks. They were analyzed using SMAQ and could be fit successfully with a simple quantal binomial model to extract the quantal parameters (black lines overlaid on histograms). Insets show comparisons of the solutions provided by fitting peaky histograms (QA) and SMAQ; n, number of entries per histogram. **F** Comparison of the solutions for the quantal parameters and the associated 95% confidence intervals given by the method of fitting peaky histograms (black) and SMAQ (blue) across the five experiments shown in A-E. Dark blue, Bayesian-inspired CIs for SMAQ; light blue, CIs for SMAQ derived from the same bootstrap resampling algorithm used to derive CIs for the method of fitting peaky histograms (black). Non-parametric Wilcoxon matched-pairs signed rank test to compare solutions provided by the two methods. For all three quantal parameters, the solutions given by the two methods were not significantly different (see text for details).

2.3.6 Single anatomical synapses contain multiple transmitter release sites

We used SMAQ to recover N (mean ± standard deviation: 6.9 ± 4.2), P (0.6 ± 0.2), and Q (0.28 ± 0.15 mV) for the 10 connections used in the study (Fig. 19). In addition, we computed Bayesian-inspired CIs for our prediction of N (mean low bound ± standard deviation: 4.1 ± 1.8; mean high bound ± standard deviation: 17.8 ± 2.5), P (0.4 ± 0.2; 0.8 ± 0.1), and Q (0.11 ± 0.03 mV; 0.7 ± 0.29 mV).

We found that the electrophysiological N exceeded the number of anatomical synapses for all connections (Fig. 19 B). Also, the minimum number of release sites (the lower CI bounds for N) exceeded the number of anatomical synapses in all experiments but one (experiment 9 in Fig. 19 B).

No significant correlation emerged when we plotted N of a connection against the cPSD area (p = 0.71, n = 10, not shown). We also computed the putative number of release sites for each of the 16 anatomical synapses: for connections with 2 synapses, we split N and assigned them to the two individual synapses following their PSD area ratio. When we compared these "putative N per individual synapse" to the PSD areas, there was no significant correlation (p = 0.059, n = 16) (Fig. 19 C).

Likewise, no significant correlation emerged when we compared Q of a connection to the individual PSD areas (p = 0.07, n = 16), assuming uniform Q in case the connection consisted of 2 synapses (Fig. 19 E). However, we found that Q significantly decreased as a function of the distance of the synapses to the soma (r = -0.57, p = 0.02) (Fig. 19 F).

We also found that the PSD areas of the 16 synapses were correlated with P of the connection (r = 0.62, p = 0.012) (Fig. 19 D), which was assumed to be uniform across N within experiments in accordance with a simple binomial model.
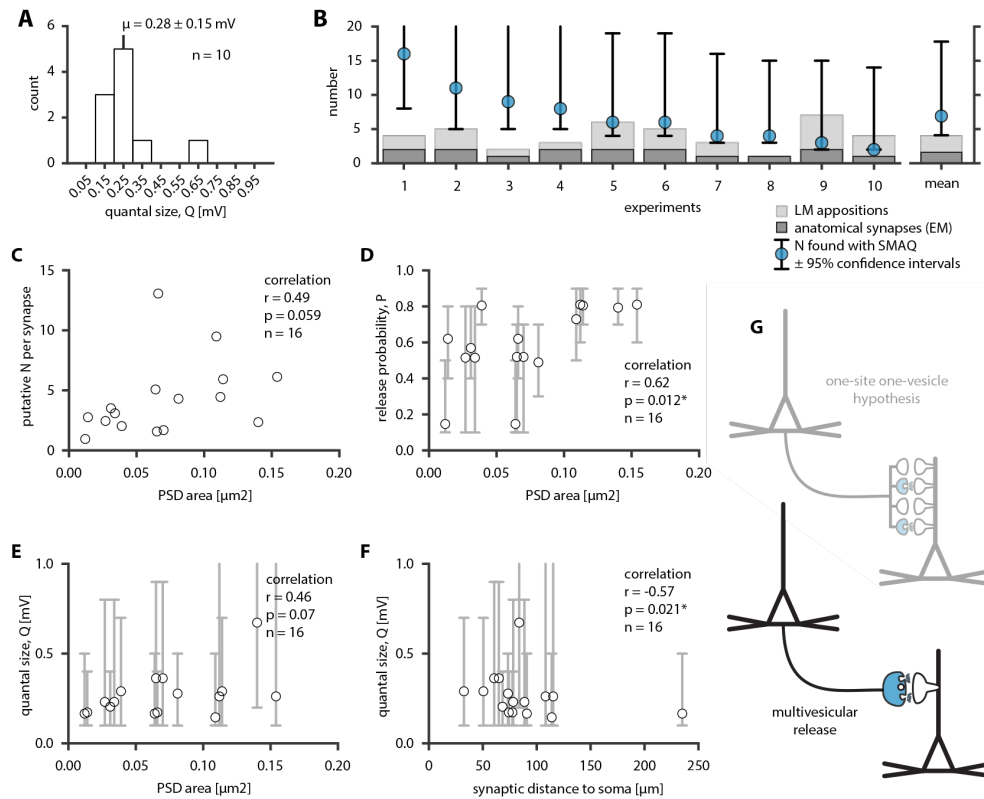
Figure 19. The number of release sites exceeded the number of anatomical synapses, indicating that neocortical synapses are capable of multivesicular release. A Distribution of quantal sizes found with SMAQ for the 10 connections (μ, mean ± standard deviation). **B** Comparison of the number of LM appositions, anatomical synapses, and release sites for the 10 connections in the study. Sorted by descending number of release sites. In all experiments except number 9, the lower CI bound for the number release sites exceeded the number of anatomical synapses. **C** Scatter plot showing the putative number of release sites per synapse versus PSD area (see text). When two synapses were formed, the total N made by a connection were assigned to the synapses following the ratio of PSD areas. **D** Scatter plot showing relationship of release probability versus PSD area. Grey bars, 95% CI from SMAQ. **E** Scatter plot showing relationship of quantal size versus PSD area. Grey bars, 95% CI from SMAQ. **F** Scatter plot showing relationship of quantal size versus synaptic distance to soma. Grey bars, 95% CI from SMAQ. **G** Our data are inconsistent with the one-site one-vesicle hypothesis (top) and provide evidence for multivesicular release at the excitatory synapses between L2/3 pyramidal neurons in mouse barrel cortex (bottom).

2.4   Extended Results

In this section, data are presented that were acquired during the experiments for the structure-function project, and that could not be included in our final dataset of 10 connected pairs of L2/3 pyramidal neurons for which we were able to relate the ultrastructural features of synapses and the electrophysiological properties of synaptic transmission.

On the one hand, these data include electrophysiological recordings between the pairs of L2/3 pyramidal neurons for which we were unable to recover synapses in EM. On the other hand, these data contain recordings of synaptic transmission between L2/3 pyramidal neurons and L2/3 interneurons. This latter series includes one experiment in which we succeeded in recovering all synapses made between the pyramidal neuron and interneuron in EM and thus could relate structure and function in a similar manner as for our dataset of 10 pairs of pyramidal neurons.

Although these data could not be included in the structure-function dataset, they provide further valuable and interesting insights into synaptic transmission in L2/3 of mouse barrel cortex. These results are discussed in the *Extended Discussion* section of this thesis.

2.4.1   Distribution of mean EPSP amplitudes between connected pyramidal neurons in L2/3

In this study, we recorded from a total of 59 connected pairs of L2/3 pyramidal neurons. Ten of these met our anatomical and physiological quality requirements and were used for the structure-function analyses. The 49 remaining pairs could not be used for the structure-function analyses for various experimental reasons, mainly because one or both cells were not sufficiently filled with biocytin. Nonetheless, these pairs were valuable for characterizing the electrophysiological properties of synaptic transmission in L2/3. Of these 49 remaining pairs, the EPSP amplitudes of 38 pairs were analyzed. 11 pairs were not analyzed for reasons concerning mostly the quality of recordings; this included a low number of evoked EPSPs and instability of recordings, such as strong and frequent fluctuations of the membrane potential or recording noise.

For the 38 analyzed connections, it was our priority to acquire a large dataset of the distribution of EPSP amplitudes between L2/3 pyramidal neurons. Therefore, we did not exclude recordings that were stable for less than 100 consecutive sweeps. On average, these connections contained consecutive stable epochs of recording of 160 sweeps (range of 25 to 425; in case when only 25 sweeps were used, these sweeps were always taken from the initial period of recording).

Thus, taken together with the 10 connected pairs used for the structure-function correlations, a total of 48 connections were analyzed. Their mean EPSP amplitudes ranged between 0.06 mV to 2.25 mV (mean of 0.60 ± 0.49 mV) and the distribution of mean EPSP amplitudes across this population was well-described by a lognormal function (Fig 20 A). Importantly, the EPSPs of the 10 connections that were used for the structure-function analyses spanned the entire spectrum of EPSP amplitudes observed in the study. Intriguingly, their mean EPSP amplitudes were significantly larger than the mean EPSPs of the 38 remaining connections (Fig 20 B, C).

To investigate this effect, the dataset was split into two halves containing equal numbers of experiments. The first half contained the chronologically earlier experiments, which were performed mostly in 2016 and the second half contained the chronologically later experiments, which were performed in 2017. The mean EPSP

amplitudes between these two groups were not significantly different, but the vast majority (78%) of connections with "strong" EPSP amplitudes (defined as exceeding 1 mV), were performed during the latter half of the experiments. During the earlier experiments, only 8% of connections had EPSP amplitudes exceeding 1 mV, while in the later experiments, 29% of connections exceeded 1 mV (Fig. 20 D). This coincided with the fact that from the early experiments, only 3 out of 24 (13%) could be used for the structure-function analyses, while from the latter experiments, 7 out of 24 (29%) could be used (not shown). Thus, the observed bias towards being able to relate structure and function of connections that had larger mean EPSP amplitudes than would be expected from the distribution of EPSP amplitudes across L2/3 could – at least partly – be caused by the overlap of these two effects (see *Extended Discussion*).

Next, we performed SMAQ quantal analysis on the 48 connections to investigate which of the quantal parameters could have mediated the observed bias.
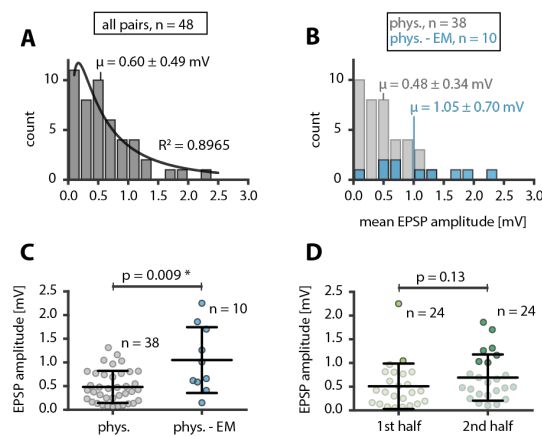
Figure 20. Distribution of mean EPSP amplitudes of all L2/3 pyramidal neuron pairs that were analyzed for the study. A Histogram of mean EPSP amplitudes of all 48 pairs. A log-normal curve was fit to the data. **B** Histogram comparing the mean EPSP amplitudes of the pairs for which physiology and anatomy could be related (phys. – EM) and of pairs, for which only the electrophysiology could be analyzed (phys.). **A**, **B** Mean ± standard deviation indicated. **C** Scatter plots comparing the same data as in B. **D** Scatter plot of the dataset in A, but split chronologically into half. "1st half" contains experiments performed largely in 2016; "2nd half" contains experiments performed in 2017. Solid dots, EPSP amplitudes > 1 mV; faint dots, EPSP amplitudes < 1 mV. **C**, **D** Whiskers in scatter plots represent mean ± standard deviation. The non-parametric Mann-Whitney test was used for statistical comparisons. Asterisk highlights statistically significant difference.

2.4.2   Distribution of quantal parameters of synapses between L2/3 pyramidal neurons.

We were able to perform SMAQ quantal analysis successfully on 30 of the 38 connections that had not been used for the structure-function analyses. In combination with the 10 connections, for which we had successfully related structure and function, we had a dataset of 40 pairs of connected L2/3 pyramidal neurons, for which SMAQ quantal analysis was successful. On average, these connections contained 4.6 release sites. The mean release probability was 0.5 and the mean quantal size was 0.3 mV.

Failures of SMAQ typically manifested themselves in one of two ways: Either SMAQ produced solutions for quantal parameters that were considered "biologically unrealistic" ($N > 20$, $Q > 1.5$ mV), or it produced solutions that contained one or more quantal parameters with a negative sign. The results were discarded in both scenarios. (Note again that to be able to acquire a large dataset of the distribution of EPSP amplitudes, we loosened our requirement that at least 100 consecutive stable sweeps had to be included in the dataset for SMAQ.)

To investigate the underlying cause of the larger EPSP amplitudes of the 10 connections used for the structure-function analyses, we compared the quantal parameters of these 10 connections against the remaining 30 connections (Fig. 21). We found that the significantly larger EPSP amplitudes of these 10 connections correlated with their significantly larger number of release sites and a larger release probability. The quantal sizes were not different.

Confidence intervals for SMAQ are not reported here, but they contained the typically large ranges that were described for the 10 connections, for which we have related structure and function and for the 5 connections, for which we compared SMAQ to the method of fitting binomial models to peaky histograms.
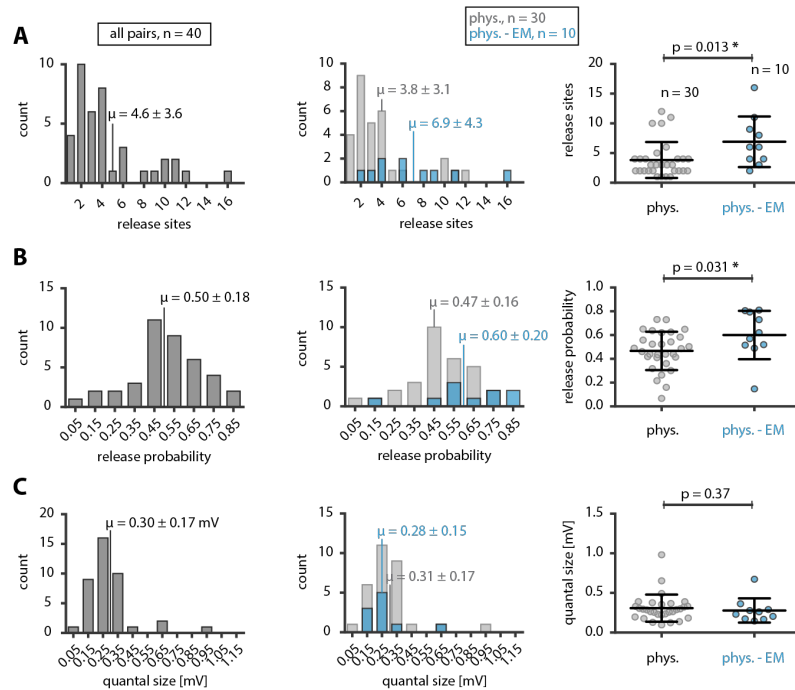
Figure 21. Quantal parameters across all pairs of L2/3 pyramidal neuron, for which SMAQ quantal analysis could be performed. A SMAQ solution for number of release sites. Left, histogram showing N for all 40 connections, for which SMAQ was successful. Middle, histograms comparing N of pairs, for which physiology and anatomy could be related (phys. − EM) and of pairs, for which only the electrophysiology could be analyzed (phys.). Mean ± standard deviation indicated. Right, Scatter plot of same data as in middle panel. **B** SMAQ solution for release probability. Same panel layout as in A. **C** SMAQ solution for quantal size. Same panel layout as in A, B. **A − C** Whiskers in scatter plots represent mean ± standard deviation. The non-parametric Mann-Whitney test was used for statistical comparisons. Asterisks highlight statistically significant differences. 95% CIs for SMAQ are not reported.

2.4.3   Synaptic connections between pyramidal cells and interneurons in L2/3

2.4.3.1   Mean EPSP amplitudes and quantal parameters of synaptic transmission

In addition to recording synaptic transmission of excitatory synapses between pairs of L2/3 neurons (excitatory to excitatory, E -> E), we also obtained recordings from 22 connections between pyramidal cells and interneurons (excitatory to inhibitory, E -> I). Because the priority of the project was to relate structure and function of synapses made between L2/3 pyramidal neurons, we analyzed the evoked EPSP recordings of only 4 E -> I connections. On average, they contained consecutive stable epochs of recording of 294 sweeps (range of 200 to 400) and had an average mean EPSP amplitude of 1.42 mV, which was significantly larger than the mean EPSPs of the 48 E -> E connections (Fig. 22 A).

We were able to perform SMAQ quantal analysis on 3 of the 4 E -> I connections and found that neither the number of release sites nor the release probability were different between E -> I connections and E -> E connections (Fig. 22 B, C). Interestingly, however, the quantal size of the E -> I connections was found to be significantly larger than the quantal size of the E -> E connections (Fig. 22 D).
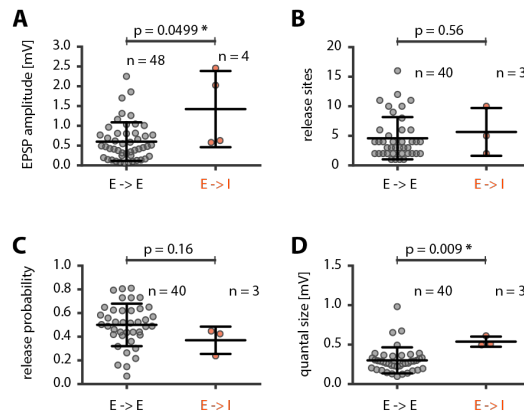
Figure 22. Comparison of synaptic transmission between L2/3 pyramidal neurons (E -> E) and between L2/3 pyramidal cells and L2/3 interneurons (E -> I). A Scatter plot comparing mean EPSP amplitudes of E -> E connections with mean EPSP amplitudes of E -> I connections. **B – D** Comparison of quantal parameters for E -> E and E -> I connections, for which SMAQ quantal analysis could be performed. **B** Scatter plot showing the number of release sites of E -> E and E -> I connections. **C** Scatter plot showing the release probabilities of E -> E and E -> I connections. **D** Scatter plot showing the quantal sizes of E -> E and E -> I connections. **A – D** Whiskers in scatter plots represent mean ± standard deviation. The non-parametric Mann-Whitney test was used for statistical comparisons. Asterisks highlight statistically significant differences. 95% CIs for SMAQ are not reported.

2.4.3.2   Structure-function observations of an E -> I connection

For a single E -> I connection, we reconstructed the labeled presynaptic axon and postsynaptic dendrite in LM and performed subsequent correlated EM of all axodendritic appositions (Fig. 23). In LM, we found 3 appositions between the presynaptic axon and the shaft of the smooth dendrite of the interneuron (Fig. 23 A, B). In striking difference to the anatomy of the E -> E connections, synapses were discovered at EM at all of these 3 appositions (Fig. 23 D). In fact, at one of the appositions (apposition 2 in Fig. 23), the presynaptic axon formed two synaptic contacts with the smooth dendrite, one of them being a *bouton terminaux* and one an *en-passant bouton* (Fig. 23 C). Thus, a total of 4 anatomical synapses were formed between the pyramidal neuron and the smooth dendrite of the interneuron. Three boutons were of the *terminaux* type, and one an *en-passant bouton* (Fig 23 B, C). The PSDs made by the 4 boutons were of strikingly similar size (Fig 23 E; not quantified systematically). No tilt series were acquired and the PSDs were only reconstructed by one person.
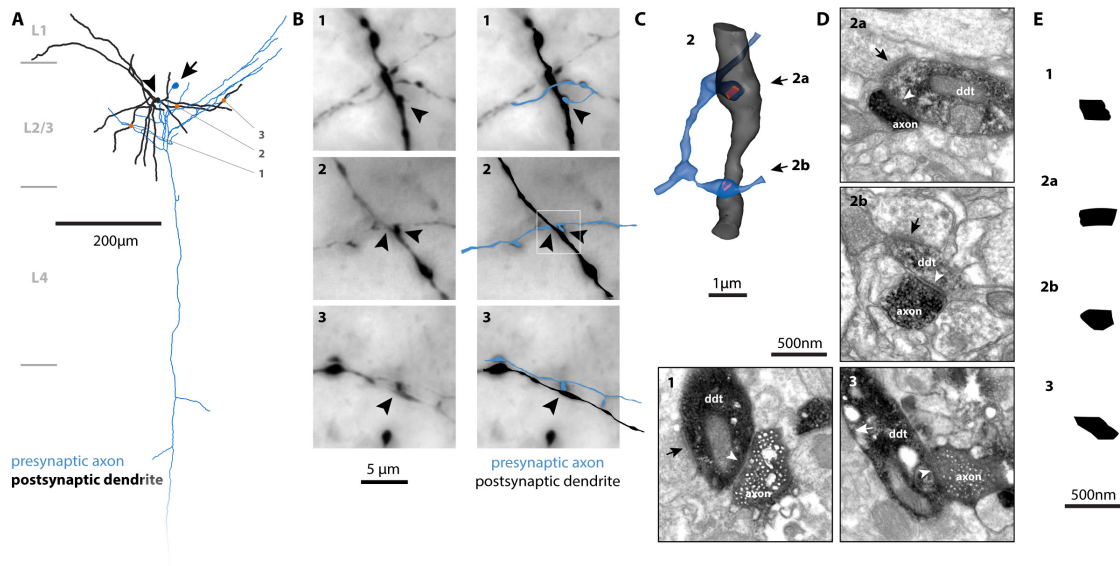
Figure 23. Correlated LM-EM of synaptically connected E -> I pair revealed that all axodendritic appositions were anatomical synapses. A Full 3D LM reconstruction of presynaptic axon of pyramidal cell (blue) and postsynaptic dendrite of interneuron (black). In LM, three appositions (orange dots, numbered) were identified. Arrow, soma of presynaptic pyramidal neurons; arrowhead, soma of postsynaptic interneuron. Cortical layers indicated. **B** Left, high-magnification LM images of the three LM appositions, numbering corresponds to A. Right, overlays of manual drawings of contact points, made from LM stacks and EM reconstructions (not shown). White box indicates position of the EM reconstruction in C. Arrowheads, locations of potential synapses. **C** 3D EM reconstruction of LM apposition 2. Two anatomical synapses were formed (orange, PSDs). Arrows indicate positions of corresponding micrographs in D. **D** Electron micrographs of the four LM appositions revealed that anatomical synapses were formed at all of them. Numbering corresponds to A – C. Arrowhead, PSD of synapses between labeled presynaptic axon and labeled postsynaptic dendrite (ddt). Arrows, synapses formed by unlabeled boutons with the labeled dendrite. **E** *En-face* representations (2D projections) of the four reconstructed PSDs.

Finally, we sought to compare the structure-function relationship of the E -> I synapses with the structure-function relationship we had discovered for the E -> E synapses between L2/3 pyramidal neurons.

For the E -> I connection, for which we had recovered the synapses in EM, the mean EPSP amplitude during the stable epoch of recording (400 sweeps) was 2.46 mV. However, during the course of the recording, the EPSP amplitude had quickly and strongly depressed by over 30% from 3.66 mV during the initial 75 sweeps to 2.46 mV during the stable epoch, which ranged from sweeps 76 to 475. Because the initial 75 sweeps were considered to represent the strength of transmission more accurately than the depressed EPSPs during the stable epoch of recording, only the initial 75 sweeps and their mean were plotted in figure 24.

In figure 24, we overlaid the EPSP-cPSD relationship of the E -> I connection onto the scatter plot showing the EPSP-cPSD relationship for the 10 E -> E connections. We found that the E -> I connection lay well above the line that was fit through the E -> E connections. Not only was the mean EPSP amplitude above this line, multiple observations of individual EPSPs extended as high as 5 to 8 mV – magnitudes we had never encountered in this study for E -> connections.

Unfortunately, SMAQ quantal analysis was unsuccessful for this connection.

To understand this difference, it is important to consider the biophysical differences between pyramidal cells and interneurons. The interneuron is likely electrotonically more compact because of its more compact dendritic arborization (Fig. 23 A). Furthermore, the noise of the baseline membrane potential (noise standard deviation of 0.22 mV during the initial 75 sweeps) was approximately twice as high as the noise usually encountered in recordings from pyramidal neurons, which likely reflects the overall higher density of synapses on the proximal dendritic tree of the interneuron (Ahmed et al., 1997; Bopp et al., 2017).
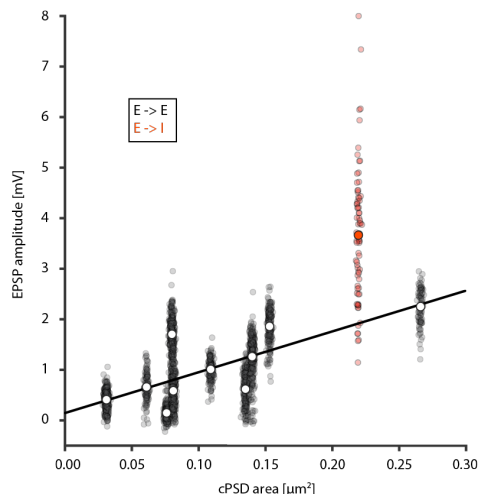

Figure 24. Comparison of cPSD-EPSP relationship between E -> E and E -> I connections. The underlying plot is the same as in figure 15 E. The single E -> I pair for which all synapses were recovered in EM is plotted on top (orange). The initial 75 sweeps of recording of this E -> I connection were plotted, because after this period, the mean EPSP amplitude depressed quickly by > 30%.

2.5 Discussion

We characterized synaptic transmission between pyramidal neurons in L2/3 of mouse barrel cortex using a novel form of quantal analysis. Then, we related structure to function by recovering all the anatomical synapses between the recorded neurons through correlated LM-EM. We were able to detect unambiguously for all axodendritic appositions in LM whether they formed anatomical synapses and measured the synapse size in EM. We discovered that (1) PSD area correlates with EPSP amplitude and that (2) single anatomical synapses contain multiple neurotransmitter release sites. Thus, cortical synapses are capable of multivesicular release, implying that the release of a single vesicle does not saturate all the postsynaptic receptors.

We found on average 4 LM appositions between labeled presynaptic axon and postsynaptic dendrite of connected pairs. This is comparable to previous correlative studies in rat barrel cortex that reported values between 2.6 and 5.5 with similar ranges as found by us (Markram et al., 1997; Feldmeyer et al., 1999, 2002, 2006; Lübke et al., 2000, 2003; Silver et al., 2003; Hardingham et al., 2010).

2.5.1 Most LM appositions are not anatomical synapses between labeled axon and dendrite

We performed high-magnification 3D EM on all LM appositions for all our experiments. Following slice recordings, we achieved high fidelity ultrastructural preservation and were able to resolve synapse specializations, including vesicles in the presynaptic bouton, a synaptic cleft, and – most importantly – the PSD. In all cases, we could unambiguously detect when no synapse was made: labeled axon and dendrite formed synapses with unlabeled partners in the neuropil and a physical separation remained between the structures. Likewise, when synapses were found, their identification was unambiguous: axodendritic contacts always extended over multiple sections and the hallmarks of synaptic specializations were present.

One of our key findings is that the majority of LM appositions did not form anatomical synapses between the labeled structures so that the existence of an apposition was not predictive of a synapse (Mishchenko et al., 2010; Kasthuri et al., 2015). Typically, putative synapse numbers are estimated from LM, with supporting data from less stringent EM (Markram et al., 1997; Feldmeyer et al., 1999, 2002, 2006; Lübke et al., 2003; Silver et al., 2003; Hardingham et al., 2010). This has supported the central dogma that neocortical synapses contain only a single release site (Silver et al., 2003; Hardingham et al., 2010). Our findings suggest a different interpretation of these data.

It is a striking observation that in some instances anatomical synapses were formed where it might not have been expected from LM. Typically, in these instances, axon and dendrite crossed on top of each other with a separation in the z-plane (Fig. 25). It remained hidden to the LM observer that, at these sites, the dendrite sometimes extended a spine in the z direction towards the axon and formed a synapse with it. Because the bouton-spine complex was located between axon and dendrite, it could not be identified as such from LM, while the large separation in z suggested that no synapse could be formed here. This observation further highlights that stringent EM is required for all axodendritic appositions and for all axodendritic crossings that are separated by several μm in the z-dimension.
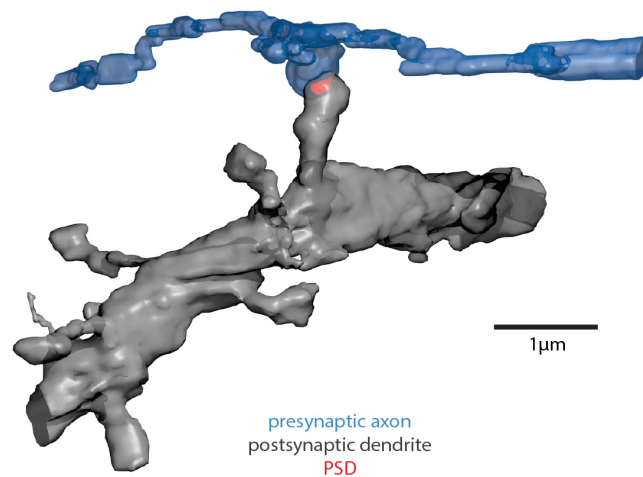
presentation labels:
presynaptic axon
postsynaptic dendrite
PSD

Figure 25. Conformation of an axodendritic contact that could be overlooked easily from LM alone. 3D EM reconstruction of a synapse between L2/3 pyramidal neurons. Axon and dendrite traverse in different z-planes. In LM, the spine extending towards the axon in the z-dimension is covered by the presynaptic axon that is crossing on top and can be missed easily.

2.5.2   Recovering and measuring the PSD area

Biocytin reaction-product in pre- and postsynaptic structures poses a challenge for reconstructing PSD areas. To overcome this, we employed a battery of technical procedures: one is the linear relation between PSD area and spine size, which we (Bopp et al., 2017) and others (Harris and Stevens, 1989; Schikorski and Stevens, 1999; Arellano et al., 2007) have observed for naïve, unlabeled synapses in the neuropil. Here, we found the same relationship between spine head volume and PSD area for the biocytin-labeled synapses. This suggested that we were able to recover reliably the PSD area across experiments despite the challenge of reaction-product in the spines. An additional observation that supports this conclusion was that *en-face* representations of our reconstructed PSDs displayed the spectrum of PSD shapes that has previously been described in cortex (Fig. 16 B). This included the tendency that larger synapses formed perforated PSDs (Peters et al., 1991; Peters and Palay, 1996; Bopp et al., 2017).

2.5.3   Multivesicular release enables the prediction of synapse size from EPSP amplitude

Our findings are fully consistent with our hypothesis that mean EPSP amplitude reflects PSD size if synapses contain multiple vesicle release sites, because all quantal parameters can be mapped onto a single – or few anatomical synapses. On the other hand, our structure-function data are inconsistent with the possibility that single synapses contain only one release site and that synapse size should correlate directly with the quantal amplitude (Q) because postsynaptic receptors would always saturate. The situation we have described is very different from this latter scenario, because all EPSP recordings showed quantal fluctuations that were not due trivially to recording noise, but indicative of multiple release sites acting on a postsynaptic receptor array that evidently could not be

saturated by release of a single vesicle. Thus, N cannot be discovered simply by counting the number of appositions seen in the LM (as previous studies have done), or the number of synapses revealed by EM.

2.5.4 Confirmation for ultrastructural studies at synaptic resolution

Our central finding that EPSP amplitude is related to synapse size in the neocortex *in vitro* constitutes an important confirmation for ultrastructural studies at synaptic resolution and the field of connectomics in particular, which has been lacking to date. Several structure-function relationships have been elucidated, such as the correlation between PSD area and estimated AMPAr number, or the correlation between active zone area and release probability; but how these structure-function relationships relate to the strength of synaptic transmission as measured by the EPSP amplitude, has remained experimentally unproven. Thus, our findings provide the missing experimental validation of how structural features of synapses, such as PSD area, relate to the physiological properties of signal transduction in the brain.

Our data could be a one of the key steps towards giving functional attributes to the structural connectomes of neocortex. This could be desirable for implementing wiring diagrams acquired through connectomics *in silico* and for subsequently simulating their behavior. On this endeavor, our work could provide the data that are necessary to tune synaptic weights of such models and to calibrate their responses. Constructing such circuit simulations and setting their parameters will ultimately require much more detailed biophysical data than we can provide here. This includes synaptic conductances and time constants, the biophysical properties of membranes, and input resistances and time constants of different cell types *in vivo* and *in vitro*, etc. However, the relationship of cPSD area and somatic EPSP amplitude we have found *in vitro* could be used as a calibration of the tuned circuit models against experimental data.

2.5.5 The anatomical substrate of the three quantal parameters

Because PSD area is a postsynaptic metric, its correlation with P, which is widely regarded as a presynaptic property, might seem surprising at first, but is in fact consistent with the literature. PSD area is identical with the active zone area in rodent cortex and hippocampus (Schikorski and Stevens, 1997, 1999; Murthy et al., 2001; Rollenhagen et al., 2014, 2018) and should thus reflect the correlation between active zone size and RRP size and P (Harris and Stevens, 1989; Murthy et al., 2001; Branco and Staras, 2009; Matz et al., 2010; Holderith et al., 2012; Rollenhagen et al., 2014).

While estimated AMPAr number is proportional to PSD size (Nusser et al., 1998; Tanaka et al., 2005), we found no correlation between Q and PSD area. Importantly, computer simulations showing that AMPAr are only activated within small hotspots around the fusion pore have suggested that it is not the number of AMPAr per synapse that determines Q, but rather the AMPAr density (Raghavachari and Lisman, 2004).

Interestingly, we found that Q decreased as a function of the synaptic distance to soma. In the hippocampus, AMPAr density increases as a function of distance along the dendrite, a potential mechanism to counteract attenuation (Andrásfalvy and Magee, 2001; Nicholson et al., 2006). If this is the case for neocortical neurons, it seems insufficient to counterbalance attenuation entirely.

Our results raise the intriguing question whether the number of release sites could be predicted from synapse size. Support for this notion comes from the hippocampus, where the number of nanodomains per spine are correlated with PSD area (Fukata et al., 2013; Nair et al., 2013).

Despite a large range in PSD sizes and estimated N, however, we found no significant correlation between N and cPSD area. Neither did we find a correlation when we split the dataset and computed the putative N per PSD for the 16 individual synapses. Whether an underlying biological effect is the cause of this, or the precision of SMAQ was insufficient to recover N precisely enough, remains unclear.

The widely varying shapes of perforated synapses, which are typically found on spines, is intriguing. It is a feature worth investigating using super-resolution LM to examine how the distribution and density of AMPAr relates to the overall structure of perforated synapses.

2.5.6   Adequacy of simple binomial statistics

We found, with a slice thickness of 300 µm, that only 1 or 2 anatomical synapses were formed between connected neurons and that single presynaptic boutons contained multiple release sites. Because multiple release sites resided within the same biophysical compartment (the presynaptic bouton), these release sites were likely subject to similar intracellular Ca^{2+} concentrations in the event of an action potential. Therefore, P between release sites within a bouton was likely relatively uniform. Because synapses within a connection tend to display less size-variance than the distribution of synapses in the neuropil suggests [qualitative observations from present study and (Bartol et al., 2016; Motta et al., 2018)], P across these sites should display less variance than release probabilities across cortex.

Synaptic vesicles were released at only one or two anatomical sites. In the latter scenario, the two synapses were located at surprisingly similar dendritic distances with respect to soma, except in one experiment. Thus, our recordings likely contained very low inter-site variance (Type II) due to differential attenuation, while intra-site variance (Type I) must have dominated (Walmsley, 1993; Jack et al., 1994; Wahl et al., 1995). This indicates that Q was likely uniform between release sites of a connection and subject to similar noise sources, even in the cases when two synapses were formed. When two synapses were formed by a connection, they had different PSD sizes. However, this does not imply that the two synapses should possess different quantal sizes. We found no correlation between Q and PSD area and not the number of AMPAr per synapse should determines Q, but rather the AMPAr density (Raghavachari and Lisman, 2004), a variable we cannot assess in this study.

Taken together, under these conditions, the simple binomial model should provide a sufficiently good approximation of synaptic transmission between L2/3 pyramidal neurons without the need to resort to compound binomial models (Larkman et al., 1997; Silver et al., 2003; Brémaud et al., 2007).

2.5.7 Considerations regarding the Stochastic Moments Analysis of Quanta

2.5.7.1 Validation of SMAQ

Central moments of EPSP distributions are routinely used to extract information about quantal parameters (Redman, 1990; Voronin et al., 1992; Dityatev and Clamann, 1998; Taschenberger et al., 2005) and can provide unbiased estimates of quantal parameters (Dityatev and Clamann, 1998). However, skewness (the third central moment) has rarely been used, despite its power to inform about of P, even when N is unknown (Taschenberger et al., 2005). It follows from the binomial equation that synapses giving rise to right-skewed distributions (with a positive sign on skewness) operate under P < 0.5, while left-skewed histograms (with a negative sign on skewness) indicate that P > 0.5, independent of N.

Furthermore, skewness is independent of Q, which allowed us to combine the equations for the first three central moments of binomial distributions and successfully derive all three quantal parameters of synaptic transmission. Following Bayesian logic, we developed a statistical test using Monte-Carlo simulations, which provided certainty bounds on our estimates that were more rigorous than CIs derived by more commonly-used bootstrap resampling techniques. We termed this method *Stochastic Moments Analysis of Quanta* and compiled it into an easy-to-use toolbox.

We tested SMAQ on EPSP histograms that displayed evenly-spaced peaks and found that its predictions were in excellent accordance with the method of fitting peaky histograms. Importantly, solutions of both methods were associated with significant uncertainty. CIs from bootstrap resampling were comparable between methods, which suggests the two methods possess similar accuracy for the ranges of quantal parameters present in the connections tested here.

It is noteworthy that CIs for SMAQ computed with bootstrap resampling were much narrower than CIs for SMAQ computed from the distributions of quantal parameters that could have produced the same solutions. This reflects that the latter – which we used throughout this study to analyze our results – answers a more rigorous statistical question.

Importantly, only the prediction of Q was largely error-free when fitting peaky histograms – as expected, given the information contained in the structure of peaks, while N and P were associated with larger uncertainty. This is in good agreement with reports that quantal parameters obtained with the method of fitting peaky histograms can contain large uncertainty (Hardingham et al., 2010). Thus, quantal analysis should not be regarded as an exact method.

Additional validation for SMAQ arises from the fact that its predictions for Q (Fig. 19 A) are in excellent agreement with the range of Q usually reported for neocortical synapses in rodents using different methods (Silver et al., 2003; Hardingham et al., 2006, 2007, 2010; Loebel, 2009; Rollenhagen et al., 2018).

2.5.7.2   Applicability of SMAQ

SMAQ contains a number of useful advantages over existing QA methods, which makes it an interesting option for many applications.

Fitting binomial models to peaky histograms is powerful because it produces visually reassuring fits, but it requires that amplitude histograms display evenly-spaced peaks, which may be rare. This strong constraint places researchers in the unfortunate dilemma of having to discard a large number of histograms and leaves them with a small and obviously biased dataset (Koester and Johnston, 2005; Hardingham et al., 2006, 2007, 2010; Rollenhagen et al., 2018). The exact nature of the bias remains elusive, but it is probable that underlying biophysical properties, such as different types and degrees of quantal variance – and not experimental infelicities - are at the core of the appearance or not of peaks (Jack et al., 1994; Hardingham et al., 2010).

In addition, the method requires a battery of statistical tests to verify the statistical robustness of peaks (Clements, 1991; Stratford et al., 1997) and goodness-of fit metrics (Hardingham et al., 2006, 2007, 2010).

Importantly, SMAQ places none of those constraints on the data: we were able to apply the method to all EPSP distributions we tested, given that extended stable epochs of recording were used. This leads to two key advantages: results obtained with SMAQ are not biased by the requirement of equally-spaced peaks in histograms and fewer samples have to be acquired before a sufficient *n* is reached. In addition, SMAQ does not require that data are acquired under multiple different experimental conditions, such as the use of different concentrations of extracellular Ca^{2+} needed for multiple-probability fluctuation analysis.

These advantages make SMAQ easy to implement both from an experimental and data-analysis perspective and allow QA to be routinely used on various types of EPSP recordings.

2.5.8   Implications of multivesicular release for the circuits of neocortex

The idea that single synapses in the neocortex release only a single vesicle in the event of an action potential and that the neurotransmitter content of that single vesicle is sufficient to saturate all postsynaptic receptors has been a widespread belief (personal communications with Kevan Martin, Ken Stratford, and Florian Engert). Our findings that single anatomical synapses must be capable of releasing multiple vesicles raises the burning question of what the implications for cortical circuits are.

2.5.8.1   Changing synaptic efficacy

If each anatomical synapse would contain only a single release site, then changes in synaptic efficacy at existing anatomical synapses could only be achieved by changing P or Q. N would be determined by the number of anatomical synapses. Changing N would require that new physical synapses were formed between presynaptic axon and postsynaptic dendrite. On average, we found 4 ± 1.9 LM appositions between connected pairs with a range of 1 to 7. The number of LM appositions would constitute the upper limit of N that could be formed by a connection.

However, since anatomical synapses contain multiple release sites, synaptic efficacy could be tuned additionally by changing N, without the need for structural remodeling. In the hippocampus, the number of nanodomains scales with the PSD area (Nair et al., 2013). If the nanodomain and the trans-synaptic nanocolumn are indeed the structural equivalents of the release site, then it would be expected that during long-term depression (LTD) or long-term potentiation (LTP) release sites should be added, or removed from the synapse, respectively (Engert and Bonhoeffer, 1999).

Thus, the design in which a single synapse contains multiple vesicle release sites should allow more flexible changes in synaptic efficacy.

2.5.8.2   Synaptic scaling

This raises the intriguing question of whether there is an upper limit on the number of release sites that can be contained within a single anatomical synapse and whether this limit is reached?

There are two conceivable strategies of how neocortical circuits could be wired. One option would be for a connection to minimize the number of anatomical synapses and maximize the size of the synapses until a possible size limit is reached, before an additional physical synapse is formed. This strategy could minimize the number of anatomical synapses and might allow a higher convergence of presynaptic partners that could form synapses with a given postsynaptic neuron.

The alternative strategy is that multiple anatomical synapses are formed by a connection and scaled in parallel as the synaptic efficacy between pre- and postsynaptic neuron changes. Our data are consistent with the latter scenario. In 6 out of 10 connections, we observed that multiple synapses were formed. In these cases, we did not identify striking size variations between the two synapses, as would be expected from the first strategy. The observation that synapses within a connection tend to display less size-variance than the distribution of synapses in the neuropil suggests has been captured quantitatively by other studies (Bartol et al., 2016; Motta et al., 2018)].

2.5.8.3   Models of neocortical circuits

Our finding that most LM appositions are not anatomical synapses in the EM has important implications for *in silico* models of neocortical circuits.

Prevalent models were constructed from a combination of data from *in vitro* paired recordings and their recovered anatomy and *in vivo* recordings (Sarid et al., 2007, 2015) and assumed that a pyramidal neuron in L2/3 of rat barrel cortex receives synapses from 270 other L2/3 neurons. These numbers were derived from the fact that L2/3 neurons form on average ∼ 900 boutons within their innervation domain in L2/3 and thus should in turn receive 900 boutons from other L2/3 neurons. Under the assumption that the number of putative synaptic contacts between connected L2/3 neurons is 3 and that 10% of boutons are made on interneurons, each L3/4 pyramidal neuron is assumed to receive synapses from 270 other L2/3 neurons (Feldmeyer et al., 2006). Similar reasoning – also based on the assumption that all putative synapses are anatomical synapses – was used to derive that about 300 – 400 L4 neurons converge onto a single L2/3 neuron, with each L4 neuron forming on average 4.5 synapses on the L2/3 neuron (Lübke et al., 2003). Because the number of putative synapses far exceeds the

number of anatomical synapses, such models underestimate the convergence of presynaptic neurons onto a L2/3 pyramidal neuron. Because of this underestimation, activation of a certain fraction of afferent neurons could have a more powerful effect on the firing of the L2/3 neuron than suggested by these models.

However, it is important to emphasize that connectivity data from slice recordings is generally unsuitable for constructing computational models of neocortical circuits, unless great care is taken to compensate for the fact that much of the neuropil is lost during the slicing procedure (Fig. 26). The total number of synapses made between two L2/3 neurons cannot be derived reliably from slice recordings.
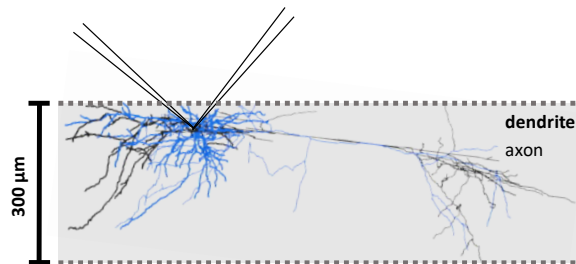

Figure 26. Neurite loss in slice recordings. Full 3D LM reconstructions of two synaptically-connected pyramidal neurons in L2/3 of mouse barrel cortex. The reconstructions are viewed from the side and are oriented with the cutting plane pointing upwards to highlight the amount of neuropil that is lost due to the slicing procedure. Recording pipettes are shown schematically.

2.5.9   Our data in relationship to excitatory synaptic transmission in vivo

The *in vitro* preparation offers several important experimental advantages that were necessary for combining successfully whole-cell recordings with EM of all LM appositions. This includes a higher experimental throughput and extended periods of recordings from connected neurons. As we were forced to discard the majority of experiments, which did not meet our anatomical quality criteria, this proved to be crucial.

Just as importantly, the *in vitro* preparation allowed us to record from connections comprised of few anatomical synapses and enabled us to relate structure and function of one or two synapses directly. This was made possible because a large portion of the neuropil of the connected neurons was cut and the number of synapses in the connection was reduced (Fig. 26).

However, the question arises of how the structure-function relationship we discovered *in vitro* relates to the *in vivo* situation. There are several important biophysical differences between the *in vitro* and *in vivo* setting that can affect this structure-function relationship: *in vitro*, the slice is relatively inactive and almost no spontaneous action potentials can be observed. This results in low synaptic background activity and a more depolarized membrane potential and a higher input resistance of neurons. *In vivo*, the circuits are well preserved and can display high activity levels, depending on the regime of anesthesia. Thus, neurons can be bombarded with high synaptic background activity, which results in a more depolarized membrane potential and a lower input resistance, because the membrane becomes leaky (Koch, 2004). Thus, the conductance state of neurons is different and more unstable *in vivo* and EPSP amplitudes are overall lower *in vivo* compared to slice recordings (Jouhanneau et al., 2015).

Therefore, the slope of the relationship between cPSD area and EPSP amplitude we found *in vitro* can be expected to be flatter *in vivo*. Experimentally, this effect is another strong advantage of the *in vitro* preparation, because it allows for a "cleaner" recording of synaptic transmission – *in vitro*, synapses on the dendritic tree are electrotonically closer to the soma than *in vivo* [see for example (Bernander et al., 1991; Koch, 2004)].

2.6 Extended Discussion

In this section, the data of the *Extended Results* section are discussed. These data were acquired during the experiments for the structure-function project but could not be included in our final dataset for relating physiology and ultrastructure of synapses between L2/3 pyramidal neurons.

2.6.1 Synaptic transmission between pyramidal neurons in L2/3 of barrel cortex

The mean EPSP amplitudes we measured between pairs of pyramidal neurons in L2/3 match well with the values reported in the literature for the same connection in rodent barrel cortex [see for example (Feldmeyer et al., 1999, 2006; Silver et al., 2003; Hardingham et al., 2006, 2007, 2010; Rollenhagen et al., 2018)].

It is an important observation for our structure-function analyses that we have managed to relate structure and function of connections that span the entire range of synaptic transmission strengths we observed in L2/3.

It is however intriguing that the 10 connections for which we were successful in relating structure and function were on average stronger than the remaining 38 connections for which we had no EM. This effect suggests a bias, which could partly be caused by the increasing experience of the experimenters over time. It is known that certain spatial relationships between the locations of the somata of two neurons influence the chances of finding synaptic connections. Neurons that are located proximal (< 50 μm) to each other, for example, are connected with higher probability than neurons whose somata are more distant from one another (> 50 μm) [see for example (Seeman et al., 2018)]. Such observations are often anecdotal because they are hard to quantify and are passed on from the teacher to the student (personal communication with Ora Ohana).

At the same time, we learned that a certain spatial relationship between the cells in the slice increased our chances of finding pairs that were reciprocally connected, of finding pairs with EPSP amplitudes exceeding 1 mV, and that this often coincided: reciprocally connected neurons often formed synapses that had large EPSP amplitudes (not quantified systematically). During the project, it remained a priority to record from as many connections as possible to increase the numbers of pairs for which we could attempt to relate structure and function. Thus, we aimed to record from spatial configurations of neurons, which we knew yielded high chances of finding connections.

Not only did we record the vast majority of connections exceeding 1 mV in the latter phase of the project, also our success rate in recovering the synapses in the EM was greatly increased then in comparison to the early phase, which can also be attributed largely to the experience gained over time.

Thus, it is probable that our bias of being able to relate structure and function for pairs with larger mean EPSP amplitudes could – at least in part – be due to the fact that most of these pairs were recorded in the latter phase of the experimental period, when we were also more successful in recovering all synapses after recordings.

2.6.2   Quantal parameters of synaptic transmission at E -> E connections in L2/3

When we performed SMAQ quantal analysis for connections between pyramidal neurons, we found that the variance in the quantal parameters was remarkably low. The large ranges of the Bayesian-inspired 95% CIs that were usually found would suggest that the solutions of SMAQ should be associated with large uncertainty and thus large variance. This is particularly intriguing given that sometimes less than 100 sweeps were used for the analyses shown in figure 21.

At the same time, the quantal parameters we found for the E -> E connections are in excellent agreement with the average values and ranges of quantal parameters typically found across the rodent cortex [see for example (Feldmeyer et al., 1999, 2006; Silver et al., 2003; Hardingham et al., 2006, 2007, 2010; Rollenhagen et al., 2018)]. For example, the average number of release sites we found (4.6) matches exactly the 4.4 release sites reported by Silver et al. (2003) between L4 and L2/3 neurons using multiple probability fluctuation analysis in rat L2/3 and slightly exceeds the 3.6 release sites between rat L2/3 neurons reported by Hardingham (2010) using the method of fitting binomial models to peaky histograms.

Thus, SMAQ quantal analysis is likely more accurate than the Bayesian-inspired CIs suggests. The wide range of these CIs constitute theoretical confidence bounds for quantal parameters, which might not be reached in biology. SMAQ quantal analysis could provide a powerful alternative to existing methods of quantal analysis and it would be important to explore the method further and investigate such observations systematically.

2.6.3   Synaptic transmission between pyramidal neurons and interneurons in L2/3

In addition to our detailed characterization of E -> E connections, we analyzed synaptic transmission of a small number of E -> I connections in L2/3 of mouse barrel cortex. Despite the small dataset, several interesting observations could be made: the mean EPSP amplitude of E -> I connections was larger than of E -> E connections and this coincided with a significantly larger quantal size.

It is known that E -> I connections operate with higher synaptic efficacy compared to E -> E connections, which is thought to be an important factor for mediating precisely-timed, reliable, and pronounced inhibition following a wave of driving excitation in cortical circuits (Douglas et al., 1989; Ohana et al., 2012).

E -> I connections not only evoke larger-amplitude EPSPs compared to E -> E connections, also the EPSP rise time is shorter and the EPSP onset after a presynaptic action potential is faster [see for example (Ohana et al., 2012)]. Anatomical and physiological factors were found to mediate these effects. Synapses made by pyramidal neurons onto interneurons are often located proximal to the soma, which could result in the larger EPSP amplitudes and fast EPSP rise-times because of cable properties (Ohana et al., 2012).

At the same time, the AMPAr contained in excitatory synapses formed with cortical interneurons possess a different composition of subunits. In particular, they lack the GluR2 subunit, which is characteristic of synapses in E -> E connections and are instead composed predominantly of the GluR1 subunit (Geiger et al., 1995; Kondo et al., 1997). AMPAr containing the GLuR1 subunit are associated with stronger synaptic conductances and faster channel kinetics. For example, AMPAr in the thalamocortical synapses onto L4 interneurons lack the GluR2 subunit,

and the evoked EPSPs in these interneurons express quantal amplitudes that are several-fold larger compared to EPSPs elicited by thalamocortical synapses in principal neurons in L4, which contain the GluR2 subunit (Hull et al., 2009).

Thus, our findings that the mean EPSP amplitudes in E -> I connections exceeded those of E -> E connections and that this coincided with significantly larger quantal sizes are in excellent agreement with the known synaptic properties of these connections.

2.6.4 Structure and function of E -> I connections

We were able to relate structure and function for one of the recorded E -> I connections; however, we were unable to analyze the stable epoch of EPSP recordings successfully with SMAQ quantal analysis.

Intriguingly, anatomical synapses between the labeled presynaptic neuron and postsynaptic smooth dendrite were found at every LM apposition, which is a striking difference to the E -> E connections, where synapses between labeled structures were found only at 40% of LM appositions. This indicates that different developmental mechanisms could be in place to regulate synapse formation between pyramidal neurons and interneurons.

From a technical perspective, this observation provides additional confirmation for our ability to recover all anatomical synapses between connected neurons in EM. If all LM appositions between E -> E connections would be anatomical synapses – as has been proposed by others – we would have detected it.

When we compared the mean EPSP amplitude of this E -> I connection with its cPSD area, we found that the EPSP amplitude was several times stronger than would be expected from the structure-function relationship we found for E -> E connections.

Because we were unable to perform SMAQ quantal analysis on this pair, we can only speculate whether synapses of E -> I connections are also capable of multivesicular release. If each of the 4 synapses we found in EM would be capable of releasing only a single vesicle, the observed EPSP amplitudes of up to 8 mV could be achieved only with quantal sizes approaching 4 mV. Because the distribution of quantal sizes for the other 3 E -> I connections was very homogenous and centered around ~ 0.5 mV, this is a very unlikely scenario. Thus, our preliminary data suggest that transmission at excitatory synapses on interneurons in L2/3 of mouse barrel cortex also involves multivesicular release.

Although we currently have only a single data-point for structure-function comparisons of E -> I connections, our findings indicate that there could be very pronounced physiological and anatomical differences between E -> E connections and E -> I connections, which likely play a critical role in the organization of cortical circuits. Therefore, it would be desirable to analyze more of the acquired data for E -> I connections and attempt to correlate the ultrastructure of the synapses with the electrophysiological properties of synaptic transmission.

Conclusion

In the first part of this thesis, we investigated the anatomical substrate of the thalamic input to L4 of the primary motor cortex. We found that thalamic synapses formed a minority of synapses in the L4 neuropil of M1 and S1. Thus, M1 L4 possesses the canonical circuit motif of core thalamic input to the middle cortical layer. Because L4 is much thinner in M1 compared to S1, in absolute numbers there are only half as many thalamic synapses in L4 of M1 compared to S1. However, it is likely that single L4 neurons receive equal numbers of thalamic synapses in both areas. This is made possible because M1 L4 contains a lower density of neurons compared to S1 L4 and because thalamic boutons in M1 L4 do not form synapses with the smooth dendrites of GABAergic interneurons. Intriguingly, we found that thalamic synapses in M1 L4 are slightly larger compared to thalamic synapses in S1, this effect is caused by the fact that the lognormal distribution of thalamic synapse sizes in M1 contains a longer and more pronounced tail compared to thalamic synapse size in S1.

However, the exact function of the thalamocortical projection to M1 is difficult to assess from anatomical data alone and it is a profound limitation for the interpretation of ultrastructural data at synaptic resolution, such as the one acquired by us in the first part of this thesis, that we do not understand how the ultrastructural features of even a single cortical synapse relate to its physiological strength. Therefore, it has been experimentally unconstrained whether such quantitative EM studies can inform about the physiology of the underlying circuit, and experimental data has been lacking that could be instructive to infer the physiological properties of synaptic transmission from reconstructions of synapses in the EM.

Although anatomy and physiology are inseparably linked in biology, we are often forced to study them separately and studying one often leaves us blind for the other. This has resulted in a divide between structure and function of neuronal connectivity that has been difficult to bridge and has left anatomy and physiology as largely separate conceptual entities in systems neuroscience.

Anatomical studies using EM can provide measurements of the anatomical weight of connections between different brain regions (Anderson et al., 1998, 2011; Anderson and Martin, 2002, 2005, 2006, 2009; da Costa and Martin, 2009, 2011; Bopp et al., 2017; Koestinger et al., 2017) or cell types (Ahmed et al., 1994, 1997; Bopp et al., 2017) by counting the numbers of synapses and measuring the distribution of PSD sizes.

These numbers, however, can provide only very limited and indirect evidence for the electrophysiological properties of signal transmission that are relevant for the operation of neuronal circuits, including the amplitudes of postsynaptic potentials, rise-times, onset latencies of postsynaptic potentials, and short-term dynamics – but also the biophysical properties of the neuron types that receive the synaptic input. To assess these properties, dedicated electrophysiology studies are necessary (Stratford et al., 1996; Tarczy-Hornoch et al., 1998, 1999; Bannister et al., 2002; Kumar and Ohana, 2008; Ohana et al., 2012).

If the electrophysiology of anatomically well-characterized connections is investigated [for example (Stratford et al., 1996)], it becomes possible to gain a glimpse of how the synaptic ultrastructure relates to synaptic

dynamics, but even then key anatomical features remain unresolved, such as the number of anatomical synapses that contribute to a given recorded postsynaptic potential. This hinders the conclusive elucidation of structure-function relationships.

Therefore, studies are critically needed that bridge the divide between the electrophysiological characterization of synaptic connectivity and the precise anatomical assessment of the same synaptic connections. To acquire such information, it is indispensable to combine detailed electrophysiological characterizations of synaptic transmission with high-fidelity EM because axodendritic appositions in LM provide very little evidence for synaptic connectivity, as we have shown in this thesis.

To bridge this gap, we related structure and function of the same synapses: we recorded pairs of synaptically connected L2/3 pyramidal neurons in mouse S1 *in vitro* and then recovered all synapses between the neurons using correlated LM-EM. We found that the mean EPSP amplitudes between connected neurons correlated with the cumulative area of their postsynaptic densities and that this correlation held when differential dendritic attenuation was corrected for. Furthermore, we discovered that the number of release sites of a connection exceeded the number of anatomical synapses. Therefore, single cortical synapses are capable of multivesicular release and release of single vesicles does not saturate all postsynaptic receptors, which has been a central dogma in systems neuroscience (Silver et al., 2003; Hardingham et al., 2010).

Excitatory cortical synapses are the computational substrate of higher cognitive functions, and especially the latter finding shows that – despite over a century of research – key details about their operation remain elusive. We propose that applying modern super-resolution technologies and optical recording techniques to neocortical synapses will advance our understanding further, for example by revealing a link between multiple release sites per synapse and the molecular nanocolumns as discovered in the hippocampus (Nair et al., 2013; Tang et al., 2016), which could in turn provide further experimental validation for our findings.

In summary, our structure-function data provide the necessary experimental validation that ultrastructural studies at synaptic resolution can inform about the electrophysiological properties of the studied synapses and of the underlying neuronal circuits. Furthermore, we have provided direct experimental evidence that synaptic transmission strength can be predicted from synapse size. This could be an essential step towards assigning functional attributes to structural connectomes.

Combining our findings from both studies allows us to hypothesize that the thalamocortical projection to L4 of M1 probably has a similar driving effect on single neurons in L4 as it has in sensory areas. Despite lower synapse densities and lower absolute synapse numbers, it is likely that single L4 neurons receive similar absolute numbers of thalamocortical synapses in M1 and S1. Furthermore, thalamic synapse sizes in M1 L4 exceeded synapse sizes in S1 L4 and our structure-function project has provided the experimental evidence that this relates to on average stronger EPSPs elicited in M1 L4 compared to S1 L4. However, it is probable that a different conductance state of the neuron *in* vivo (Koch, 2004; Jouhanneau et al., 2015) in combination with the stronger short-term depression of synapses with larger EPSPs (see *Appendix* – Conference abstracts of A. Gastone and M. Buchholz) result in

effectively equal synaptic strength between thalamocortical synapses in M1 L4 and S1 L4 during normal brain activity *in vivo*.

To test this hypothesis and answer the question conclusively of whether the M1 circuitry indeed contains the same canonical circuit motif that was found to be implemented across sensory areas of neocortex, it is necessary to conduct *in vivo* electrophysiological experiments similar to the ones performed by Douglas and Martin in cat V1 (1991).

Appendix

Abstracts of posters presented at national and international conferences

Information transfer between pyramidal neurons is optimized by synaptic background activity and short-term plasticity

A. Gastone Guilabert, B. Ehret, M.O. Buchholz, G.F.P. Schuhknecht

Institute of Neuroinformatics, University of Zurich, ETH Zurich

Winterthurerstrasse 190, 8057 Zurich, Switzerland

Cortical neurons receive thousands of synapses whose excitatory postsynaptic potential (EPSP) amplitudes span an order of magnitude. Most synapses evoke EPSPs below 1 mV; only a small fraction of EPSPs exceed 2 mV. Such 'strong' connections predominantly occur between similarly-tuned neurons that tend to fire in synchrony, and are hypothesized to determine the postsynaptic neuron's response[1]. In this study, we asked how the majority of inputs – having uncorrelated firing and 'weak' synapses – contribute to cortical computation. We performed *in vitro* whole-cell recordings of layer 2/3 (L2/3) pyramids in mouse barrel cortex with extracellular single-fiber stimulation and recorded the distribution of EPSP amplitudes and corresponding short-term plasticity (STP). Using our results and pairwise correlation coefficients found in *in vivo* studies, we modeled a L2/3 pyramid whose presynaptic partners fired at an average 5 Hz. We set 13% of input cells to have strong, depressing synapses and fire with temporal correlation. The majority of inputs were set to have weak synapses with weak STP and fire temporally uncorrelated spikes. We then quantified the ability of presynaptic cells to elicit spikes in the postsynaptic neuron by measuring the mutual information between each input spike train and the postsynaptic response. Our simulations indicated that temporal correlations found *in vivo* maximized synaptic information transfer to 30 bits/s. Notably, the presence of weak, temporally uncorrelated synapses increased information transfer of strong, correlated synapses by a factor of 2. STP contributed as a synaptic mechanism to stabilize firing by preventing strong, depressing synapses from driving the postsynaptic neuron into runaway excitation, indicating that STP acts as a necessary filter to the presynaptic pattern of inputs. Our results show how weak and strong synapses cooperate to shape the firing properties of cortical neurons, and highlight how neurons are intricately fine-tuned to use synaptic background activity and STP for efficient synaptic computation.

References

1. Cossell L, Iacaruso MF, Muir DR, Houlton R, Sader EN, Ko H, Hofer SB, Mrsic-Flogel TD. Functional organization of excitatory synaptic strength in primary visual cortex. Nature. 19 Feb 2015; 518: 399-403.

Society for Neuroscience (SfN), San Diego, USA, November 3 – 7, 2018.

EPSP amplitude predicts synapse size in mouse barrel cortex

Gregor F.P. Schuhknecht, Simone Holler-Rickauer, German Köstinger, Kevan A.C. Martin

Institute of Neuroinformatics, University of Zurich, ETH Zurich

Winterthurerstrasse 190, 8057 Zurich, Switzerland

The field of connectomics is currently subject to great attention and immense research efforts. One of its central promises holds that acquiring the complete wiring diagram of all the neurons and their synaptic connections in a block of the brain using an electron microscope (EM) will ultimately lead to a deep understanding of the embedded neuronal circuits. A serious difficulty is that we do not yet understand how the anatomical features of even a single cortical synapse seen in the EM correlate with its physiological strength. To bridge this gap, we studied the physiology and ultrastructure of the same synapses. First, we recorded pairs of synaptically connected layer 2/3 pyramidal neurons in mouse barrel cortex (at postnatal days 21 to 30) *in vitro* and measured the mean amplitude and variance of the excitatory postsynaptic potentials (EPSPs). The synapses in this study (n = 8 connected pairs) had mean EPSP amplitudes varying between 0.4 mV and 2.3 mV and further analyses indicated that multiple release sites were present. The pre- and postsynaptic neurons were filled with biocytin, which allowed us to identify all putative synaptic contacts between the axon of the presynaptic neuron and the dendrites of the postsynaptic neuron in the light microscope (LM; average of 4.1 contacts per pair). Finally, we performed correlated LM-EM on all contacts seen in LM to test whether these contacts formed synapses. Surprisingly, of the 8 pairs, 6 were connected by only a single anatomical synapse. Two pairs (both of which also had the largest EPSPs) were connected by 2 synapses, each. Significantly, in all cases, the number of physiological release sites exceeded the number of anatomical synapses found in EM. This implies that individual cortical synapses contain multiple transmitter release sites and that release of a single vesicle does not saturate all the postsynaptic receptors. Most previous correlative studies relied on LM and likely overestimated the number of synapses, and so concluded that each synapse contains only a single release site. Importantly for the interpretation of structural connectomes, we found that a synapse's postsynaptic density (PSD) size was strongly correlated with its average evoked EPSP (r = 0.9). This relation could be a key step in giving functional attributes to the structural connectomes of neocortex.

Annual Meeting of Swiss Society for Neuroscience, Zurich, Switzerland, February 9, 2018.

Correlating Structure and Function of Single Excitatory Synapses in Mouse Barrel Cortex*

G.F.P. Schuhknecht, S. Holler-Rickauer, G. Köstinger, K.A.C. Martin

Institute of Neuroinformatics, University of Zurich, ETH Zurich

Winterthurerstrasse 190, 8057 Zurich, Switzerland

The central promise of classical connectomics holds that acquiring the wiring diagram of billions of neurons and trillions of synapses using an electron microscope (EM) will ultimately lead to a deep understanding of brain function. Unfortunately, we do not properly understand how anatomical and physiological features correlate at a single cortical synapse. In particular, the physiological response of a synapse cannot yet be estimated from EM. We combined physiological and structural analyses to tackle this problem. First, we measured synaptic transmission between L2/3 pyramids in mouse barrel cortex using electrophysiology. Quantal analysis suggested that all recorded synapses (n=8) contained multiple release sites. Then, we used light microscopy to identify all putative synaptic contacts between the neurons (av.: 3.8). Finally, we performed EM on all contacts to validate the existence of synapses and measured their structural features. Our EM analysis showed that 7 pairs were connected by a single synapse. This finding implies that single cortical synapses contain multiple transmitter release sites and that the postsynaptic receptors cannot be saturated by a single released vesicle. Most previous studies relied on light microscopy and so mistakenly concluded that each synapse contains only a single release site. Importantly, we did find that a synapse's postsynaptic density (PSD) size was strongly correlated with its average evoked postsynaptic potential (r = 0.97). This potentially provides a convenient and powerful metric for estimating the relative physiological strengths of synapses from their PSD sizes in EM.

---

*Awarded as best poster in Category *Systems and Behavioral Neuroscience*

The distribution of short-term plasticity of intracortical synapses converging onto single layer 2/3 neurons

Moritz O. Buchholz, Gregor F. P. Schuhknecht, Kevan A. C. Martin

Institute of Neuroinformatics, University of Zurich, ETH Zurich

Winterthurerstrasse 190, 8057 Zurich, Switzerland

A neuron's response to presynaptic activity is shaped by the short-term plasticity (STP) at its afferent synapses. Therefore, the distribution of STP of the synapses that converge onto one neuron is of high importance for how input is integrated. To investigate this distribution, we performed whole-cell slice-recordings of neurons in layer 2/3 (L2/3) of barrel cortex and measured the STP responses for multiple synapses per cell following extracellular paired-pulse stimulation at different locations in L2/3. In total, we recorded from 94 synapses onto 26 different neurons in 13 mice. The EPSP amplitudes of these 94 synapses had a mean of 1.27 ± 0.75 mV and followed a lognormal distribution. Interestingly, for stimulation with a paired-pulse interval of 20 ms, the paired-pulse ratios (PPR) of the recorded synapses followed a normal distribution with a mean of 0.92 ± 0.21. For 10 neurons, we obtained measurements of at least 5 different synapses each. Strikingly, the distributions of PPR for any of these neurons was never significantly different from the overall PPR distribution in L2/3. We conclude that the STPs of synapses converging onto a single L2/3 neuron can be well described and modeled with a normal distribution with a mean of 0.92 ± 0.21.

An ultrastructural study of the thalamic input to layers 4 of motor and somatosensory cortex in the mouse

G.F.P. Schuhknecht, R. Bopp, S. Holler-Rickauer, K.A.C. Martin

Institute of Neuroinformatics, University of Zurich, ETH Zurich

Winterthurerstrasse 190, 8057 Zurich, Switzerland

The primary motor cortex (M1) is traditionally thought to lack the granular layer 4 (L4), which is the principal target for thalamic input in sensory areas, suggesting the local circuits are organized differently in M1. Recent physiological evidence that M1 possesses a thin thalamo-recipient middle layer has inspired the speculation that motor cortex is actually similar to sensory cortex. Whether important anatomical features, such as the proportion of synapses formed by the thalamus in L4 of M1 versus barrel cortex (S1), are unknown. We used the vesicular glutamate transporter 2 (VGluT2) as a reliable and exclusive marker of thalamic presynaptic boutons. We discovered significant differences between M1 and S1. By unbiased dissector counts of labeled profiles in EM, we found that the thalamus contributes about twice as many synapses to the local circuitry in L4 of S1 compared to M1. Strikingly, thalamic boutons innervated almost exclusively spines (i.e. pyramidal cells) in M1, while in S1 9% of thalamic synapses targeted smooth dendrites of putative GABAergic neurons. After reconstructing a number of VGluT2$^+$ boutons in 3D we discovered further differences: on average, labeled boutons in S1 were larger than in M1 (0.31 μm^3 vs. 0.20 μm^3), formed more synapses per bouton (2.1 vs. 1.3), while postsynaptic densities were larger in M1 (0.052 μm^2 vs. 0.078 μm^2). Our data indicate that while the motor cortex possesses a canonical pattern of thalamic innervation, the thalamic input to M1 likely plays a role in cortical processing that is different to sensory areas.

An ultrastructural study of the thalamic input to layers 4 of motor and somatosensory cortex in the mouse

Gregor FP Schuhknecht, Rita Bopp, Simone Holler-Rickauer, Kevan AC Martin

Institute of Neuroinformatics, University of Zurich, ETH Zurich

Winterthurerstrasse 190, 8057 Zurich, Switzerland

The primary motor cortex (M1) is traditionally thought to lack the granular layer 4 (L4), which is the principal target for thalamic input in sensory areas, suggesting the local circuits are organized differently in M1. Recent physiological evidence that M1 possesses a thin thalamo-recipient middle layer has led to the speculation that motor cortex is in fact similar to sensory cortex. Whether important anatomical features, such as the proportion of synapses formed by the thalamus in L4 of M1 versus barrel cortex (S1), are not known. Here we used the vesicular glutamate transporter 2 (VGluT2) as a reliable and exclusive marker of thalamic presynaptic boutons. We discovered significant differences between M1 and S1. By unbiased dissector counts of labeled profiles in EM, we found that the thalamus contributes about twice as many synapses to the local circuitry in L4 of S1 compared to M1. Strikingly, thalamic boutons formed synapses almost exclusively with spines (i.e. pyramidal cells) in M1, while in S1 9% of thalamic synapses targeted smooth dendrites of putative GABAergic neurons. After reconstructing a number of VGluT2^{+} boutons in 3D we discovered further differences: labeled boutons in S1 were larger than in M1 ($\bar{x}$ = 0.31 μm^3 vs. 0.20 μm^3), formed more synapses per bouton ($\bar{x}$ = 2.1 vs. 1.3), while postsynaptic densities were larger in M1 ($\bar{x}$ = 0.052 μm^2 vs. 0.078 μm^2). Our data indicate that while the motor cortex possesses a canonical pattern of thalamic innervation, the thalamic input to M1 likely plays a role in cortical processing that is different to the sensory areas.

Thalamic input to the primary motor cortex in the mouse has a canonical pattern and weight

G.F.P. Schuhknecht, R. Bopp, K.A.C. Martin

Institute of Neuroinformatics, University of Zurich, ETH Zurich

Winterthurerstrasse 190, 8057 Zurich, Switzerland

A defining feature of the neocortex is its 6 layers, which are thought to arise from the organization of canonical circuits that are present in all cortical areas. Motor cortex (M1), however, seems to violate this definition, because it appears to lack a granular layer 4 (L4), which is a principal target for thalamic input in sensory areas. From this striking difference in cytoarchitecture one might suppose that the local circuits in M1 and their operation are quite different to those in sensory areas. To investigate the apparent lack of a thalamic recipient zone in the middle layers, we made a qualitative and quantitative analysis of the thalamic input to M1 in the mouse. We injected the anterograde tracer biotinylated dextran amine (BDA) into the motor thalamus (n = 9 mice, under general anaesthesia, permission of Zurich Veterinäramt) and observed the same core and matrix pattern of cortical innervation that is evident in sensory cortex, including a distinct band in a region we could identify as putative L4. We then quantified the proportion of synapses formed by the thalamus within all asymmetric synapses in L4 of M1 and barrel cortex (S1BF) by immunostaining for the vesicular glutamate transporter 2 (VGluT2), a reliable and exclusive marker of thalamic terminals. The pattern of VGluT2 staining resembled that of the adjacent S1BF, albeit with a thinner L4. By unbiased dissector counts of labeled profiles seen in EM, we found that the proportion of thalamic synapses in the neuropil of M1 ($\approx$11.4%) was of the same order of magnitude as that of L4 in S1BF ($\approx$16.6%) (n = 3 mice). Our new data indicate that the primary motor cortex possesses a canonical pattern of thalamic innervation. Its lack of a granular layer may thus be more a reflection of the size of the postsynaptic neurons in L4 of M1 than any fundamental difference in its circuits.

Matlab and Python code

This disk contains the code that was developed and used for the analysis of EPSP amplitudes and kinetics, the code for SMAQ and the associated statistical tests, and the Python code that was used to run the NEURON model of the L2/3 pyramidal cell.

Bibliography

Agmon A, O'Dowd DK (1992) NMDA receptor-mediated currents are prominent in the thalamocortical synaptic response before maturation of inhibition. J Neurophysiol 68:345–349.

Ahmed B, Anderson JC, Douglas RJ, Martin KAC, Nelson JC (1994) Polyneuronal innervation of spiny stellate neurons in cat visual cortex. J Comp Neurol 341:39–49.

Ahmed B, Anderson JC, Martin KAC, Nelson JC (1997) Map of the synapses onto layer 4 basket cells of the primary visual cortex of the cat. J Comp Neurol 380:230–242.

Anderson JC, Binzegger T, Martin K, Rockland KS (1998) The connection from cortical area V1 to V5: a light and electron microscopic study. J Neurosci 18:10525–10540.

Anderson JC, Kennedy H, Martin KAC (2011) Pathways of attention: synaptic relationships of frontal eye field to V4, lateral intraparietal cortex, and area 46 in macaque monkey. J Neurosci 31:10872–10881.

Anderson JC, Martin KAC (2002) Connection from cortical area V2 to MT in macaque monkey. J Comp Neurol 443:56–70.

Anderson JC, Martin KAC (2005) Connection from cortical area V2 to V3A in macaque monkey. J Comp Neurol 488:320–330.

Anderson JC, Martin KAC (2006) Synaptic connection from cortical area V4 to V2 in macaque monkey. J Comp Neurol 495:709–721.

Anderson JC, Martin KAC (2009) The synaptic connections between cortical areas V1 and V2 in macaque monkey. J Neurosci 29:11283–11293.

Anderson JC, Martin KAC (2016) Chapter 6 - Interareal connections of the macaque cortex: how neocortex talks to itself. In: Axons and brain architecture (Rockland KS, ed), pp 117–134. San Diego: Academic Press.

Andrásfalvy BK, Magee JC (2001) Distance-dependent increase in AMPA receptor number in the dendrites of adult hippocampal CA1 pyramidal neurons. J Neurosci 21:9151–9159.

Arellano JI, Benavides-Piccione R, DeFelipe J, Yuste R (2007) Ultrastructure of dendritic spines: correlation between synaptic and spine morphologies. Front Neurosci 1:131–143.

Artola A, Singer W (1987) Long-term potentiation and NMDA receptors in rat visual cortex. Nature 330:649–652.

Banitt Y, Martin KAC, Segev I (2007) A biologically realistic model of contrast invariant orientation tuning by thalamocortical synaptic depression. J Neurosci 27:10230–10239.

Bannister NJ, Nelson JC, Jack JJB (2002) Excitatory inputs to spiny cells in layers 4 and 6 of cat striate cortex. Philos Trans R Soc Lond B Biol Sci 357:1793–1808.

Barbas H, García-Cabezas MÁ (2015) Motor cortex layer 4: less is more. Trends Neurosci 38:259–261.

Bartol TM, Bromer C, Kinney J, Chirillo MA, Bourne JN, Harris KM, Sejnowski TJ (2016) Nanoconnectomic upper bound on the variability of synaptic plasticity. eLife 4:e10778.

Bastos AM, Usrey WM, Adams RA, Mangun GR, Fries P, Friston KJ (2012) Canonical microcircuits for predictive coding. Neuron 76:695–711.

Bernander O, Douglas RJ, Martin KAC, Koch C (1991) Synaptic background activity influences spatiotemporal integration in single pyramidal cells. PNAS 88:11569–11573.

Betz W (1874) Anatomischer Nachweis zweier Gehirncentra. Centralblatt für die medizinischen Wissenschaften 12:195–599.

Biró ÁA, Holderith NB, Nusser Z (2005) Quantal size is independent of the release probability at hippocampal excitatory synapses. J Neurosci 25:223–232.

Bopp R, Holler-Rickauer S, Martin KAC, Schuhknecht GFP (2017) An ultrastructural study of the thalamic input to layer 4 of primary motor and primary somatosensory cortex in the mouse. J Neurosci 37:2435–2448.

Branco T, Staras K (2009) The probability of neurotransmitter release: variability and feedback control at single synapses. Nat Rev Neurosci 10:373–383.

Brémaud A, West DC, Thomson AM (2007) Binomial parameters differ across neocortical layers and with different classes of connections in adult rat and cat neocortex. PNAS 104:14134–14139.

Broca P (1861) Remarks on the seat of the faculty of articulated language, following an observation of aphemia (loss of speech). Bulletin de la Société Anatomique 6:330–57.

Brodmann K (1909) Vergleichende Lokalisationslehre der Großhirnrinde. Barth.

Bruno RM, Sakmann B (2006) Cortex is driven by weak but synchronously active thalamocortical synapses. Science 312:1622–1627.

Buhl E H, Tamás G, Szilágyi T, Stricker C, Paulsen O, Somogyi P (1997) Effect, number and location of synapses made by single pyramidal cells onto aspiny interneurones of cat visual cortex. J Physiol 500:689–713.

Büttner U, Büttner-Ennever JA (2006) Present concepts of oculomotor organization. In: Progress in Brain Research (Büttner-Ennever JA, ed), pp 1–42 Neuroanatomy of the Oculomotor System. Elsevier.

Canepari M, Vogt K, Zecevic D (2008) Combining voltage and calcium imaging from neuronal dendrites. Cell Mol Neurobiol 28:1079.

Casas-Torremocha D, Porrero C, Rodriguez-Moreno J, García-Amado M, Lübke JHR, Núñez Á, Clascá F (2019) Posterior thalamic nucleus axon terminals have different structure and functional impact in the motor and somatosensory vibrissal cortices. Brain Struct Funct 224:1627–1645.

Christie JM, Jahr CE (2006) Multivesicular release at Schaffer collateral–CA1 hippocampal synapses. J Neurosci 26:210–216.

Clements J (1991) Quantal synaptic transmission? Nature 353:396–396.

Colonnier M (1968) Synaptic patterns on different cell types in the different laminae of the cat visual cortex. An electron microscope study. Brain Res 9:268–287.

Cragg BG (1967) The density of synapses and neurones in the motor and visual areas of the cerebral cortex. J Anat 101:639–654.

Czeiger D, White EL (1993) Synapses of extrinsic and intrinsic origin made by callosal projection neurons in mouse visual cortex. J Comp Neurol 330:502–513.

da Costa NM, Martin KAC (2009) The proportion of synapses formed by the axons of the lateral geniculate nucleus in layer 4 of area 17 of the cat. J Comp Neurol 516:264–276.

da Costa NM, Martin KAC (2011) How thalamus connects to spiny stellate cells in the cat's visual cortex. J Neurosci 31:2925–2937.

DeFelipe J, Swanson L (2017) The beautiful brain: the drawings of Ramón y Cajal, 1st ed. New York: Abrams & Chronicle Books.

del Castillo J, Katz B (1954a) Statistical factors involved in neuromuscular facilitation and depression. J Physiol 124:574–585.

del Castillo J, Katz B (1954b) Quantal components of the end-plate potential. J Physiol 124:560–573.

Dityatev AE, Clamann HP (1998) Synaptic differentiation of single descending fibers studied by triple intracellular recording in the frog spinal cord. J Neurophysiol 79:763–768.

Douglas RJ, Koch C, Mahowald M, Martin KAC, Suarez HH (1995) Recurrent excitation in neocortical circuits. Science 269:981–985.

Douglas RJ, Martin KAC (1991) A functional microcircuit for cat visual cortex. J Physiol 440:735–769.

Douglas RJ, Martin KAC (2004) Neuronal circuits of the neocortex. Annu Rev Neurosci 27:419–451.

Douglas RJ, Martin KAC (2007) The butterfly and the loom. Brain Research Reviews 55:314–328.

Douglas RJ, Martin KAC (2012) Behavioral architecture of the cortical sheet. Curr Biol 22:R1033–R1038.

Douglas RJ, Martin KAC, Whitteridge D (1989) A canonical microcircuit for neocortex. Neural Computation 1:480–488.

Eccles JC (1982) The synapse: from electrical to chemical transmission. Annu Rev Neurosci 5:325–339.

Ellis-Davies GCR (2007) Caged compounds: photorelease technology for control of cellular chemistry and physiology. Nat Methods 4:619–628.

Ellis-Davies GCR (2019) Two-photon uncaging of glutamate. Front Synaptic Neurosci 10.

Engert F, Bonhoeffer T (1999) Dendritic spine changes associated with hippocampal long-term synaptic plasticity. Nature 399:66–70.

Fatt P, Katz B (1950) Some observations on biological noise. Nature 166:597–598.

Fatt P, Katz B (1951) An analysis of the end-plate potential recorded with an intra-cellular electrode. J Physiol 115:320–370.

Fatt P, Katz B (1952) Spontaneous subthreshold activity at motor nerve endings. J Physiol 117:109–128.

Feldmeyer D, Egger V, Lübke J, Sakmann B (1999) Reliable synaptic connections between pairs of excitatory layer 4 neurones within a single 'barrel' of developing rat somatosensory cortex. J Physiol 521:169–190.

Feldmeyer D, Lübke J, Sakmann B (2006) Efficacy and connectivity of intracolumnar pairs of layer 2/3 pyramidal cells in the barrel cortex of juvenile rats. J Physiol 575:583–602.

Feldmeyer D, Lübke J, Silver RA, Sakmann B (2002) Synaptic connections between layer 4 spiny neurone- layer 2/3 pyramidal cell pairs in juvenile rat barrel cortex: physiology and anatomy of interlaminar signalling within a cortical column. J Physiol 538:803–822.

Ferrier D (1874) Experiments on the brain of monkeys—No. I. Proc R Soc Lond 23:409–430.

Ferster D, LeVay S (1978) The axonal arborizations of lateral geniculate neurons in the striate cortex of the cat. J Comp Neurol 182:923–944.

Ferster D, Lindström S (1983) An intracellular analysis of geniculo-cortical connectivity in area 17 of the cat. J Physiol 342:181–215.

Foster M, Sherrington CS (1897) A textbook of physiology. London: Macmillan.

Franks KM, Bartol TM, Sejnowski TJ (2002) A Monte Carlo model reveals independent signaling at central glutamatergic synapses. Biophys J 83:2333–2348.

Franks KM, Stevens CF, Sejnowski TJ (2003) Independent sources of quantal variability at single glutamatergic synapses. J Neurosci 23:3186–3195.

Freund TF, Martin KAC, Whitteridge D (1985) Innervation of cat visual areas 17 and 18 by physiologically identified X-and Y-type thalamic afferents. I. Arborization patterns and quantitative distribution of postsynaptic elements. J Comp Neurol 242:263–274.

Fritsch G, Hitzig E (1870) Über die elektrische Erregbarkeit des Grosshirns. Arch, Anat Physiol Wiss Med 37.

Fukata Y, Dimitrov A, Boncompain G, Vielemeyer O, Perez F, Fukata M (2013) Local palmitoylation cycles define activity-regulated postsynaptic subdomains. J Cell Biol 202:145–161.

García-Cabezas MÁ, Barbas H (2014) Area 4 has layer IV in adult primates. Eur J Neurosci 39:1824–1834.

Geiger JRP, Melcher T, Koh D-S, Sakmann B, Seeburg PH, Jonas P, Monyer H (1995) Relative abundance of subunit mRNAs determines gating and Ca2+ permeability of AMPA receptors in principal neurons and interneurons in rat CNS. Neuron 15:193–204.

Gest H (2004) The discovery of microorganisms by Robert Hooke and Antoni van Leeuwenhoek, fellows of The Royal Society. Notes and Records of the Royal Society of London 58:187–201.

Gil Z, Connors BW, Amitai Y (1999) Efficacy of thalamocortical and intracortical synaptic connections: quanta, innervation, and reliability. Neuron 23:385–397.

Glenn Northcutt R, Kaas JH (1995) The emergence and evolution of mammalian neocortex. Trends Neurosci 18:373–379.

Granit R (1966) Charles Scott Sherrington: an appraisal. Nelson.

Gray EG (1959) Axo-somatic and axo-dendritic synapses of the cerebral cortex. J Anat 93:420–433.

Graziano MSA (2015) Ethological action maps: a paradigm shift for the motor cortex. Trends Cogn Sci.

Graziano MSA, Taylor CSR, Moore T (2002a) Complex movements evoked by microstimulation of precentral cortex. Neuron 34:841–851.

Graziano MSA, Taylor CSR, Moore T, Cooke DF (2002b) The cortical control of movement revisited. Neuron 36:349–362.

Gross CG (2007) The discovery of motor cortex and its background. Journal of the History of the Neurosciences 16:320–331.

Gulyás AI, Miles R, Sik A, Tóth K, Tamamaki N, Freund TF (1993) Hippocampal pyramidal cells excite inhibitory neurons through a single release site. Nature 366:683–687.

Guzman SJ, Schlögl A, Schmidt-Hieber C (2014) Stimfit: quantifying electrophysiological data with Python. Front Neuroinform 8:16.

Haas KT, Compans B, Letellier M, Bartol TM, Grillo-Bosch D, Sejnowski TJ, Sainlos M, Choquet D, Thoumine O, Hosy E (2018) Pre-post synaptic alignment through neuroligin-1 tunes synaptic transmission efficiency. eLife 7:e31755.

Hannay T, Larkman A, Stratford K, Jack JJB (1993) A common rule governs the synaptic locus of both short-term and long-term potentiation. Curr Biol 3:832–841.

Hardingham NR, Bannister NJ, Read JCA, Fox KD, Hardingham GE, Jack JJB (2006) Extracellular calcium regulates postsynaptic efficacy through group 1 metabotropic glutamate receptors. J Neurosci 26:6337–6345.

Hardingham NR, Hardingham GE, Fox KD, Jack JJB (2007) Presynaptic efficacy directs normalization of synaptic strength in layer 2/3 rat neocortex after paired activity. J Neurophysiol 97:2965–2975.

Hardingham NR, Read JCA, Trevelyan AJ, Nelson JC, Jack JJB, Bannister NJ (2010) Quantal analysis reveals a functional correlation between presynaptic and postsynaptic efficacy in excitatory connections from rat neocortex. J Neurosci 30:1441–1451.

Harris KM, Stevens JK (1989) Dendritic spines of CA 1 pyramidal cells in the rat hippocampus: serial electron microscopy with reference to their biophysical characteristics. J Neurosci 9:2982–2997.

Hayashi Y, Shi S-H, Esteban JA, Piccini A, Poncer J-C, Malinow R (2000) Driving AMPA receptors into synapses by LTP and CaMKII: requirement for GluR1 and PDZ domain interaction. Science 287:2262–2267.

Herculano-Houzel S (2009) The human brain in numbers: a linearly scaled-up primate brain. Front Hum Neurosci 3:1–11.

Hestrin S, Sah P, Nicoll RA (1990) Mechanisms generating the time course of dual component excitatory synaptic currents recorded in hippocampal slices. Neuron 5:247–253.

Holderith N, Lorincz A, Katona G, Rózsa B, Kulik A, Watanabe M, Nusser Z (2012) Release probability of hippocampal glutamatergic terminals scales with the size of the active zone. Nat Neurosci 15:988–997.

Hooke R (1664) Micrographia, or, some physiological descriptions of minute bodies made by magnifying glasses: with observations and inquiries thereupon. Council of the Royal Society of London for Improving of Natural Knowledge.

Hubel DH, Wiesel TN (1959) Receptive fields of single neurones in the cat's striate cortex. J Physiol 148:574–591.

Hubel DH, Wiesel TN (1962) Receptive fields, binocular interaction and functional architecture in the cat's visual cortex. J Physiol 160:106–154.

Hubel DH, Wiesel TN (1968) Receptive fields and functional architecture of monkey striate cortex. J Physiol 195:215–243.

Hubel DH, Wiesel TN (1969) Anatomical demonstration of columns in the monkey striate cortex. Nature 221:747–750.

Hubel DH, Wiesel TN (1998) Early exploration of the visual cortex. Neuron 20:401–412.

Hull C, Isaacson JS, Scanziani M (2009) Postsynaptic mechanisms govern the differential excitation of cortical neurons by thalamic inputs. J Neurosci 29:9127–9136.

Humphrey AL, Sur M, Uhlrich DJ, Sherman SM (1985) Projection patterns of individual X-and Y-cell axons from the lateral geniculate nucleus to cortical area 17 in the cat. J Comp Neurol 233:159–189.

Jack JJB, Kullmann DM, Larkman AU, Major G, Stratford KJ (1990) Quantal analysis of excitatory synaptic mechanisms in the mammalian central nervous system. Cold Spring Harb Symp Quant Biol 55:57–67.

Jack JJB, Larkman AU, Major G, Stratford KJ (1994) Quantal analysis of the synaptic excitation of CA1 hippocampal pyramidal cells. Adv Second Messenger Phosphoprotein Res 29:275–299.

Johnson RR, Burkhalter A (1996) Microcircuitry of forward and feedback connections within rat visual cortex. J Comp Neurol 368:383–398.

Jones EG (1994) The neuron doctrine 1891. Journal of the History of the Neurosciences 3:3–20.

Jones EG (2012) The thalamus. Springer Science & Business Media.

Jones EG, Powell TPS (1970) An electron microscopic study of the laminar pattern and mode of termination of afferent fibre pathways in the somatic sensory cortex of the cat. Philos Trans R Soc Lond B Biol Sci 257:45–62.

Jouhanneau J-S, Kremkow J, Dorrn AL, Poulet JFA (2015) In vivo monosynaptic excitatory transmission between layer 2 cortical pyramidal neurons. Cell Reports 13:2098–2106.

Kaas JH (2006) Evolution of the neocortex. Curr Biol 16:R910–R914.

Kandel ER, Schwartz JH, Jessell TM (2000) Principles of neural science, 4th revised edition. New York, NY: McGraw-Hill Professional.

Kasthuri N et al. (2015) Saturated reconstruction of a volume of neocortex. Cell 162:648–661.

Kato N, Artola A, Singer W (1991) Developmental changes in the susceptibility to long-term potentiation of neurones in rat visual cortex slices. Dev Brain Res 60:43–50.

Kawai R, Markman T, Poddar R, Ko R, Fantana AL, Dhawale AK, Kampff AR, Ölveczky BP (2015) Motor cortex is required for learning but not for executing a motor skill. Neuron 86:800–812.

Keller D, Erö C, Markram H (2018) Cell densities in the mouse brain: a systematic review. Front Neuroanat 12.

Koch C (2004) Biophysics of computation: information processing in single neurons. Oxford University Press.

Koester HJ, Johnston D (2005) Target cell-dependent normalization of transmitter release at neocortical synapses. Science 308:863–866.

Koestinger G, Martin KAC, Roth S, Rusch ES (2017) Synaptic connections formed by patchy projections of pyramidal cells in the superficial layers of cat visual cortex. Brain Struct Funct 222:3025–3042.

Kondo M, Sumino R, Okado H (1997) Combinations of AMPA receptor subunit expression in individual cortical neurons correlate with expression of specific calcium-binding proteins. J Neurosci 17:1570–1581.

Korn H, Faber DS (1991) Quantal analysis and synaptic efficacy in the CNS. Trends Neurosci 14:439–445.

Korn H, Triller A, Mallet A, Faber DS (1981) Fluctuating responses at a central synapse: n of binomial fit predicts number of stained presynaptic boutons. Science 213:898–901.

Krieg WJ (1946) Connections of the cerebral cortex. I. The albino rat. B. Structure of the cortical areas. J Comp Neurol 84:277–323.

Kuffler SW (1953) Discharge patterns and functional organization of mammalian retina. J Neurophysiol 16:37–68.

Kumar P, Ohana O (2008) Inter- and intralaminar subcircuits of excitatory and inhibitory neurons in layer 6a of the rat barrel cortex. J Neurophysiol 100:1909–1922.

Kuramoto E, Furuta T, Nakamura KC, Unzai T, Hioki H, Kaneko T (2009) Two types of thalamocortical projections from the motor thalamic nuclei of the rat: a single neuron-tracing study using viral vectors. Cereb Cortex 19:2065–2077.

Kuramoto E, Ohno S, Furuta T, Unzai T, Tanaka YR, Hioki H, Kaneko T (2013) Ventral medial nucleus neurons send thalamocortical afferents more widely and more preferentially to layer 1 than neurons of the ventral anterior–ventral lateral nuclear complex in the rat. Cereb Cortex 25:221–235.

Kuypers H (1981) Anatomy of the descending pathways. In: Handbook of physiology, section I. The nervous system, pp. 597-667. American Physiological Society, Bethesda, MD., pp 597–666.

Larkman AU, Hannay T, Stratford K, Jack JJB (1992) Presynaptic release probability influences the locus of long-term potentiation. Nature 360:70–73.

Larkman AU, Jack JJB, Stratford KJ (1997) Quantal analysis of excitatory synapses in rat hippocampal CA1 In vitro during low-frequency depression. J Physiol 505:457–471.

Latawiec D, Martin KAC, Meskenaite V (2000) Termination of the geniculocortical projection in the striate cortex of macaque monkey: a quantitative immunoelectron microscopic study. J Comp Neurol 419:306–319.

Lee CC, Sherman SM (2008) Synaptic properties of thalamic and intracortical inputs to layer 4 of the first- and higher-order cortical areas in the auditory and somatosensory systems. J Neurophysiol 100:317–326.

Lee TS, Mumford D (2003) Hierarchical Bayesian inference in the visual cortex. J Opt Soc Am A, JOSAA 20:1434–1448.

LeVay S, Gilbert CD (1976) Laminar patterns of geniculocortical projection in the cat. Brain Res 113:1–19.

Lim R, Alvarez FJ, Walmsley B (1999) Quantal size is correlated with receptor cluster area at glycinergic synapses in the rat brainstem. J Physiol 516:505–512.

Loebel A (2009) Multiquantal release underlies the distribution of synaptic efficacies in the neocortex. Front Comput Neurosci 3.

Lübke J, Egger V, Sakmann B, Feldmeyer D (2000) Columnar organization of dendrites and axons of single and synaptically coupled excitatory spiny neurons in layer 4 of the rat barrel cortex. J Neurosci 20:5300–5311.

Lübke J, Roth A, Feldmeyer D, Sakmann B (2003) Morphometric analysis of the columnar innervation domain of neurons connecting layer 4 and layer 2/3 of juvenile rat barrel cortex. Cereb Cortex 13:1051–1063.

Luhmann HJ, Prince DA (1991) Postnatal maturation of the GABAergic system in rat neocortex. J Neurophysiol 65:247–263.

MacGillavry HD, Song Y, Raghavachari S, Blanpied TA (2013) Nanoscale scaffolding domains within the postsynaptic density concentrate synaptic AMPA receptors. Neuron 78:615–622.

Markram H, Lübke J, Frotscher M, Roth A, Sakmann B (1997) Physiology and anatomy of synaptic connections between thick tufted pyramidal neurones in the developing rat neocortex. J Physiol 500:409–440.

Martin KAC, Whitteridge D (1984) Form, function and intracortical projections of spiny neurones in the striate visual cortex of the cat. J Physiol 353:463–504.

Matyas F, Sreenivasan V, Marbach F, Wacongne C, Barsy B, Mateo C, Aronoff R, Petersen CCH (2010) Motor control by sensory cortex. Science 330:1240–1243.

Matz J, Gilyan A, Kolar A, McCarvill T, Krueger SR (2010) Rapid structural alterations of the active zone lead to sustained changes in neurotransmitter release. PNAS 107:8836–8841.

Meyer HS, Wimmer VC, Oberlaender M, de Kock CPJ, Sakmann B, Helmstaedter M (2010) Number and laminar distribution of neurons in a thalamocortical projection column of rat vibrissal cortex. Cereb Cortex 20:2277–2286.

Minkowski M (1913) Experimentelle Untersuchungen über die Beziehungen der Grosshirnrinde und der Netzhaut zu den primären optischen Zentren, besonders zum Corpus geniculatum externum. Springer-Verlag.

Mishchenko Y, Hu T, Spacek J, Mendenhall J, Harris KM, Chklovskii DB (2010) Ultrastructural analysis of hippocampal neuropil from the connectomics perspective. Neuron 67:1009–1020.

Motta A, Berning M, Boergens KM, Staffler B, Beining M, Loomba S, Schramm C, Hennig P, Wissler H, Helmstaedter M (2018) Dense connectomic reconstruction in layer 4 of the somatosensory cortex. bioRxiv:460618.

Mumford D (1992) On the computational architecture of the neocortex. Biol Cybern 66:241–251.

Murthy VN, Schikorski T, Stevens CF, Zhu Y (2001) Inactivity produces increases in neurotransmitter release and synapse size. Neuron 32:673–682.

Nair D, Hosy E, Petersen JD, Constals A, Giannone G, Choquet D, Sibarita J-B (2013) Super-resolution imaging reveals that AMPA receptors inside synapses are dynamically organized in nanodomains regulated by PSD95. J Neurosci 33:13204–13224.

Nicholson DA, Trana R, Katz Y, Kath WL, Spruston N, Geinisman Y (2006) Distance-dependent differences in synapse number and AMPA receptor expression in hippocampal CA1 pyramidal neurons. Neuron 50:431–442.

Nimchinsky EA, Yasuda R, Oertner TG, Svoboda K (2004) The number of glutamate receptors opened by synaptic stimulation in single hippocampal spines. J Neurosci 24:2054–2064.

Nusser Z, Lujan R, Laube G, Roberts JDB, Molnar E, Somogyi P (1998) Cell type and pathway dependence of synaptic AMPA receptor number and variability in the hippocampus. Neuron 21:545–559.

Oertner TG, Sabatini BL, Nimchinsky EA, Svoboda K (2002) Facilitation at single synapses probed with optical quantal analysis. Nat Neurosci 5:657–664.

Ohana O, Portner H, Martin KAC (2012) Fast recruitment of recurrent inhibition in the cat visual cortex. PLoS ONE 7:e40601.

Palay SL, Palade GE (1955) The fine structure of neurons. J Biophys Biochem Cytol 1:69–88.

Peters A, Palay SL (1996) The morphology of synapses. J Neurocytol 25:687–700.

Peters A, Palay SL, others (1991) The fine structure of the nervous system: neurons and their supporting cells. Oxford University Press, USA.

Poljak S (1927) An experimental study of the association callosal, and projection fibers of the cerebral cortex of the cat. J Comp Neurol 44:197–258.

Prange O, Murphy TH (1999) Analysis of multiquantal transmitter release from single cultured cortical neuron terminals. J Neurophysiol 81:1810–1817.

Raghavachari S, Lisman JE (2004) Properties of quantal transmission at CA1 synapses. J Neurophysiol 92:2456–2467.

Ramón y Cajal S (1899) Estudios sobre la corteza cerebral humana. II. Estructura de la corteza motriz del hombre y mamíferos superiores. Revista Trimestral Micrográfica 4:117–200.

Ramón y Cajal S (1937) Recollections of my life. (Trans by E Horne Craigie and J Cano) The American Philosophical Society.

Rao RPN, Ballard DH (1999) Predictive coding in the visual cortex: a functional interpretation of some extra-classical receptive-field effects. Nat Neurosci 2:79–87.

Rathelot J-A, Strick PL (2006) Muscle representation in the macaque motor cortex: An anatomical perspective. PNAS 103:8257–8262.

Rathelot J-A, Strick PL (2009) Subdivisions of primary motor cortex based on cortico-motoneuronal cells. PNAS 106:918–923.

Redman S (1990) Quantal analysis of synaptic potentials in neurons of the central nervous system. Physiol Rev 70:165–198.

Reimann MW, King JG, Muller EB, Ramaswamy S, Markram H (2015) An algorithm to predict the connectome of neural microcircuits. Front Comput Neurosci 9.

Robertis EDPD, Bennett HS (1955) Some features of the submicroscopic morphology of synapses in frog and earthworm. J Cell Biol 1:47–58.

Rollenhagen A, Klook K, Sätzler K, Qi G, Anstötz M, Feldmeyer D, Lübke JHR (2014) Structural determinants underlying the high efficacy of synaptic transmission and plasticity at synaptic boutons in layer 4 of the adult rat 'barrel cortex.' Brain Struct Funct 220:3185–3209.

Rollenhagen A, Lübke JHR (2006) The morphology of excitatory central synapses: from structure to function. Cell Tissue Res 326:221–237.

Rollenhagen A, Ohana O, Sätzler K, Hilgetag CC, Kuhl D, Lübke JHR (2018) Structural properties of synaptic transmission and temporal dynamics at excitatory layer 5B synapses in the adult rat somatosensory cortex. Front Synaptic Neurosci 10.

Rosenmund C, Stern-Bach Y, Stevens CF (1998) The tetrameric structure of a glutamate receptor channel. Science 280:1596–1599.

Sakaba T, Schneggenburger R, Neher E (2002) Estimation of quantal parameters at the calyx of Held synapse. Neuroscience Research 44:343–356.

Sarid L, Bruno R, Sakmann B, Segev I, Feldmeyer D (2007) Modeling a layer 4-to-layer 2/3 module of a single column in rat neocortex: interweaving in vitro and in vivo experimental observations. PNAS 104:16353–16358.

Sarid L, Feldmeyer D, Gidon A, Sakmann B, Segev I (2015) Contribution of intracolumnar layer 2/3-to-layer 2/3 excitatory connections in shaping the response to whisker deflection in rat barrel cortex. Cereb Cortex 25:849–858.

Schikorski T, Stevens CF (1997) Quantitative ultrastructural analysis of hippocampal excitatory synapses. J Neurosci 17:5858–5867.

Schikorski T, Stevens CF (1999) Quantitative fine-structural analysis of olfactory cortical synapses. PNAS 96:4107–4112.

Schoonover CE, Tapia J-C, Schilling VC, Wimmer V, Blazeski R, Zhang W, Mason CA, Bruno RM (2014) Comparative strength and dendritic organization of thalamocortical and corticocortical synapses onto excitatory layer 4 neurons. J Neurosci 34:6746–6758.

Schüz A, Palm G (1989) Density of neurons and synapses in the cerebral cortex of the mouse. J Comp Neurol 286:442–455.

Schwann T (1839) Mikroskopische Untersuchungen über die Uebereinstimmung in der Struktur und dem Wachsthum der Thiere und Pflanzen. Verlag der Sander'schen Buchhandlung (GE Reimer).

Seeman SC et al. (2018) Sparse recurrent excitatory connectivity in the microcircuit of the adult mouse and human cortex. Elife 7:e37349.

Shepherd GMG (2009) Intracortical cartography in an agranular area. Front Neurosci 3:337–343.

Sherrington CS (1906) The integrative action of the nervous system. Yale Univ. Press, New Haven, CT.

Sherrington CS (1908a) Some comparisons between reflex inhibition and reflex excitation. Q J Exp Psychol 1:67–78.

Sherrington CS (1908b) Reciprocal innervation of antagonistic muscles. Thirteenth note. - On the antagonism between reflex inhibition and reflex excitation. Proc R Soc Lond B 80:565–578.

Shi S-H, Hayashi Y, Esteban JA, Malinow R (2001) Subunit-specific rules governing AMPA receptor trafficking to synapses in hippocampal pyramidal neurons. Cell 105:331–343.

Shi S-H, Hayashi Y, Petralia RS, Zaman SH, Wenthold RJ, Svoboda K, Malinow R (1999) Rapid spine delivery and redistribution of AMPA receptors after synaptic NMDA receptor activation. Science 284:1811–1816.

Shipp S (2005) The importance of being agranular: a comparative account of visual and motor cortex. Philos Trans R Soc Lond B Biol Sci 360:797–814.

Shipp S, Adams RA, Friston KJ (2013) Reflections on agranular architecture: predictive coding in the motor cortex. Trends Neurosci 36:706–716.

Silver RA, Lübke J, Sakmann B, Feldmeyer D (2003) High-probability uniquantal transmission at excitatory synapses in barrel cortex. Science 302:1981–1984.

Skoglund TS, Pascher R, Berthold CH (1997) The existence of a layer IV in the rat motor cortex. Cereb Cortex 7:178–180.

Smith PH, Populin LC (2001) Fundamental differences between the thalamocortical recipient layers of the cat auditory and visual cortices. J Comp Neurol 436:508–519.

Smith TC, Howe JR (2000) Concentration-dependent substate behavior of native AMPA receptors. Nat Neurosci 3:992–997.

Staiger JF, Flagmeyer I, Schubert D, Zilles K, Kötter R, Luhmann HJ (2004) Functional diversity of layer IV spiny neurons in rat somatosensory cortex: quantitative morphology of electrophysiologically characterized and biocytin labeled cells. Cereb Cortex 14:690–701.

Stepanyants A, Chklovskii DB (2005) Neurogeometry and potential synaptic connectivity. Trends Neurosci 28:387–394.

Stepanyants A, Hof PR, Chklovskii DB (2002) Geometry and structural plasticity of synaptic connectivity. Neuron 34:275–288.

Stratford KJ, Jack JJB, Larkman AU (1997) Calibration of an autocorrelation-based method for determining amplitude histogram reliability and quantal size. J Physiol 505:425–442.

Stratford KJ, Tarczy-Hornoch K, Martin KAC, Bannister NJ, Jack JJB (1996) Excitatory synaptic inputs to spiny stellate cells in cat visual cortex. Nature 382:258–261.

Südhof TC (2013) Neurotransmitter release: the last millisecond in the life of a synaptic vesicle. Neuron 80:675–690.

Südhof TC, Cowan WM, Stevens CF (2003) Synapses. Johns Hopkins Univ Pr.

Südhof TC, Rothman JE (2009) Membrane fusion: grappling with SNARE and SM proteins. Science 323:474–477.

Takahashi T, Svoboda K, Malinow R (2003) Experience strengthening transmission by driving AMPA receptors into synapses. Science 299:1585–1588.

Tanaka H (2016) Modeling the motor cortex: Optimality, recurrent neural networks, and spatial dynamics. Neurosci Research 104:64–71.

Tanaka J, Matsuzaki M, Tarusawa E, Momiyama A, Molnar E, Kasai H, Shigemoto R (2005) Number and density of AMPA receptors in single synapses in immature cerebellum. J Neurosci 25:799–807.

Tang A-H, Chen H, Li TP, Metzbower SR, MacGillavry HD, Blanpied TA (2016) A trans-synaptic nanocolumn aligns neurotransmitter release to receptors. Nature 536:210–214.

Tarczy-Hornoch K, Martin KAC, Jack JJB, Stratford KJ (1998) Synaptic interactions between smooth and spiny neurones in layer 4 of cat visual cortex in vitro. J Physiol 508:351–363.

Tarczy-Hornoch K, Martin KAC, Stratford KJ, Jack JJB (1999) Intracortical excitation of spiny neurons in layer 4 of cat striate cortex In vitro. Cereb Cortex 9:833–843.

Taschenberger H, Scheuss V, Neher E (2005) Release kinetics, quantal parameters and their modulation during short-term depression at a developing synapse in the rat CNS. J Physiol 568:513–537.

Taylor CSR, Gross CG (2003) Twitches versus movements: A story of motor cortex. Neuroscientist 9:332–342.

Thorne K (1995) Black holes & time warps: Einstein's outrageous legacy. WW Norton & Company.

Tong G, Jahr CE (1994) Multivesicular release from excitatory synapses of cultured hippocampal neurons. Neuron 12:51–59.

Viaene AN, Petrof I, Sherman SM (2011) Synaptic properties of thalamic input to layers 2/3 and 4 of primary somatosensory and auditory cortices. J Neurophysiol 105:279–292.

Voronin LL, Kuhnt U, Hess G, Gusev AG, Roschin V (1992) Quantal parameters of "minimal" excitatory postsynaptic potentials in guinea pig hippocampal slices: binomial approach. Exp Brain Res 89:248–264.

Wadiche JI, Jahr CE (2001) Multivesicular release at climbing fiber-Purkinje cell synapses. Neuron 32:301–313.

Wahl LM, Stratford KJ, Larkman AU, Jack JJB (1995) The variance of successive peaks in synaptic amplitude histograms: effects of inter-site differences in auantal size. Proc R Soc Lond B 262:77–85.

Waller WH, Barris RW (1937) Relationships of thalamic nuclei to the cerebral cortex in the cat. J Comp Neurol 67:317–341.

Walmsley B (1993) Quantal analysis of synaptic transmission. In: Electrophysiology: A practical approach, Oxford University Press:109–141.

Weiler N, Wood L, Yu J, Solla SA, Shepherd GMG (2008) Top-down laminar organization of the excitatory network in motor cortex. Nat Neurosci 11:360–366.

White EL, Czeiger D (1991) Synapses made by axons of callosal projection neurons in mouse somatosensory cortex: Emphasis on intrinsic connections. J Comp Neurol 303:233–244.

Winfield DA, Powell TPS (1983) Laminar cell counts and geniculo-cortical boutons in area 17 of cat and monkey. Brain Res 277:223–229.

Yamawaki N, Borges K, Suter BA, Harris KD, Shepherd GMG (2015) A genuine layer 4 in motor cortex with prototypical synaptic circuit connectivity. eLife 3:e05422.

Zola-Morgan S (1995) Localization of brain function: The legacy of Franz Joseph Gall (1758-1828). Annu Rev Neurosci 18:359–383.